Structural Design of Advanced Electrodes Employing Nanostructured V_2O_5 Nanofibers for Metal-ion Battery Application

Von der Fakultät Chemie der Universität Stuttgart

zur Erlangung der Würde eines Doktors der

Naturwissenschaft (Dr. rer. nat.) genehmigte Abhandlung

Vorgelegt von

Achim Max Diem

aus Stuttgart

Hauptberichter:	Prof. Dr. Joachim Bill
Mitberichter:	Prof. Dr. Dr. h. c. Siegfried Schmauder
Prüfungsvorsitzender:	Prof. Dr. Thomas Schleid

Tag der mündlichen Prüfung: 02.07.2020

Institut für Materialwissenschaft

Universität Stuttgart

2021

Contents

Declaration of Authorship / Erklärung über die Eigenständigkeit der Dissertation

Ich versichere, dass die vorliegende Arbeit mit dem Titel

“Structural Design of Advanced Electrodes Employing Nanostructured V_2O_5 Nanofibers for Metal-ion Battery Application”

selbständig verfasst und keine anderen als die angegebenen Quellen und Hilfsmittel benutzt habe; aus fremden Quellen entnommene Passagen und Gedanken sind als solche kenntlich gemacht.

I hereby certify that the dissertation entitled

“Structural Design of Advanced Electrodes Employing Nanostructured V_2O_5 Nanofibers for Metal-ion Battery Application”

is entirely my own work except where otherwise indicated. Passages and ideas from other sources have been clearly indicated.

Name/Name: _____

Unterschrift/Signature: _____

Datum/Date: _____

Publication of the Individual Chapters in Scientific Journals

This thesis has a cumulative style and the content of the individual chapters are composed of the publications published in scientific journals.

Chapter 2: Free-standing Nanostructured Vanadium Pentoxide Films for Metal-ion Batteries

Achim M. Diem, Andrea Knöller, Zaklina Burghard and Joachim Bill. Nanoscale, 2018, 10, 15736–15746. https://doi.org/10.1039/C8NR04033H

(A.M.D. synthesized and characterized the V_2O_5 nanofibers and paper-like thin films, A.K. contribute to the data analysis and discussion of the mechanical properties, Z.B., J.B. supervised the work)

Chapter 3: Binder-free V_2O_5 Cathode for High Energy Density Rechargeable Aluminum-ion Batteries

Achim M. Diem, Bernhard Fenk, Joachim Bill and Zaklina Burghard. Nanomaterials, 2020, 10, 247. https://doi.org/10.3390/nano10020247

(A.M.D. fabricated and investigated the V_2O_5 cathodes, B.F. prepared the TEM lamella and contributed to microstructural discussions, T.H.J. and R.L. assisted the TEM investigations, J.B., Z.B. supervised the work)

Chapter 4: Creasing Highly Porous V_2O_5 Scaffolds for High Energy Density Aluminum-ion Batteries

Achim M. Diem, Joachim Bill and Zaklina Burghard, ACS Applied Energy Materials, 2020, 3, 4033-4042. https://doi.org/10.1021/acsaem.0c00455

(A.M.D. prepared and characterized the V_2O_5 scaffolds, S.E. carried out the BET measurements, J.B., Z.B. supervised the work)

Further non-related Publications

Further contributions in collaboration with other colleagues resulted in two scientific publications. The publications are not included into the content of this thesis.

- Bernd Wicklein, Achim M. Diem, Andrea Knöller, Manoella S. Cavalcante, Lennart Bergström, Joachim Bill, Zaklina Burghard. Dual-Fiber Approach toward Flexible Multifunctional Hybrid Materials, *Advanced Functional Materials*, **2018**, 28, 1704274.

- Andrea Knöller, Stefan Kilper, Achim M. Diem, Marc Widenmeyer, Tomče Runčevski, Robert E. Dinnebier, Joachim Bill, Zaklina Burghard. Ultrahigh Damping Capacities in Lightweight Structural Materials, *Nano Letters*, **2018**, 18, 2519-2524.

- Timotheus Jahnke, Leila Raafat, Daniel Hotz, Andrea Knöller, Achim M. Diem, Joachim Bill and Zaklina Burghard. Highly Porous Free-Standing rGO/SnO_2 Pseudocapacitive Cathodes for High-Rate and Long-Cycling Al-Ion Batteries, *Nanomaterials*, **2020**, 10, 2024.

- Leila Raafat, Bernd Wicklein, Günter Majer, Timotheus Jahnke, Achim M. Diem, Joachim Bill and Zaklina Burghard. Shape-Conformable, Eco-Friendly Cellulose Aerogels as High-Performance Battery Separators, *ACS Applied Energy Materials,* **2021**, 4, 763-774.

List of Abbreviations and Symbols

2D	Two-dimensional
3D	Three-dimensional
$A_{scaffolds}$	Cross-section area of the scaffolds
AIB	Aluminum-ion battery
AFM	Atomic force microscopy
Al	Aluminum
$AlCl_3$	Aluminum chloride
AP	As-prepared
APTES	(3-Aminopropyl)triethoxysilane
Ar	Argon
Au	Gold
BET	Brunauer-Emmett-Teller
CV	Cyclic voltammetry
C_{ct}	Charge-transfer capacitance
C_e	Electrode capacitance
Cu	Copper
d	Interlayer distance
DMC	Dimethyl carbonate
ε	Porosity
EC	Ethylene carbonate
EDX	Energy-dispersive X-ray spectroscopy
EELS	Electron energy loss spectroscopy
EIS	Electrochemical impedance spectroscopy
[EMIM]Cl	1-Ethyl-3-methylimidazolium chloride
H_2O	Water
H-bond	Hydrogen bond
Ir	Iridium
l	Electrode distance
Li	Lithium
LIB	Lithium-ion battery
$LiClO_4$	Lithium perchlorate
Mg	Magnesium

Mo	Molybdenum
N_2	Nitrogen
n	Hydration state
Na	Sodium
NH_4VO_3	Ammonium metavanadate
Ni	Nickel
PT	Post-treated
PTFE	Polytetrafluoroethylene
PVDF	Polyvinylidene fluoride
ρ	Density
ρ_{V2O5}	Density of V_2O_5
R_{ct}	Charge-transfer resistance
R_e	Electrode resistance
$R_{internal}$	Internal resistance
R_s	Contact resistance
σ_0	Electrical bulk conductivity
σ	Electrical conductivity
SEM	Scanning electron microscopy
Si-wafer	Silicon-wafer
Ta	Tantalum
TEM	Transmission electron microscopy
TGA	Thermogravimetric analysis
V_2O_5	Vanadium pentoxide
W_d	Warburg diffusion
XRD	X-ray diffraction

1 General Introduction

Nowadays research in the field of metal-ion batteries is focusing on the development of materials delivering high energy densities even at high current densities to meet the requirements and demands for mobile and stationary devices.[1–3] Typically, electrodes for such systems are composed of powdered active material combined with additives such as polymeric binders for their mechanical support and carbon black for enhancement of their electrical conductivity.[4,5] However, the used additives do not participate in the electrochemical processes, lowering the gravimetric capacity of the electrodes and thus the overall battery cell performance. Therefore, electrodes comprised of only active material with a good intrinsic electrical conductivity would be beneficial for the electrode and hence, cell performance.

Lithium-ion batteries (LIBs) are widely used in advanced electronic devices because their high storage capacities.[6,7] However, their further application is encumbered mainly with their safety issues and limited resources resulting in their rising cost.[8] Therefore, novel metal-ion battery systems are needed, encouraging research on the materials for their individual components, *i.e.*, electrodes, separators and electrolytes (**Figure 1**). To this end, aluminum-ion batteries (AIBs) are very promising as aluminum is the third most abundant element in the earth crust, less hazardous than lithium and provides a three-electron transfer mechanism yielding high theoretical gravimetric and volumetric capacities.[9–12] For their realization, however, some critical issues have to be addressed such as the development of materials capable of hosting trivalent aluminum ions, as well as free-standing while remaining mechanically stable.[13,14] Moreover, the compatibility of the cell components with the typically used ionic liquid-based electrolyte is another challenging issue that has to be overcome to avoid side reactions.[15] To remedy these problems a combination of binder-free systems with optimized working conditions would significantly enhance the cell performance.[16] Accordingly, this dissertation aims to unravel a novel system with an optimized cell setup including structurally designed advanced binder-free vanadium pentoxide (V_2O_5) nanofiber-based electrodes for metal-ion batteries.

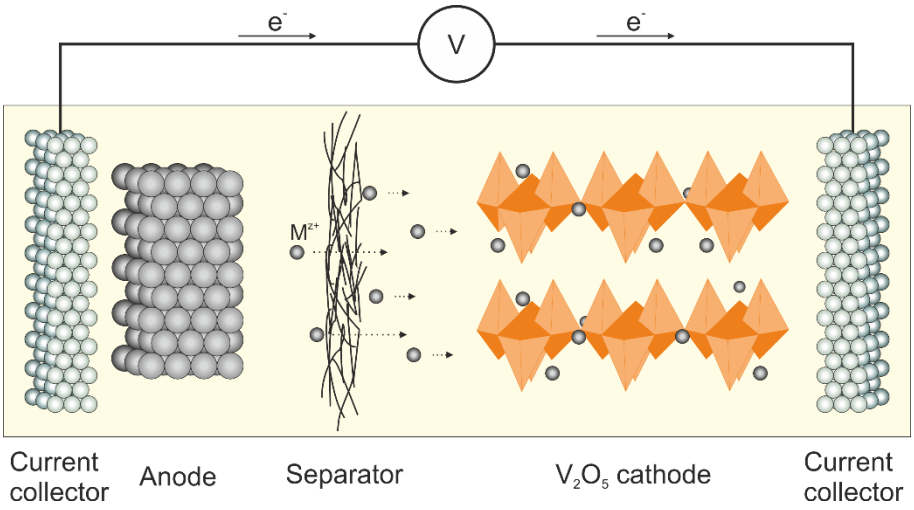

Figure 1: Schematic illustration of a cell setup, including the components, specifically the structure of the V_2O_5 cathode enabling metal-ion intercalation addressed in this thesis.

The rich redox chemistry of vanadium pentoxide designates it as a good intercalation compound with a high theoretical storage capacity of 442 mAh g^{-1}, which is able to accommodate a variety of metal-ions, including Li^+ and Al^{3+}.[17]

Out of all nanostructures of the V_2O_5, the high aspect ratio nanofibers, synthesized by a low temperature sol-gel route, are of great interest due to their intrinsic mechanical flexibility and functional surface groups.[18] The functional surface groups, composed of oxo- and hydroxyl-groups, mainly facilitate the assembly of the nanofibers into different self-supporting structures.[19,20] Furthermore, the nanofiber bilayer structure, separated by water molecules, provides sufficient space for metal-ion intercalation.[17,19,21] However, the electrical conductivity of such V_2O_5 ceramic-based materials is moderate while high storage capacities at high current densities are only achieved if it is sufficiently high. In this respect, it was reported that doping of V_2O_5 with Cu or Ag enhances the conductivity, thus, facilitates fast metal-ion insertion.[22–25] These properties render the nanofibers as an ideal one-dimensional (1D) building block for hierarchically arranged microstructures, employed as advanced free-standing cathodes for Li^+ and Al^{3+} intercalation.

The research reported hereinafter follows structural design as well as electrochemical principles to meet the demands of innovative high energy density electrodes. Along this line, the focal point is developing binder-free systems abstaining inactive and instable components. Their tuned bioinspired microstructure enables the feasibility of metal-ion insertion while remaining their mechanical stability. The gained insights and

results deliver novel guidelines for the design of nanostructured advanced electrodes for metal-ion battery application.

Following structural design principles, adapted from nature, has been recognized as beneficial for the design of novel mechanically stable multifunctional materials, which can find application also as advanced electrodes. The transfer of these design principles to synthesized materials in order to meet the required application properties, involves hierarchical assembly of nanostructured building blocks by a bottom-up strategy. This bioinspired approach is evidently very promising, as nature developed over billions of years multifunctional biomaterials with various compositions and morphologies. The structure of the biomaterials was optimized in respect to their functionality, primarily their mechanical stability, *e.g.,* strength, fracture toughness.[26] A long this line, two prominent examples, nacre and cuttlebone, were investigated in detail. Both examples are based on aragonite ($CaCO_3$) but exhibit completely different morphologies.[27,28] Nacre, the iridescent inner layer of the red abalone shell is formed in seawater and is comprised of 95 wt% of brittle aragonite platelets embedded in a soft organic matrix (5 wt%) of polysaccharides and proteins.[27,29] The two components are assembled in a layered brick-and-mortar-like morphology, as shown in **Figure 2a**. This precisely controlled architecture features several intrinsic reinforcement strategies, including the formation of mineral bridges and nanoasperities, which support energy dissipation and crack deflection yielding high mechanical stability.[26,29] This hierarchical organization renders nacre with a combination of hardness and fracture toughness about eight times enhanced compared to pure $CaCO_3$.[30] Therefore, nacre is an ideal model for fracture resistant ceramic films or membranes.

Complementary, cuttlebone – the buoyancy tank of the cuttlefish – is a highly porous (93% porosity) structure, which is comprised of about 95 wt.% aragonite fibers and 5 wt.% organic matrix.[31] The hierarchical arrangement of such fibers into regularly ordered lamellas and interconnecting pillars (**Figure 2b**), renders the cuttlebone its high mechanical stability.[28] Thereby, sophisticated architecture favors localized compaction rather than total breaking. In this manner, it can resist external pressures greater than 1 MPa.[31] Such performance is motivating to implement the cuttlebone's structure for design of porous and lightweight mechanically stable advanced multifunctional materials.

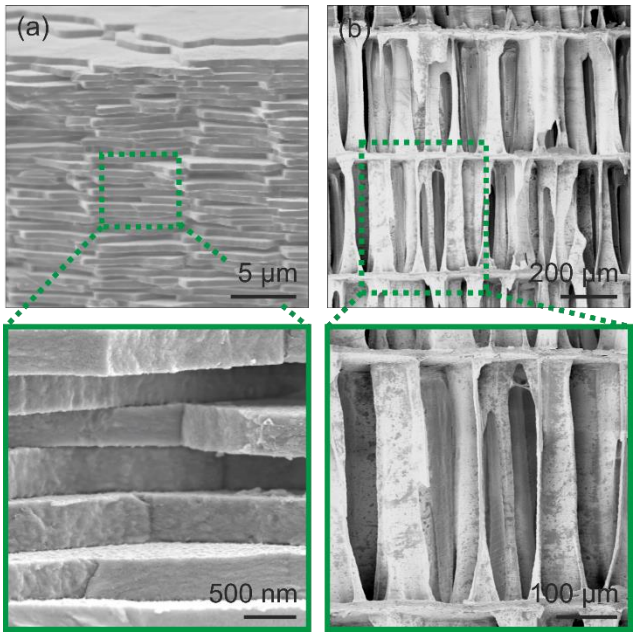

Figure 2: SEM images revealing the microstructure of (a) nacre and (b) cuttlebone, showing their different morphologies although assembled from the same building block material (aragonite).

In this thesis, V_2O_5 nanofibers were utilized as the counterpart to the aragonite-based building blocks for the bioinspired structuring, whereas the incorporated water molecules represent the soft organic fraction. The assembly of the V_2O_5 nanofibers can yield two different, highly ordered microstructures, namely (i) the layered two-dimensional (2D) paper-like thin films, resembling the architecture of nacre and (ii) the highly porous three-dimensional (3D) scaffolds, mimicking the cuttlebone structure.
2D V_2O_5 paper-like thin films (**Figure 3**) are obtained by a facile self-assembly process from an aqueous V_2O_5 nanofiber dispersion.[18,21] The water evaporation induces hydrogen-bond (H-bond) formation between the individual nanofibers, enabled by the functional surface groups and mediated by water molecules.[32] This H-bond formation results in a hierarchical arrangement of the nanofibers into slabs and lamellas.[18,21] The obtained 2D layered microstructure of regularly stacked V_2O_5 sheets, mimics the brick-and-mortar structure of natural nacre. The V_2O_5 paper-like thin film has a thickness in the micrometer range, while the lateral dimensions are in the millimeter range. In addition, such thin films are optical transparent, self-supported and mechanically stable. The latter allows a high flexibility under strong bending without damaging of the structure.[18]

Contrary to the dense 2D thin films, highly porous 3D scaffolds (**Figure 3**) are fabricated by ice-templating with subsequent freeze-drying. Ice-templating uses ice crystals growing from the aqueous V_2O_5 dispersion as structuring agent along a specific freezing direction or temperature gradient.[33,34] During this freezing process, the nanofibers, specifically their functional surface groups, interact with the growing ice crystals, which support the nanofiber's alignment and trapping, resulting in frozen scaffolds.[33] Removing the ice crystals via freeze-drying yields their negative as porous scaffolds. Therefore, the ice crystal shape and size define the pore morphology of the scaffolds.[35,36] The scaffold's microstructure is characterized by a domain-like structure, each comprised of regularly arranged lamellas with interconnecting pillars. Thus, the V_2O_5 scaffolds resemble the cuttlebone's hierarchical architecture. The macroscopic shape of the scaffolds is in the millimeter range and can be adjusted by the used mold. Such prepared V_2O_5 scaffolds exhibit an ultra-high porosity of 99.9% with a high specific surface area of 211 $m^2\ g^{-1}$. In addition, they show good mechanical stability and moderate electrical conductivity.[34]

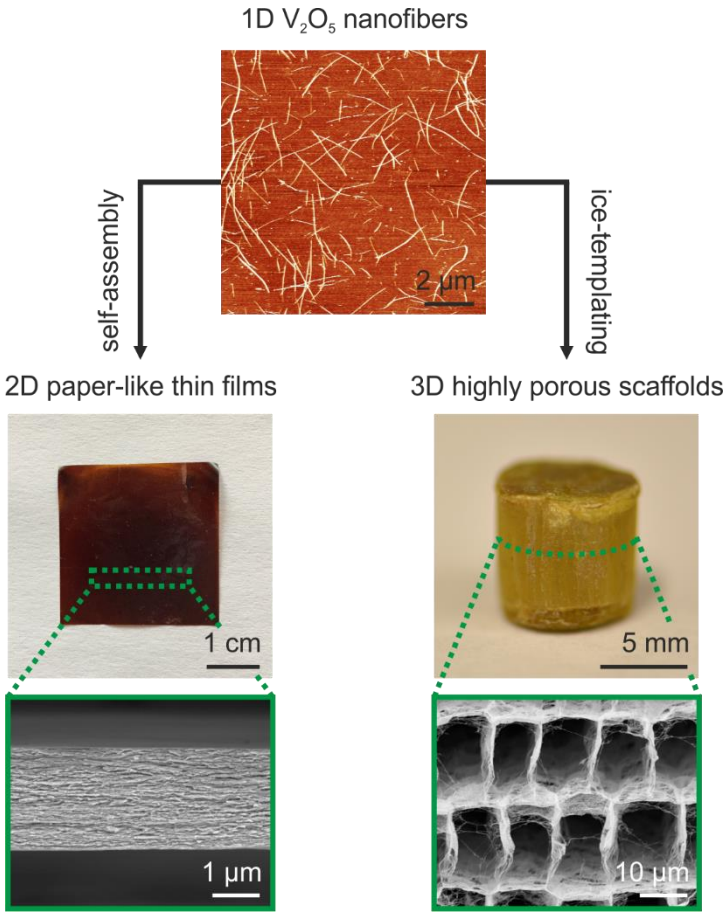

Figure 3: AFM image of V_2O_5 nanofibers, assembled into 2D paper-like thin films by self-assembly (left side) or 3D highly porous scaffolds by ice-templating (right side). For both morphologies a macroscopic and a SEM image is shown. The paper-like thin film is characterized by stacked sheets, whereas the scaffold is comprised of regularly arranged lamellas and interconnecting pillars.

In **chapter 2** (A. M. Diem, A. Knöller, Z. Burghard and J. Bill, *Nanoscale* 2018, *10*, 15736) the influence of the nanofiber length on the 2D thin film formation, as well as the film's mechanical and electrical properties are described. It was established that with increasing the nanofiber length, the Young's modulus, tensile strength and toughness could be significantly enhanced by 45%, 174% and 323%, respectively, achieving 34 GPa, 112 MPa and 189 kJ m^{-3}. Furthermore, the nanofiber length showed significant impact on the in-plane electrical conductivity of the films, reaching almost 2 S cm^{-1}. In addition, a humidity controlled post-treatment was implemented to adjust the water content in order to further improve the film's properties. Such novel paper-like thin films used as cathodes, can reversibly intercalate Li^+, reaching a specific storage capacity of 150 mAh g^{-1} at a current density of 100 mA g^{-1}.

In **chapter 3** (A. M. Diem, B. Fenk, J. Bill and Z. Burghard, *Nanomaterials* 2020, *10*, 247) a self-limiting one-step Cu doping approach for the 2D V_2O_5 paper-like thin films cathodes was demonstrated, for their electrical conductivity enhancement. The Cu dopant occupies one specific insertion site of the bilayered V_2O_5, while another insertion site is available for the reversible Al^{3+} insertion. Furthermore, TEM investigations revealed the formation of Cu-enriched precipitates within a Cu-doped V_2O_5 bronze. In this manner, a high specific discharge capacity of 173 mAh g^{-1} for the novel cathodes, with an energy density of 74 Wh kg^{-1} is achieved. Moreover, the optimization of the cell-setup and working potential window, as well as the high mechanical stability rendered the cathodes with Couloumb efficiencies of almost 100% and a cycling stability over 500 cycles.

The fabrication and microstructural characterization of 3D highly porous scaffolds are presented in **chapter 4** (A. M. Diem, J. Bill and Z. Burghard, *ACS Applied Energy Materials* 2020, *3*, 4033-4042). The scaffolds are characterized by the aligned lamellas with interconnecting pillars and cavities achieved by ice-templating and unidirectional freezing. Creasing the scaffolds leads to a corrugated lamella structure, enhancing of the electrical conductivity by 91% through generating new connection points. The high specific surface area of 211 m^2 g^{-1} of the creased scaffolds, and the one-step Cu doping approach contribute to the achieved high energy densities at unusually high current densities for Al^{3+} intercalation. These cathodes delivered a specific storage capacity of 105 mAh g^{-1} at a current density of 500 mA g^{-1}, yielding an energy density of 52 Wh kg^{-1}.

1.1 References

[1] J. B. Goodenough, Y. Kim, *Chem. Mater.* **2010**, *22*, 587.

[2] V. Etacheri, R. Marom, R. Elazari, G. Salitra, D. Aurbach, *Energy Environ. Sci.* **2011**, *4*, 3243.

[3] J. W. Choi, D. Aurbach, *Nat. Rev. Mater.* **2016**, *1*, 1.

[4] A. Vlad, N. Singh, C. Galande, P. M. Ajayan, *Adv. Energy Mater.* **2015**, *5*, 1402115.

[5] G. Zubi, R. Dufo-López, M. Carvalho, G. Pasaoglu, *Renew. Sustain. Energy Rev.* **2018**, *89*, 292.

[6] M. S. Whittingham, *Chem. Rev.* **2004**, *104*, 4271.

[7] M. Armand, J.-M. Tarascon, *Nature* **2008**, *451*, 652.

[8] F. Wu, H. Yang, Y. Bai, C. Wu, *Adv. Mater.* **2019**, *31*, 1806510.

[9] P. Canepa, G. Sai Gautam, D. C. Hannah, R. Malik, M. Liu, K. G. Gallagher, K. A. Persson, G. Ceder, *Chem. Rev.* **2017**, *117*, 4287.

[10] G. A. Elia, K. Marquardt, K. Hoeppner, S. Fantini, R. Lin, E. Knipping, W. Peters, J.-F. Drillet, S. Passerini, R. Hahn, *Adv. Mater.* **2016**, *28*, 7564.

[11] Z. A. Zafar, S. Imtiaz, R. Razaq, S. Ji, T. Huang, Z. Zhang, Y. Huang, J. A. Anderson, *J. Mater. Chem. A* **2017**, *5*, 5646.

[12] T. Leisegang, F. Meutzner, M. Zschornak, W. Münchgesang, R. Schmid, T. Nestler, R. A. Eremin, A. A. Kabanov, V. A. Blatov, D. C. Meyer, *Front. Chem.* **2019**, *7*, DOI 10.3389/fchem.2019.00268.

[13] S. K. Das, S. Mahapatra, H. Lahan, *J. Mater. Chem. A* **2017**, *5*, 6347.

[14] Y. Zhang, S. Liu, Y. Ji, J. Ma, H. Yu, *Adv. Mater.* **2018**, *30*, 1706310.

[15] L. D. Reed, E. Menke, *J. Electrochem. Soc.* **2013**, *160*, A915.

[16] H. Wang, Y. Bai, S. Chen, X. Luo, C. Wu, F. Wu, J. Lu, K. Amine, *ACS Appl. Mater. Interfaces* **2015**, *7*, 80.

[17] A. Moretti, S. Passerini, *Adv. Energy Mater.* **2016**, *6*, 1600868.

[18] Z. Burghard, A. Leineweber, P. A. van Aken, T. Dufaux, M. Burghard, J. Bill, *Adv. Mater.* **2013**, *25*, 2468.

[19] J. Livage, *Chem. Mater.* **1991**, *3*, 578.

[20] A. Moretti, F. Maroni, I. Osada, F. Nobili, S. Passerini, *ChemElectroChem* **2015**, *2*, 529.

[21] A. M. Diem, A. Knöller, Z. Burghard, J. Bill, *Nanoscale* **2018**, *10*, 15736.

[22] F. Coustier, J. Hill, B. B. Owens, S. Passerini, W. H. Smyrl, *J. Electrochem. Soc.*

1999, *146*, 1355.

[23] F. Coustier, G. Jarero, S. Passerini, W. H. Smyrl, *J. Power Sources* **1999**, *83*, 9.

[24] M. Giorgetti, M. Berrettoni, W. H. Smyrl, *Chem. Mater.* **2007**, *19*, 5991.

[25] A. M. Diem, B. Fenk, J. Bill, Z. Burghard, *Nanomaterials* **2020**, *10*, 247.

[26] M. A. Meyers, P.-Y. Chen, A. Y.-M. Lin, Y. Seki, *Prog. Mater. Sci.* **2008**, *53*, 1.

[27] M. A. Meyers, J. McKittrick, P.-Y. Chen, *Science* **2013**, *339*, 773.

[28] J. Cadman, S. Zhou, Y. Chen, W. Li, R. Appleyard, Q. Li, *Acta Mech. Sin.* **2009**, *26*, 27.

[29] J. Sun, B. Bhushan, *RSC Adv.* **2012**, *2*, 7617.

[30] M. Sarikaya, K. E. Gunnison, M. Yasrebi, I. A. Aksay, *MRS Online Proc. Libr. Arch.* **1989**, *174*, DOI 10.1557/PROC-174-109.

[31] J. D. Birchall, N. L. Thomas, *J. Mater. Sci.* **1983**, *18*, 2081.

[32] V. Petkov, P. N. Trikalitis, E. S. Bozin, S. J. L. Billinge, T. Vogt, M. G. Kanatzidis, *J. Am. Chem. Soc.* **2002**, *124*, 10157.

[33] A. Knöller, T. Runčevski, R. E. Dinnebier, J. Bill, Z. Burghard, *Sci. Rep.* **2017**, *7*, 42951.

[34] A. M. Diem, J. Bill, Z. Burghard, *ACS Appl. Energy Mater.* **2020**, *3*, 4033.

[35] S. Deville, *Adv. Eng. Mater.* **2008**, *10*, 155.

[36] S. Deville, *J. Mater. Res.* **2013**, *28*, 2202.

2 Free-standing Nanostructured Vanadium Pentoxide Films for Metal-ion Batteries

(reprinted with permission of RSC 2018)

Achim M. Diem, Andrea Knöller, Zaklina Burghard and Joachim Bill

Abstract

Owing to their unique layer structure, high aspect ratio and intercalation capability, vanadium pentoxide (V_2O_5) nanofibers are close-to-ideal building blocks for high performance electrodes for metal-ion batteries. However, thus far investigated electrodes composed of V_2O_5 nanofibers mostly contain binders and conductive agents, which reduce the electrodes' gravimetric capacity. Here we demonstrate self-supporting V_2O_5 nanofiber-based films that combine high mechanical flexibility and stability with good electrical conductivity. This has been achieved by suitable adjustment of the nanofiber length, in combination with a suitable humidity controlled post-treatment, to ensure an effective nanofiber interconnection and aging of the films. The optimization of these two parameters allows for an impressive 81%, 184%, and 281% enhancement in Young's modulus, tensile strength and toughness respectively, along with an increase of electrical conductivity by up to 165%. Such films can reach storage capacities of up to 150 mAh g^{-1} without the support of conductive agents and binders. Our findings provide fundamental design guidelines for advanced binder-free electrode materials, which unite high specific storage capacity, excellent mechanical stability and good intrinsic electrical conductivity - the key to technologically advanced battery performance and lifetime.

2.1 Introduction

The development of electrochemical energy storage systems requires electrode materials of high storage capacity, cycling stability and the capability of fast charging rates.[1–3] In this context, many transition metal oxides have been intensively investigated for their application as cathode material in metal-ion batteries, due to their layered crystal structure, multiple valence states and high Coulomb efficiency.[4] Furthermore, it has been demonstrated that the charging rate and cycling stability of such electrodes can be significantly improved by the use of nanoscale materials (e.g., particles, fibers or rods).[5–8] Their high surface area enables better accessibility of the ions and shorter diffusion paths, thus ensuring fast intercalation/deintercalation of the ions.

However, such oxide-based nanostructured materials exhibit poor electrical conductivity and are usually available only in the form of loose powders. Therefore, their implementation into electrodes requires additives, such as binders, which provide mechanical support, and carbon black, which serves as a conductive agent. In general, these additives do not participate in the actual energy storage process, and accordingly lead to a reduced gravimetric storage capacity. As another disadvantage, recycling batteries composed of such electrodes is demanding due to the large number of components involved. To overcome these limitations, suitable strategies are needed to design novel types of self-supporting electrodes, which inherently are mechanically stable and electrically conductive, thus no binders and conductive agents are required. Oxide nanostructures that are particularly promising in this respect are vanadium pentoxide (V_2O_5) nanofibers, obtainable by a low temperature sol-gel method.[5] The nanofibers exhibit a ribbon-like shape with a height of 1.5 nm, width of 10 nm, and length up to several micrometers.[9,10] An AFM image of a typical nanofiber is shown in Fig. 1a, along with a schematic depiction of its structure in Fig. 1b. The nanofiber's rectangular cross-section consists of two V_2O_5 layers,[10] which are separated by water molecules, leading to a layer separation of between 8.4 Å and 17.7 Å, depending on the water content.[5] The hydration state of the nanofibers is commonly quantified by $V_2O_5 \cdot n\ H_2O$, where n is the number of water molecules per V_2O_5 unit.

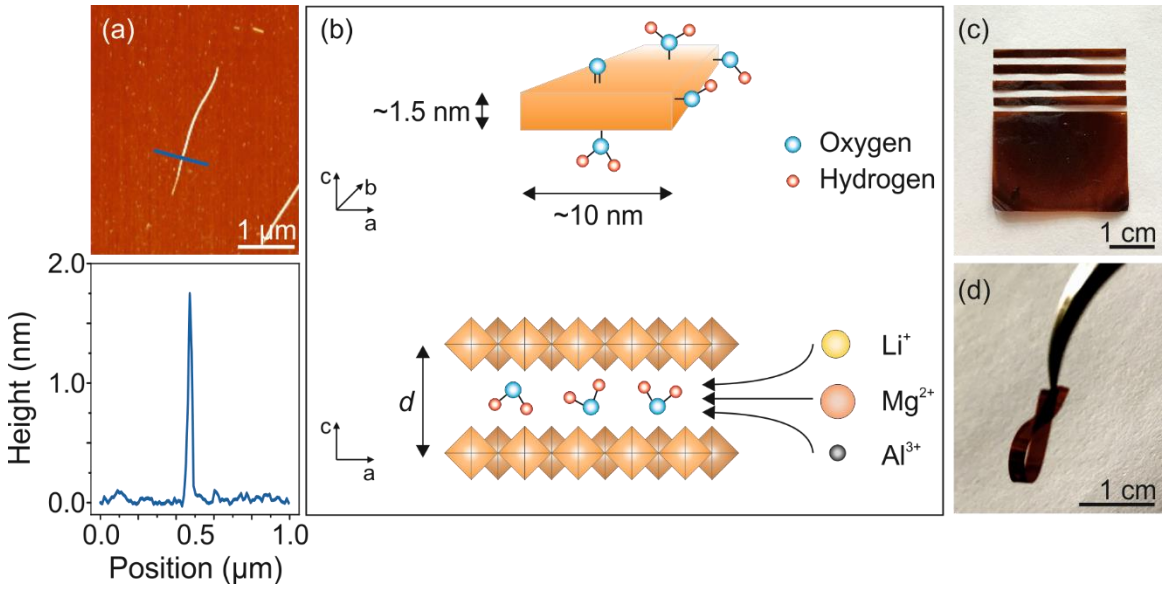

Fig. 1 (a) Representative AFM height image of an individual V_2O_5 nanofiber deposited on a silicon substrate with the cross-sectional analysis along the blue line, revealing a nanofiber height of 1.7 nm. (b) Schematic illustration of a V_2O_5 nanofiber with its characteristic dimensions and double layer structure with a spacing *d*, available for the intercalation of different metal-ions. (c) Digital image of a 2 µm thick free-standing film fabricated *via* self-assembly of V_2O_5 nanofibers. Out of these films various geometries can be cut or punched-out, e.g. ~2 mm thin strips. (d) A strip folded by tweezers to demonstrate flexibility and mechanical stability of the film.

A major advantage of the V_2O_5 nanofibers is their spacious bilayer structure, which enables metal-ion intercalation. For the intercalation of three Li^+ ions, a high theoretical capacity of 442 mAh g^{-1} got close to be reached.[11] The interlayer water molecules, which keep the two V_2O_5 layers sufficiently apart (Fig. 1b), also enable the intercalation of larger ions such as Na^+,[12,13] Mg^{2+},[14] or Al^{3+}.[15,16] For Mg^{2+}, it has been documented that the water facilitates the intercalation by shielding the ion charge of Mg^{2+} *via* a solvent co-intercalation mechanism, thus enabling a fast shuttling of the ions during electrochemical cycling.[14] As a further advantage, vanadium is an abundant element in the earth's crust, which reduces the material costs. It is noteworthy that the unique properties of V_2O_5 nanofibers have prompted interest in their application not only for energy storage, but also for sensors[2] and actuators.[17]

Toward practical electrode fabrication, a reliable method is needed to assemble the V_2O_5 nanofibers into films, whose structure ensures both good accessibility of the nanofibers by the ions as well as good mechanical stability. Moreover, the films must

have sufficient electrical conductivity to achieve fast cycling kinetics. Along these lines, it is beneficial that the nanofibers are decorated by oxo- and hydroxyl groups (Fig. 1b), which can form an extended hydrogen-bonded (H-bond) network between the nanofibers and thereby guide the self-assembly of the nanofibers into paper-like films (Fig. 1c,d).[9] However, it is not straightforward to take advantage of these interactions, unless several factors are carefully controlled such as concentration of the sol[18] and nanofiber length[6] or drying conditions. In fact, drying of aqueous solutions of high concentration that contain nanofibers with a length of more than several micrometers, yields xerogels composed of a disordered, highly entangled nanofiber network.[5] Such a microstructure impedes effective stress distribution during mechanical loading, and also limits the electrical conductivity.[9,19,20]

By contrast, shorter V_2O_5 nanofibers (with a length of a few micrometers) are able to self-assemble into micrometer thick, free-standing paper-like films.[9] The highly ordered layered structure of the films ensures very good mechanical flexibility and stability. They can be fabricated or cut in any desired shape (Fig. 1c), an important prerequisite for electrode applications. The films show superior electrical conductivity in the range of 0.1-1 S cm^{-1},[17,19] as compared to V_2O_5 single crystals and vapor- (or sputter-) deposited V_2O_5 films for which values of ~10^{-2}-10^{-4} S cm^{-1} and ~10^{-3}-10^{-6} S cm^{-1},[20,21] respectively, have been reported. In order to further enhance the electrical conductivity of the V_2O_5 nanofiber films, graphene[22] or carbon nanotubes have been added.[23] While in this manner the electrical conductivity could indeed be improved, the resultant hybrid material in the form of loose powder has all the above mentioned disadvantages of additive-containing electrodes.

Here, we investigate the influence of nanofiber length on the microstructure and the mechanical and electrical properties of free-standing films self-assembled from V_2O_5 nanofibers with a length of up to several micrometers. In addition, we explore the effect of controlled hydration and aging of the films, both as a means to control the internal hydrogen-bond network and nanofiber interconnectivity, on the aforementioned properties. The remarkable combination of excellent mechanical stability and good electrical conductivity of the free-standing films renders them promising as electrode material with a fast charging rates, high gravimetric storage capacity, as well as a long lifetime.

2.2 Results and Discussion

The hydrated V_2O_5 ($V_2O_5 \cdot n\ H_2O$) nanofibers used in this study were obtained through heat-induced sol-gel synthesis using ammonium meta-vanadate (NH_4VO_3) in aqueous solution. While the nanofiber height depends on the amount of intercalated water, their length can be adjusted *via* the synthesis conditions, in particular the synthesis temperature (which is typically maintained for several minutes) and the growth time (many days) after synthesis under ambient conditions.[6] Keeping the first parameter constant, we stored the obtained aqueous solutions for different growth times under ambient conditions. The average length of thus obtained nanofibers was determined with the aid of atomic force microscopy (AFM), as displayed in Fig. 2a-d, where the four different types of samples V_2O_5-1, V_2O_5-2, V_2O_5-3 and V_2O_5-4 correspond to growth times of 3, 14, 28 and 42 days, respectively. The plot in Fig. 2e reveals a monotonic increase of the nanofiber length with time from V_2O_5-1 (0.54 ± 0.47 µm) to V_2O_5-4 (1.95 ± 0.5 µm) and the width of the length distribution is seen to increase significantly from V_2O_5-1 to V_2O_5-4. Further relevant data are provided in the Supporting Information Table S1.

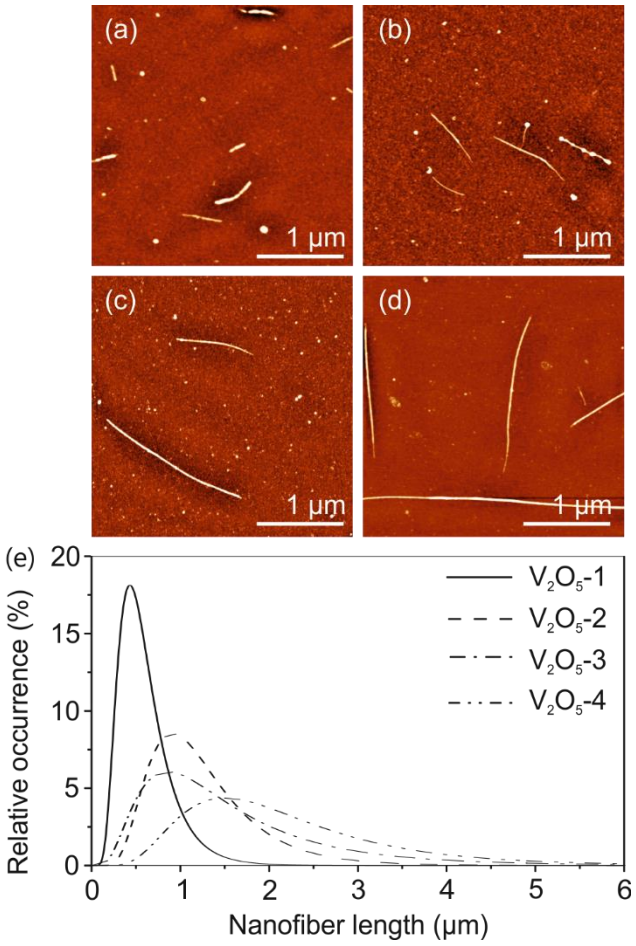

Fig. 2 (a)-(d) AFM images for individual V_2O_5 nanofibers adsorbed on a silicon substrate of (a) V_2O_5-1, (b) V_2O_5-2, (c) V_2O_5-3, (d) V_2O_5-4 and (e) the corresponding V_2O_5 nanofiber length distributions obtained from AFM investigations.

In general, the V_2O_5 nanofibers grow from a dot-shaped to a fibrous structure *via* an anisotropic polycondensation reaction of the precursor molecules in the aqueous solution.[5,6] The increasing width of the length distributions in Fig. 2e with increasing growth time implies a second, simultaneously occurring growth mechanism. The linking of dissolved precursor molecules to the already existing nanofibers is most likely accompanied by the partial combination of two already existing nanofibers. The latter not only increases the average nanofiber length, but also decreases the relative occurrence and likewise is responsible for the broadening of the length distributions with increasing growth time.

Upon slowly evaporating the water from the nanofiber solutions at room temperature, the V_2O_5 nanofibers first form slabs which then self-assemble into lamellas. The latter undergo further self-assembly by stacking on top of each other, leading to a highly organized structure of architecture with an extended H-bond network supported by the

water molecules in-between (Fig. 3a).[9] We investigated the influence of nanofiber length on the films' microstructure, and how the latter is further affected by a humidity-controlled drying of the samples at 40 °C (for details see the experimental section). This humidity-controlled post-treatment (PT) is expected to promote rearrangement of the H-bonds already formed during the drying under ambient conditions.

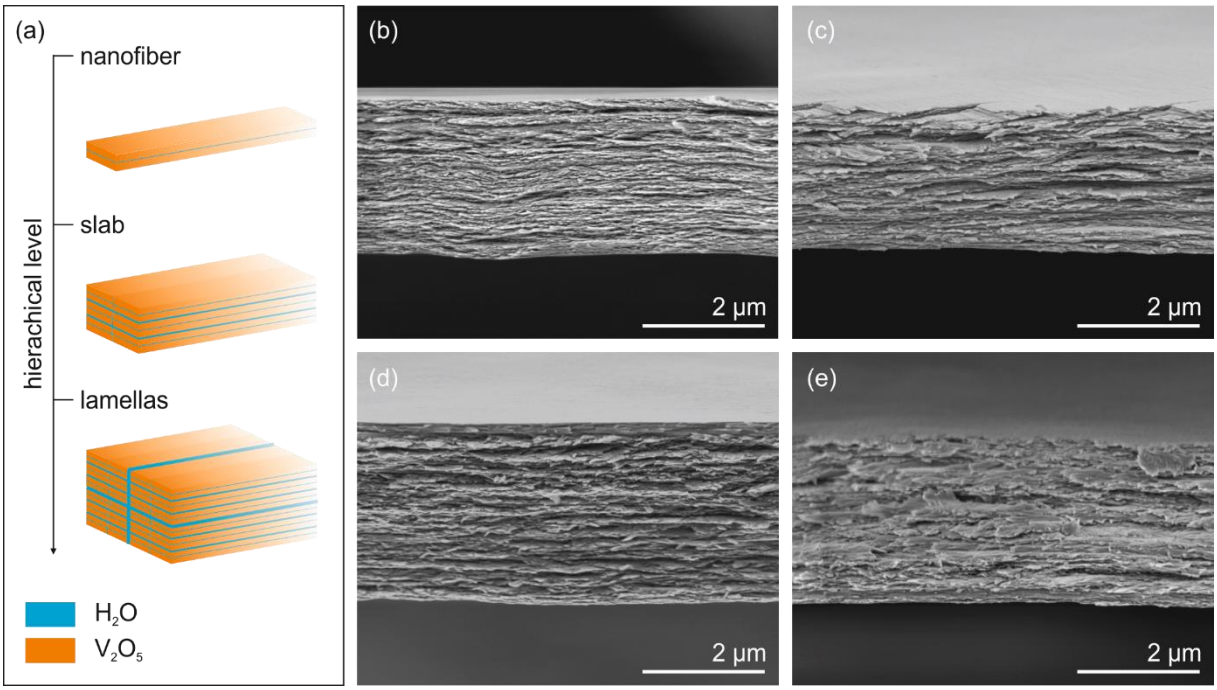

Fig. 3 (a) Schematic depiction of V_2O_5 nanofibers as building blocks, which are arranged in hierarchical levels, such as slabs and lamellas which are separated by water molecules. (b)-(e) SEM cross-section micrographs of paper's fracture surface for (b) V_2O_5-1/AP, (c) V_2O_5-2/AP, (d) V_2O_5-3/AP and (e) V_2O_5-4/AP.

Scanning electron microscopy (SEM) analysis of the fracture surface of the mechanically broken films of the as-prepared (AP) samples revealed a uniform stacking of individual V_2O_5 lamellas for a paper thicknesses of ~2.0 µm - 2.5 µm (Fig. 3b-e). It can be observed that while the fracture surface of V_2O_5-1/AP with shorter nanofibers (Fig. 3b) is relatively smooth, that of V_2O_5-4/AP with longer nanofibers (Fig. 3e) is considerably rougher and also displays pronounced pull-out lamellas. Their easier pull-out reflects a strong lateral connection between the slabs composed of long nanofibers, such that the slabs and lamellas are able to remain as intact entities upon sliding with respect to each other.

Having explored the nanofiber arrangement in the vertical direction, we further investigated the surface morphology of the films by AFM (Fig. 4) to unravel the degree of lateral alignment of the self-assembled V_2O_5 fibers over an area of several square micrometers. Remarkably, it can be seen that the individual nanofibers are aggregated into slabs, whose smooth surface indicates strong inter-fiber connections. As previously reported by Petkov et al.[10] the nanofibers within the slabs are connected in parallel and side-by-side *via* sharing corners of octahedra. From the slab width of between 10 nm and 20 nm, it follows that they are laterally composed of two nanofibers (see schematic depiction in Fig. 3a), in agreement with the conclusions by Petkov et al.[10] It is furthermore apparent that the slab length is correlated with the length of the nanofibers. Moreover, comparison of the AFM images in Fig. 4a and 4d (large scan) reveals a more wavy surface structure for the sample V_2O_5-1/AP, in comparison to the smoother surface and straighter slab alignment in the other cases. The more regular and compact self-assembly of the longer vs. shorter fibers can be understood based upon the larger average contact length between the nanofibers, which facilitates a smooth, “zip-like” lateral attachment between the side facets of the nanofibers within the slabs. This type of attachment continues on the next hierarchical level, comprising slabs laterally connected *via* both direct H-bonds between hydroxyl groups and oxygen bridges, such that the edges (shape) of the slabs are visible in the AFM images. As an additional contribution, in the case of the shorter nanofibers there is a higher probability of structural misfits in the slabs, in particular when the lateral contact length between the nanofibers is especially small. This leads to the formation of kinked slab sections along which the slabs cannot make fully close contact. The density of such imperfect connection sections is significantly higher for the shorter vs. longer nanofiber samples, as apparent from the number of white circles in the AFM images of Fig. 4. This, in turn, results in a lack of regular shape and a stronger variation of the slab width for the sample with the shortest nanofibers (V_2O_5-1/AP), as compared to the three other samples.

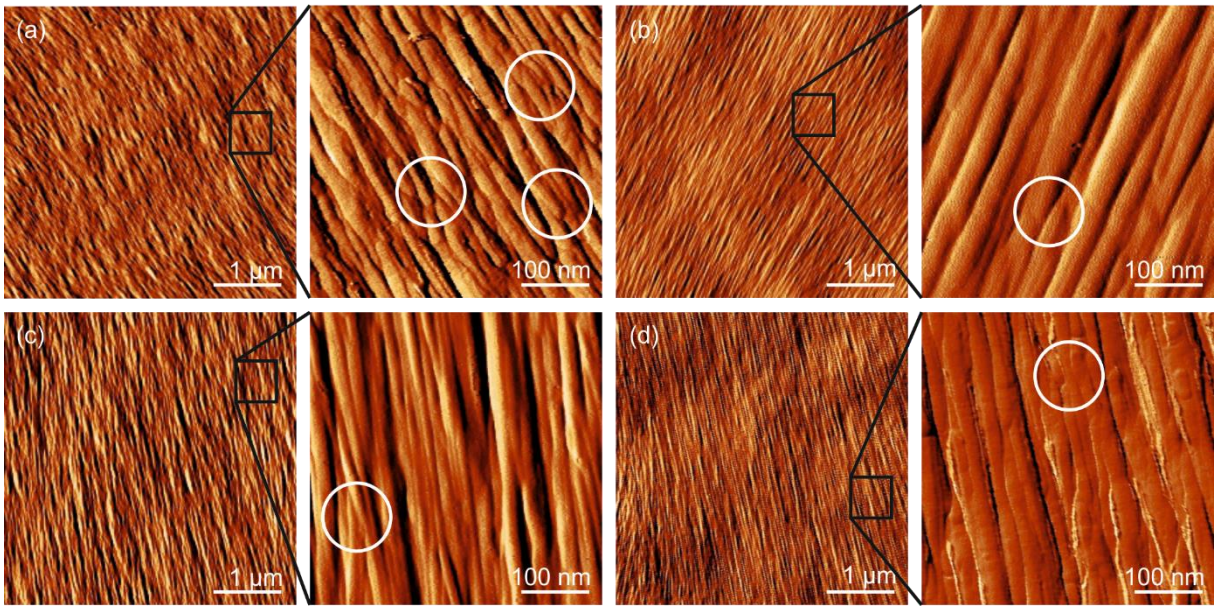

Fig. 4 (a)-(d) AFM amplitude images of the paper's surface, showing an alignment over several tens of micrometer and the interconnection of individual slabs (white circles) for (a) V_2O_5-1/AP, (b) V_2O_5-2/AP, (c) V_2O_5-3/AP and (d) V_2O_5-4/AP. Local lateral connections between the slabs are highlighted by white circles.

In order to determine the height of the slabs, we complemented the SEM and AFM investigations by X-ray diffraction (XRD) measurements on the films. The slab height, which reflects the number of vertically stacked nanofibers, was derived from the XRD peak widths (Fig. 5a and 5c). It continuously increases from ~5 nm to ~6 nm with increasing nanofiber length, which translates into an increase from ~2.5 to 3 vertically stacked nanofibers. That the slab height is almost independent on the nanofiber length (Fig. 5c) is important for the interpretation of the films' mechanical properties (see below). The combined AFM and XRD results indicate that for all investigated fiber lengths, the slabs on average are composed of three nanofibers in the vertical and two nanofibers in the lateral direction, while the slab length is governed by the nanofiber length. XRD data further provide information about the interlayer distance *d* within the V_2O_5 nanofibers, which is related to the amount of intercalated water and hence a measure for the films' hydration state. From the positions of the main reflection peak, an almost constant *d* value of ~1.0 nm is calculated, implying the same hydration state for all samples. Extrapolating the dependence of interlayer distance on hydration state, as reported in the literature,[5,20] yields $n = 1.25$ water molecules per V_2O_5 unit. The same result was obtained for the PT samples for all investigated nanofiber lengths, which shows that during the treatment at 40 °C under controlled humidity, no water is

introduced into the fibers, but only between slabs and on the film surface (Fig. 5b and 5c).

Very similar observations to those detailed above for the morphology of the AP samples were made on the PT samples for all investigated nanofiber lengths. The corresponding SEM and AFM images are depicted in Fig. S1 (Supporting Information). It turned out that upon the humidity controlled post-treatment of AP samples, the papers' microstructure as well as the interlayer distance (Fig. 5b) within the nanofibers and the slab height (Fig. 5c) is preserved. The latter implies that there is no significant change in the samples' hydration state.

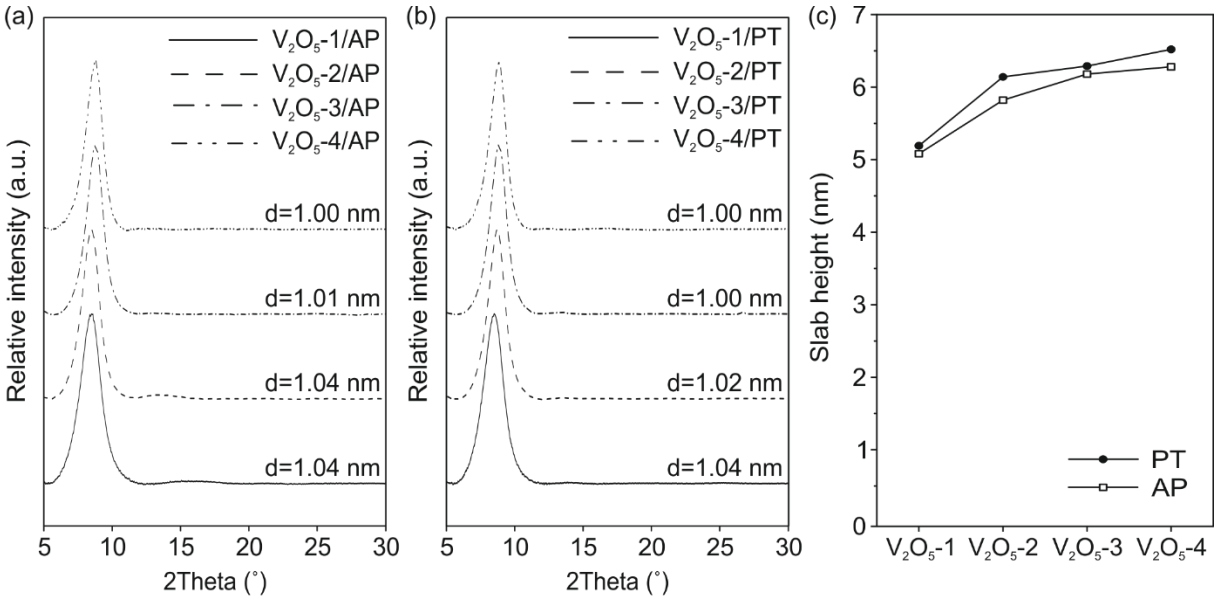

Fig. 5 XRD scans of (a) as-prepared (AP) and (b) post-treated (PT) with the respective interlayer spacing *d*. (c) Calculated slab height obtained from the XRD data.

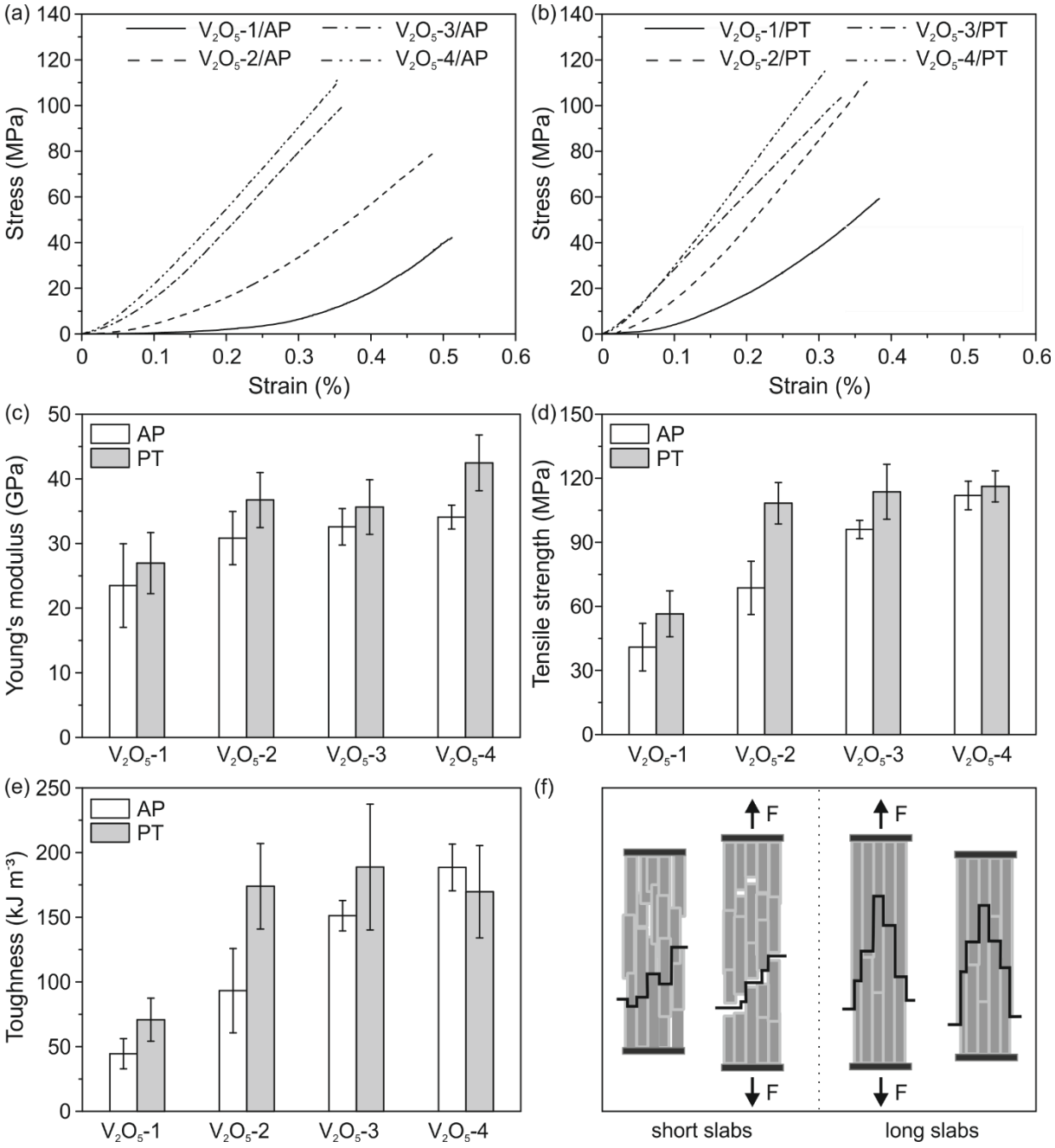

Fig. 6 Typical stress-strain curves obtained by nanotensile tests as a function of V_2O_5 nanofiber length for (a) AP and (b) PT samples. Assessment of the determined mechanical properties: (c) Young's modulus, (d) tensile strength, (e) toughness and (f) Schematic depiction of the deformation mechanism for samples comprising short or long slabs under tensile loading under the same applied load. The black lines indicate pathways for crack formation and propagation (in the case of the short slabs), and sliding of the slabs along each other (in the case of the long slabs).

In order to evaluate the mechanical performance of the films, we have characterized the AP and PT samples by nanomechanical tests. The nanofiber length-dependent mechanical properties in the in-plane direction are summarized in Fig. 6.

The stress-strain curve of the V_2O_5-1/AP sample initially displays a relatively small increase in stress with strain, which is followed by a linear regime of much steeper slope (Fig. 6a). This initial regime becomes increasingly less pronounced for films made of longer nanofibers, so that for the largest nanofiber length only the linear regime with a steep slope remains. The corresponding Young's modulus (Fig. 6c), which is determined before failure, displays an increase in stiffness with increasing nanofiber length. While the Young's modulus increases by 45%, the tensile strength (Fig. 6d) and toughness (Fig. 6e) are improved by 174% and 323%, respectively. By contrast, the maximum strain (Fig. S2, Supporting Information) changes only very little with nanofiber length. Based upon the structural characterization, it follows that the weak links during film deformation are between the slabs within the lamellas (held together by direct hydrogen bonds or oxygen bridges) and between the lamellas (connected by water-mediated hydrogen bonds). Both these bonding types are weaker than the bonds between the nanofibers in the slabs. Therefore, the observed trend for mechanical properties of the investigated films can be understood from the corresponding change in the density of connection points between the slabs (Fig. 4, white circles), which constitute mechanically weak links upon tensile loading. Another contribution likely stems from the interconnection area between the slabs. In particular, the initial stress-strain curve for the films involving the shortest fibers is attributable to easy slab movement and reorientation during the stress increase. This reorganization, which is enabled by the relatively weak connections between the short slabs (because of the small contact area and large number of contact points) (Fig. 6f), progressively leads to interlocking of the slabs and correspondingly to enhanced mechanical properties, as manifested in the increased slope of the curve in the higher strain regime. In comparison, the papers comprising longer nanofibers contain a smaller density of contact points (i.e., slab ends) and also a large interconnection area (i.e., area between the laterally connected slabs) (Fig. 6f). This more regular and compact structure does not easily support movement of the slabs within the plane. Hence, the main deformation during the applied stress occurs in the out-of-plane direction, where weaker H-bond (*via* water molecules) interconnections of the lamellas are present. This scenario is supported by the fact that the toughness (i.e. work of fracture) of the

investigated papers depends more sensitively on the nanofiber length. The slab and lamella pull-out enabled by the longer nanofibers (Fig. 3b-e) lead to enhanced energy dissipation and hence higher toughness of the films. The pull-out of slabs, in turn, is associated with the so-called stick-slip effect, which describes an intrinsic reinforcement. In principle, as the H-bonds between the slabs break and rebuild at an offset position under tensile loading, their effect is more pronounced in the samples with long slabs due to their the larger interconnection area. Sinko and Keten[24] simulated the stick-slip effect in cellulose nanocrystals for shear and tensile loading depending on the type and number of bonds. They found that H-bonds are the most dominant bonding type governing the tensile strength. Similarly, Medhekar *et al.*[25] proved for graphene oxide papers that by increasing the water content, more H-bonds are generated between the sheets, which improves the H-bond network and thus mechanically strengthens the paper. Such a trend also accounts well also for the nanofiber length-dependent mechanical properties of the present V_2O_5 films.

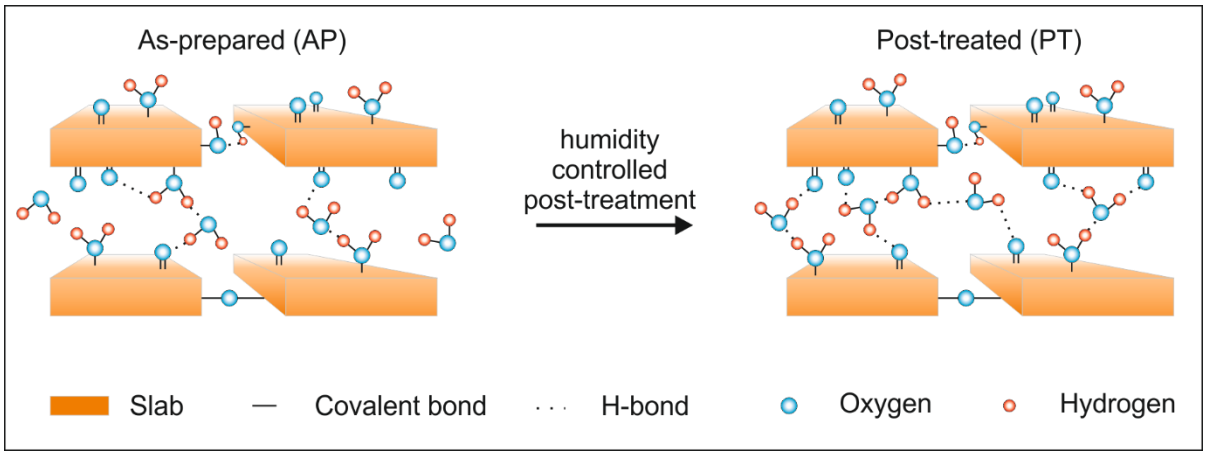

Fig. 7 Schematic illustration of the water molecules and corresponding H-bond network rearrangement between V_2O_5 slabs before and after humidity controlled post-treatment of the paper leading to the “annealing” of the H-bonds.

Subjecting the films to a humidity-controlled, post-treatment resulted in a notable enhancement of Young’s modulus (Fig. 6c), tensile strength (Fig. 6d), and toughness (Fig. 6e) while the maximum strain is reduced (Fig. S2, Supporting Information). In particular, an increase in Young’s modulus of 25 % and in tensile strength of 4 % was observed for V_2O_5-4. While a change of the film’s microstructure can be ruled out as a reason for these changes, it is relevant that the self-assembly of the nanofibers proceeds in an uncontrolled manner, such that the humidity controlled post-treatment

is able to “anneal” the H-bond network and thus improve the H-bond distribution (Fig. 7). The latter is, in turn, expected to enhance the above described mechanical stabilization mechanisms.

Complementary to the mechanical properties of the films, we also investigated their in-plane electrical conductivity. In general, the films’ electrical conductivity has both electronic and ionic contributions. The electronic component involves unpaired electron hopping between V^{4+} and V^{5+} centers along the nanofibers, while the ionic conductivity is carried by proton diffusion along the nanofiber surface.[5,26] The relative contributions of the two mechanisms depend on several factors, including the nanofibers’ fabrication conditions, the structure and thickness of the resulting thin films, as well as the surrounding atmosphere.[5,21] Remarkably, the conductivity (measured directly after sample fabrication) decreases with increasing nanofiber length, although the change is relatively small (Fig. 8a). This observation points toward proton conduction as the major transport mechanism in the present films. In fact, the proton diffusion is known to depend much less on the nanofiber orientation than on the H-bond network, in accordance with the Grotthuss mechanism.[27] The latter involves proton transport *via* a turnover from H-bonds. Cleavage of these bonds (Fig. 8d path 3) and the subsequent formation of a new bond (Fig. 8d path 4) lead to a shift of the positive charge along the H-bonded matrix. Thus, the connection points between the nanofibers and other barriers can be easily passed (Fig. 8d path 5). Conversely, the electronic hopping conduction, which is facilitated along the nanofiber direction,[5] is expected to be favored by the better aligned and long nanofiber slabs in the samples made of longer nanofibers, which is opposite to the behavior observed in Fig. 8a. That proton diffusion is the dominant conduction mechanism in the present V_2O_5 *n* H_2O papers with $n = 1.25$ is, furthermore, consistent with observations made by Livage.[5]

The above conclusion is also in accordance with the electrical behavior of the PT samples, which display a notably increased conductivity, which is consistent with the improved H-bond distribution discussed earlier (Fig. 7). However, when the samples are stored for a prolonged time under ambient conditions (‘aging’), the situation appears to change. As apparent from Fig. 8b, the films’ conductivity gradually increases with time from 0.73 ± 0.06 S cm^{-1} to 1.13 ± 0.10 S cm^{-1} and from 1.01 ± 0.13 S cm^{-1} to 1.67 ± 0.18 S cm^{-1} after 160 days of aging for V_2O_5-1/AP and V_2O_5-1/PT, respectively. This increase most likely originates from a partial chemical reduction of the V^{5+} centers in the V_2O_5 nanofibers, predominantly close to the papers’

surface.[21] The increased fraction of V^{4+} centers then increases the electrical contribution to the overall conductivity of the V_2O_5 papers.[20,26] The same tendency was also observed for other AP and PT samples, independent of the nanofiber length (Fig. 8c). However, the enhancement turned out to be stronger for the PT samples, which showed an increase of up to 49%. This again confirms the beneficial effect of the humidity-controlled post-treatment on the H-bond network within the films.

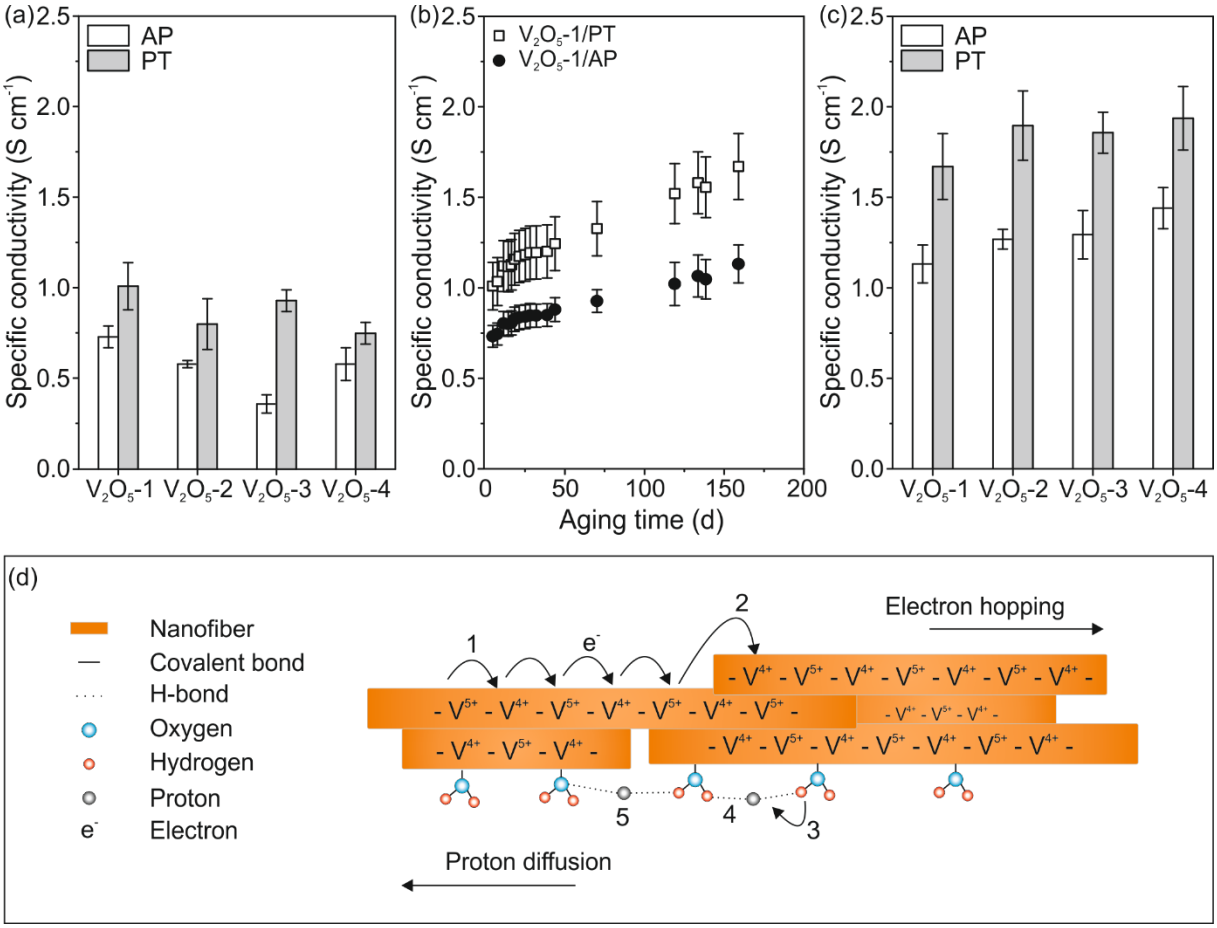

Fig. 8 Specific conductivity of (a) all sample types directly after preparation (b) of V_2O_5-1/AP and V_2O_5-1/PT as a function of the aging time and (c) comparison of all sample types after aging for ~160 days (d) Schematic depiction of the two transport mechanisms: Electron hopping and proton diffusion. Path 1 illustrates the electron transport in nanofibers, whereas the crossover to another nanofiber acts like a barrier (path 2). Proton diffusion is enabled by breaking and formation of H-bonds (paths 3,4) thus, faster transport is possible without the hindrance of the connection points (path 5).

The electrochemical studies of free-standing V_2O_5 nanofiber films for the Li^+ intercalation were performed on samples, which have shown the best mechanical and electrical properties (V_2O_5-4/PT). The results prove that such type of free-standing paper-like materials can be used as a cathode without conductive agents and binders.

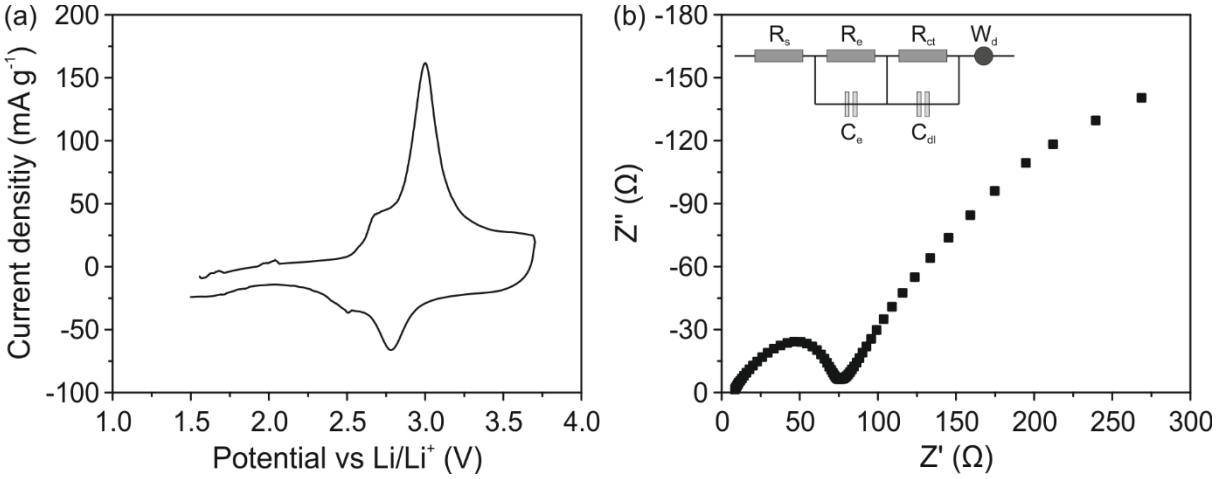

Fig. 9 Electrochemical investigation of a free-standing V_2O_5 film. (a) Current-voltage curve shows the insertion and release of Li^+ during the charging and discharging process, respectively. (b) Nyquist plot obtained by electrochemical impedance spectroscopy. The data were fitted on the basis of the equivalent circuit in the inset.

For the investigated V_2O_5 films, the current-voltage (CV) plot (Fig. 9a) displays a distinct discharging peak at around 2.8 V, which overlaps with the second, less pronounced peak at around 2.5 V. This overlap occurs due to a broadening of the peaks, which most likely arises from the presence of an amorphous structure.[1] In total, the amount of Li^+ intercalated into the structure accounts for 0.9, as extracted from the CV measurements. The electrochemical measurements further revealed that the free-standing V_2O_5 nanofiber films reached a discharge capacity of up to 150 mAh g^{-1} for a charging rate of 100 mA g^{-1}. This value is comparable or even better than the capacity reported for conventional electrodes based on pure vanadium pentoxide for the same charging rate.[22] Complementary electrochemical impedance spectroscopy (EIS) measurements were conducted to determine the films' electrochemical kinetic properties (Fig. 9b). Such measurements revealed that the internal resistance (R_e = 50.8 Ω) and the charge-transfer resistance (R_{ct} = 7.4 Ω) of the free-standing V_2O_5 nanofiber films is much lower than the values of V_2O_5 based electrodes supported by conductive agents and binders. In particular, determined values are 40 % lower than

values reported for crystalline V_2O_5 electrode materials reinforced by graphene and 6 times lower than for the electrodes made of pure vanadium pentoxide.[22] These results underline the faster redox chemistry of the free-standing V_2O_5 film. The better electrochemical properties are assumed to origin from the nanosized fibers, which enable an optimal transport distance and reduced diffusion path for both, ions and electrons. Moreover, the effective alignment of the nanofibers support the aforementioned two electrical conductivity mechanisms.

2.3 Conclusion

We have demonstrated a facile and low-cost fabrication method for mechanically highly stable and electrically conductive V_2O_5 free-standing films. They are obtained by self-assembly of sol-gel derived V_2O_5 nanofibers whose length can be controlled through the growth time. The resulting hierarchical architecture of the films comprises slabs and lamellas interconnected *via* an H-bond network. The films' mechanical and electrical properties are strongly influenced by the nanofiber length and the H-bond density between the slabs and lamellas. Longer nanofibers yield better mechanical properties, because their stronger interconnection ensures effective stress distribution. Suitable tuning of the hydrogen bond network leads to a remarkable 81 %, 184 %, and 281 % enhancement of Young's modulus, tensile strength and toughness, respectively. Likewise, the electrical conductivity depends on the H-bond distribution, since the proton diffusion makes the dominant contribution to the overall conductivity. Remarkably, an increase by up to 159 % can be achieved simply through a humidity controlled post-treatment to improve the proton diffusion through the H-bond matrix. The conductivity can be further increased of up to 165 % through aging of the films, whereupon the V^{5+} species are partially reduced to V^{4+} and hence electron hopping is enhanced. In addition, we proved that such additive-free films can be used for Li^+ intercalation.

The present findings are valuable for the development of novel high performance electrodes for metal-ion batteries which are exclusively composed of active material, and in addition feature good mechanical stability combined with intrinsic electrical conductivity. The optimized nanofiber length should enable an optimal transport distance for ions and electrons within the nanofibers as a prerequisite for fast current rates, while the nanofiber connection *via* water molecules among the nanofibers provides fast transport pathways for the electrolyte and ions. In addition, the optimum nanofiber length is expected to improve the mechanical stability by enabling effective stress distribution throughout the material, which during charge-discharge cycling would result in an enhanced rate capability and cycling stability.

2.4 Experimental Section

Synthesis of V_2O_5 dispersion: The V_2O_5 nanofiber dispersion was prepared by mixing ammonium meta-vanadate (1 g, Fluka) and an acidic ion-exchanger (10 g, Dowex 50WX8 50-100, Alfa Aesar) in deionized water (200 ml) as pioneered by Livage.[7] This aqueous mixture was heated to 80 °C in an oil bath for 10 min under continuous stirring. The V_2O_5 dispersion reached a temperature of 45 °C. Subsequently the V_2O_5 dispersion was cooled to room temperature and the nanofibers grew for 3, 14, 28 and 42 days.

Fabrication of V_2O_5 samples: Silicon (100)-wafers (p-type, Wacker, Sitronic AG) were used which were cleaned by immersion in chloroform, acetone and ethanol each for 10 min in an ultrasonic bath and drying in a nitrogen flow. The cleaned Si-wafers were placed in a glass beaker with a certain volume (9 ml) of the V_2O_5 dispersion of the desired growth time and a sufficiently low concentration to avoid interference due to nanofiber entanglement already in the initial assembly stage. The V_2O_5 samples were dried at room temperature for several days. After the complete evaporation of the water, the V_2O_5 film could be removed in a water bath to get a free-standing film. One batch of as-prepared V_2O_5 films were additionally post-treated in a climatic chamber (VC 7018, Vötsch) to enhance to hydrogen bond distribution of the paper. This drying program consisted of increasing the humidity from 50 % to 80 % and the temperature from room temperature to 40 °C in 15 min. The temperature was kept constant for 15 hours, while the humidity started to decrease after one hour, to 20 % in 10 hours and held there for further 4.5 hours. At the end the temperature was reduced again to room temperature. In order to determine the nanofiber length, the cleaned Si-wafers were coated with a self-assembled monolayer (SAM) by immersing the Si-wafers for 5 min in a 1:1000 diluted mixture of (3-Aminopropyl)triethoxysilane (APTES, Sigma Aldrich) and deionized water. Those Si-wafers were dipped in a 1:90 solution of the V_2O_5 dispersion and deionized water to deposit single V_2O_5 nanofibers. Subsequently the Si-wafer were rinsed in water and dried in a nitrogen stream.

Microstructural characterization: For microstructural investigations atomic force microscopy (AFM, MultiMode 8, Nanoscope V, Bruker) and scanning electron microscopy (SEM, Zeiss Ultra 55) were used. X-ray diffraction experiments were carried out by PXRD (Rigaku Smartlab) using copper K_α radiation with an acceleration voltage of 40 kV and a current of 30 mA. The measuring mode was grazing incidence

in the range of 5-30° with a step size of 0.04°. By using Bragg's law the interlayer distance is calculated, whereas the slab height is obtained using the Scherrer equation.

Mechanical characterization: The mechanical properties were determined by nanotensile tests (Nano Bionix, Keysight Technologies (former MTS)). Therefore, the free-standing films were cut into strips of 1 mm in width and 10 mm in length and were glued on cardboard. The system was run by controlling the force with an applied strain rate of $1 \cdot 10^{-4}$ mm s^{-1} and a load resolution of 50 nN. Out of the obtained data, at least 5 measurements were averaged.

Electrical characterization: The electrical conductivity was measured *via* a four-terminal configuration (SourceMeter 2400, Keithley). For this purpose the free-standing V_2O_5 film was fixed on a glass substrate with kapton tape. Four further gold contacts were sputtered (100 nm, SCD 040, Balzers Union) on the samples to ensure good electrical contact between the measuring pins and the sample. The gold contacts had a spacing of 3 mm. All samples were kept at room temperature under ambient conditions for 160 days to investigate the effect of the samples aging on their electrical conductivity.

The mechanical and electrical investigations, as well as AFM measurements and X-ray diffraction, were performed under ambient conditions at room temperature.

Electrochemical characterization: Swagelok™ union connections made of PTFE were used with stainless steel contacts as half-cells. Their assembly was done in an argon filled glovebox (Labmaster SP, MBraun). Before assembly, the free-standing V_2O_5 films were sputtered from both sides with a thin gold layer (10 nm, SCD 040, Balzers Union) to reduce the contact resistance towards the current collector (8 µm thick aluminum foil, 99 %, Sigma Aldrich). A lithium foil (99.9 %, Alfa Aesar) served as counter electrode, which was attached to another current collector (25 µm thick copper foil, 99.98 %, Sigma Aldrich). Both electrodes were separated by a glass fiber membrane (Grade 934-AH, Whatman), which was soaked with electrolyte. The latter consists of a 1:1 mixture of ethylene carbonate (99 %, Sigma Aldrich) and dimethyl carbonate (>99 %, Sigma Aldrich) with 1 M $LiClO_4$ (>99 %, Sigma Aldrich). All electrochemical tests were conducted on a Multi Autolab M204 test station (Metrohm). Galvanostatic charge/discharge tests were carried out with current rate of 100 mA g^{-1}, cyclic voltammetry with a sweep rate of 0.1 mV s^{-1} in the voltage range of 1.5-3.7 V and electrochemical impedance spectroscopy was performed in the frequency range between 0.1 and 10^6 Hz.

2.5 Supporting Information

Table S1. V_2O_5 nanofiber length determined from AFM scans in dependence of the dispersion growth time.

V_2O_5 nanofibers	V_2O_5-1	V_2O_5-2	V_2O_5-3	V_2O_5-4
Growth time (d)	3	14	28	42
Length (µm)	0.54 + 0.47	1.13 + 0.46	1.30 + 0.64	1.95 + 0.51

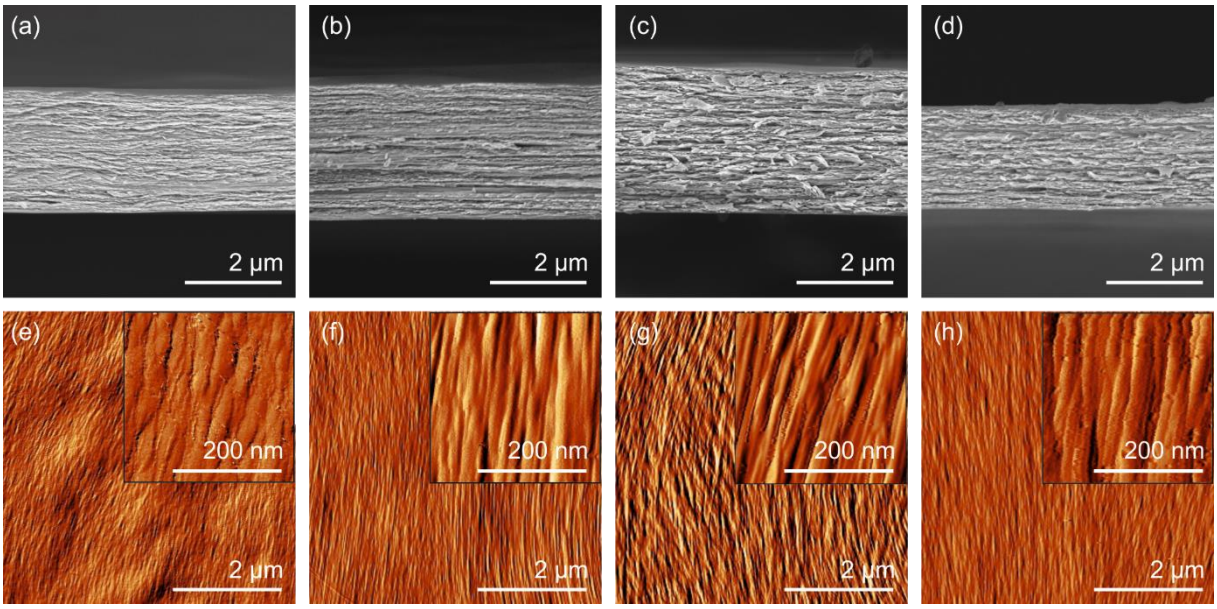

Figure S1. (a)-(d) SEM cross-section images of paper's fracture surface for (a) V_2O_5-1/PT, (b) V_2O_5-2/PT, (c) V_2O_5-3/PT and (d) V_2O_5-4/PT. (e)-(h) AFM amplitude images with an inset of higher magnification of the paper's surface for (e) V_2O_5-1/PT, (f) V_2O_5-2/PT, (g) V_2O_5-3/PT and (h) V_2O_5-4/PT.

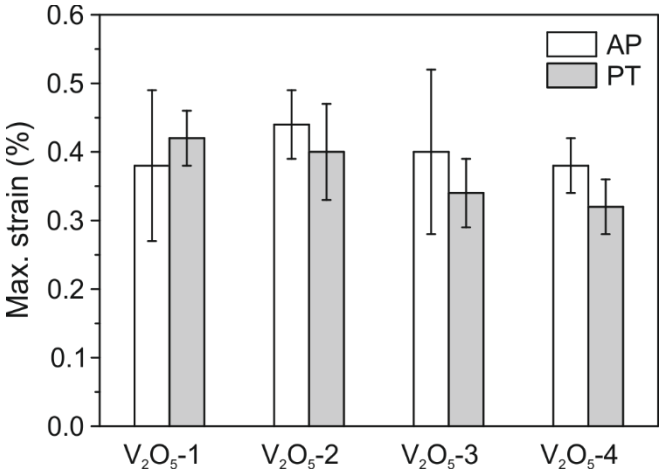

Figure S2. Determined maximum strain for AP and PT samples obtained from nanotensile tests.

2.6 Acknowledgements

The authors thank the group of Prof. Spatz of the Max-Planck-Institute in Stuttgart for equipment use and technical support and R. Segar for proofreading. The financial support provided by DFG (BU2713/2-1), Vector Stiftung (SVG-ID:0090018) and Landesgraduiertenförderung is highly appreciated.

2.7 References

[1] A. Moretti, S. Passerini, *Adv. Energy Mater.* **2016**, *6*, n/a.

[2] J. Liu, X. Wang, Q. Peng, Y. Li, *Adv. Mater.* **2005**, *17*, 764.

[3] Y. Yue, H. Liang, *Adv. Energy Mater.* **2017**, *7*, n/a.

[4] C. Liu, F. Li, L.-P. Ma, H.-M. Cheng, *Adv. Mater.* **2010**, *22*, E28.

[5] J. Livage, *Chem. Mater.* **1991**, *3*, 578.

[6] S. J. Park, J. S. Ha, Y. J. Chang, G. T. Kim, *Chem. Phys. Lett.* **2004**, *390*, 199.

[7] A.-M. Cao, J.-S. Hu, H.-P. Liang, L.-J. Wan, *Angew. Chem. Int. Ed.* **2005**, *44*, 4391.

[8] C. O'Dwyer, V. Lavayen, S. B. Newcomb, M. A. S. Ana, E. Benavente, G. González, C. M. S. Torres, *J. Electrochem. Soc.* **2007**, *154*, K29.

[9] Z. Burghard, A. Leineweber, P. A. van Aken, T. Dufaux, M. Burghard, J. Bill, *Adv. Mater.* **2013**, *25*, 2468.

[10] V. Petkov, P. N. Trikalitis, E. S. Bozin, S. J. L. Billinge, T. Vogt, M. G. Kanatzidis, *J. Am. Chem. Soc.* **2002**, *124*, 10157.

[11] X. Huang, X. Rui, H. H. Hng, Q. Yan, *Part. Part. Syst. Charact.* **2015**, *32*, 276.

[12] S. Tepavcevic, H. Xiong, V. R. Stamenkovic, X. Zuo, M. Balasubramanian, V. B. Prakapenka, C. S. Johnson, T. Rajh, *ACS Nano* **2012**, *6*, 530.

[13] W. Luo, J.-J. Gaumet, L. Mai, *MRS Commun.* **2017**, *7*, 152.

[14] G. Sai Gautam, P. Canepa, W. D. Richards, R. Malik, G. Ceder, *Nano Lett.* **2016**, *16*, 2426.

[15] N. Jayaprakash, S. K. Das, L. A. Archer, *Chem. Commun.* **2011**, *47*, 12610.

[16] S. Gu, H. Wang, C. Wu, Y. Bai, H. Li, F. Wu, *Energy Storage Mater.* **2017**, *6*, 9.

[17] G. Gu, M. Schmid, P.-W. Chiu, A. Minett, J. Fraysse, G.-T. Kim, S. Roth, M. Kozlov, E. Muñoz, R. H. Baughman, *Nat. Mater.* **2003**, *2*, 316.

[18] J. Livage, *Solid State Ion.* **1996**, *86*, 935.

[19] Muster J., Kim G. T., Krstić V., Park J. G., Park Y. W., Roth S., Burghard M., *Adv. Mater.* **2000**, *12*, 420.

[20] J. Bullot, O. Gallais, M. Gauthier, J. Livage, *Appl. Phys. Lett.* **1980**, *36*, 986.

[21] T. Szörényi, K. Bali, I. Török, I. Hevesi, *Thin Solid Films* **1984**, *121*, 29.

[22] Q. Liu, Z.-F. Li, Y. Liu, H. Zhang, Y. Ren, C.-J. Sun, W. Lu, Y. Zhou, L. Stanciu, E. A. Stach, J. Xie, *Nat. Commun.* **2015**, *6*, 6127.

[23] J. S. Sakamoto, B. Dunn, *J. Electrochem. Soc.* **2002**, *149*, A26.

[24] R. Sinko, S. Keten, *J. Mech. Phys. Solids* **2015**, *78*, 526.

[25] N. V. Medhekar, A. Ramasubramaniam, R. S. Ruoff, V. B. Shenoy, *ACS Nano* **2010**, *4*, 2300.

[26] C. Sanchez, F. Babonneau, R. Morineau, J. Livage, J. Bullot, *Philos. Mag. Part B* **1983**, *47*, 279.

[27] N. Agmon, *Chem. Phys. Lett.* **1995**, *244*, 456.

3 Binder-free V_2O_5 Cathode for High Energy Density Rechargeable Aluminum-ion Batteries

(reprinted with permission of MDPI 2020)

Achim M. Diem, Bernhard Fenk, Joachim Bill and Zaklina Burghard

Abstract

Nowadays, research on electrochemical storage systems moves into the direction of post-lithium-ion batteries, such as aluminum-ion batteries, and the exploration of suitable materials for such batteries. Vanadium pentoxide (V_2O_5) is one of the most promising host materials for the intercalation of multivalent ions. Here, we report on the fabrication of a binder-free and self-supporting V_2O_5 micrometer-thick paper-like electrode material and its use as the cathode for rechargeable aluminum-ion batteries. The electrical conductivity of the cathode was significantly improved by a novel in-situ and self-limiting copper migration approach into the V_2O_5 structure. This process takes advantage of the dissolution of Cu by the ionic liquid-based electrolyte, as well as the presence of two different accommodation sites in the nanostructured V_2O_5 available for aluminum-ions and the migrated Cu. Furthermore, the advanced nanostructured cathode delivered a specific discharge capacity of up to ~170 mAh g^{-1} and the reversible intercalation of Al^{3+} for more than 500 cycles with a high Coulomb efficiency reaching nearly 100%. The binder-free concept results in an energy density of 74 Wh kg^{-1}, which shows improved energy density in comparison to the so far published V_2O_5-based cathodes. Our results provide valuable insights for the future design and development of novel binder-free and self-supporting electrodes for rechargeable multivalent metal-ion batteries associating a high energy density, cycling stability, safety and low cost.

3.1 Introduction

The rising demand for advanced energy storage systems, e.g., rechargeable metal-ion batteries, with a high energy density requires novel electrode materials and fabrication concepts to fulfill crucial requirements for their application. Those requirements include a high storage capacity and current density, as well as long-term stability, low cost and sustainability [1–3]. In this context, lithium-ion batteries (LIBs) have been in the focus of research due to their high energy densities and wide electrochemical potential window [4]. However, lithium is a highly reactive metal and its natural resources are quite limited [5,6]. Therefore, attention has shifted toward different mono- and multivalent ions as a substitution for lithium [7]. Among this, aluminum is especially promising as it is the third most abundant element in the earth's crust, less hazardous and reactive compared to alkali metals. In addition, the three-electron redox couple of aluminum leads to a high theoretical gravimetric and volumetric capacity of 2980 mAh g^{-1} and 8063 mAh cm^{-3}, respectively, rendering it for high energy density metal-ion batteries [8,9]. While the working principle of rechargeable aluminum-ion batteries (AIBs) has been clarified to some extent [8], the ongoing development faces several challenges. This includes identifying suitable electrolytes, current collectors and additives. Ionic liquids, such as those imidazolium-based, mixed with aluminum chloride ($AlCl_3$) have shown some promise as electrolytes [10–15]. However, such electrolytes are not fully compatible with current collectors (e.g., Ni, Cu, Ta, Mo or stainless steel). In particular, stainless steel [16] and Cu [13,17,18] are dissolved by the imidazolium-based electrolytes. Furthermore, for achieving better stability of the current collectors the operating potential window needs optimization. For example, the use of Ni is limited because side reactions take place between the potentials 1.0 V and 1.5 V [17]. Similar to current collectors, binders, like polyvinylidene fluoride (PVDF), often have only limited stability against the electrolyte [12]. Finally, the role of carbon black, usually used as a conductive agent in conventionally prepared electrodes, should be taken into account. Considering all aspects, the aforementioned limitations highlight the need for suitable cell design, which includes the optimal pairing of a current collector with an electrolyte, as well as the development of self-supporting and binder-free electrodes for AIBs.

One promising class of cathode materials for AIBs are carbons—in particular, graphite and graphene—owing to their layered structure and good electrical conductivity. Lin et al. [10] reported a cathode comprised of a three-dimensional graphitic foam with a specific capacity of up to ~70 mAh g^{-1} at a current density of 4000 mA g^{-1} over more

than 7000 cycles. Another study, reports that an electrode made of natural graphite flakes and PVDF exhibits a specific capacity of ~110 mAh g^{-1} at a current density of 99 mA g^{-1}, and a Coulomb efficiency of ~98% [14]. Reduced graphene oxide combined with PVDF and carbon black has also been used as cathode material, yielding a capacity of 171 mAh g^{-1} at a current density of 100 mA g^{-1} [17]. Recently, Zhang and coworkers [19] could improve the capacity at high current densities of a graphene-based cathode by increasing the number of intercalation sites through the fabrication of an edge-rich graphene paper. In this manner, they reached for this cathode a specific capacity of 128 mAh g^{-1} at a current density of 2000 mA g^{-1}. In general, the ability to apply high current densities for carbonaceous-based electrodes is due to the higher diffusion rate enabled by the intercalated species, chloroaluminate ($AlCl_4^-$) [20]. Carbonaceous materials do not promote the splitting of $Al_2Cl_7^-$ into $AlCl_4^-$ and Al^{3+} at the electrode/electrolyte interface during the electrochemical reactions, thus $AlCl_4^-$ is inserted instead of Al^{3+} into the host lattice [12]. Besides the advantage of a high diffusion rate, only one electron is transferred per intercalated ion, which limits the storage capacity of such materials [8,10,14]. Therefore, active materials that provide the ability to supply Al^{3+} at the interface to the electrolyte would be beneficial to achieve a three-electron transfer resulting in higher storage capacities.

This encouraged the research on vanadium pentoxide (V_2O_5) as cathode material for AIBs, whose layered structure allows intercalation of various ions into the lattice, including Al^{3+} [2,3,21]. Another important advantage of V_2O_5 is its support to dissociate chloroaluminates into Al^{3+} at the interface between electrode and electrolyte [12]. Therefore, Al^{3+} species are available for insertion, which would offer a three-electron transfer leading to high storage capacities. A number of investigations have been done on crystalline V_2O_5 powder as cathodes for which storage capacities ranging between 30 and 305 mAh g^{-1} have been reported [11,13,15,22–24]. The relatively low values (compared to the theoretical capacity of 442 mAh g^{-1}) and the wide range of reached capacities are due to the different applied current densities, used current collectors and composition of the electrodes. The latter involves binders as mechanical support for the loose V_2O_5 powder, while adding carbon black to the electrode solves the issue of the poor electrical conductivity. However, they do not participate in the electrochemical reactions and increase the weight of the electrode, thus reducing the gravimetric storage capacity [12]. Moreover, the additives could react with the electrolyte leading to a decline of cycling stability. Despite these disadvantages, binder-free systems have

been rarely reported. One example is a cathode fabricated by the direct deposition of V_2O_5 on a Ni foam, which serves as mechanical support and current collector [12]. The foam structure of the cathode, as well as the close proximity of the V_2O_5 to Ni, resulted in an improved diffusion of the electrolyte through the network and enhanced charge exchange between V_2O_5 and Ni. Consequently, the electrochemical polarization is reduced compared to the binder containing electrodes. This resulted in high storage capacities of up to ~240 mAh g^{-1} at a current density of 44.2 mA g^{-1}. Although the approach is very promising, it still requires Ni as mechanical support, which affects the gravimetric storage capacity of the electrode. Therefore, an approach to fabricate a self-supporting, binder-free electrode and to increase the electrical conductivity of the active material would be of great importance for the development of advanced AIBs.

For the fabrication of self-supporting electrodes, micro- and nanostructuring is a versatile strategy to improve their mechanical stability. Recently, we demonstrated that self-supporting paper-like V_2O_5 films are accessible through self-assembly of V_2O_5 nanofibers from an aqueous suspension. The films are characterized by a high mechanical stability (tensile strength up to 116 MPa and Youngs modulus of 42 GPa), which can be tailored by the nanofiber length and water content. The mechanical stability and moderate in-plane electrical conductivity of ~2 S cm^{-1} render them as a suitable binder-free cathode for metal-ion batteries, such as LIBs [25]. However, in order to take full advantage of the three-electron transfer during Al^{3+} intercalation a higher electrical conductivity in-plane and out-of-plane would be beneficial. In this respect, doping with metal-ions is one plausible approach. It was reported that the electrical conductivity of nanofiber-based V_2O_5 xerogels can be significantly enhanced by Cu doping resulting in the formation of $Cu_xV_2O_5$ bronzes, while the layered structure of the nanofibers is preserved [26]. The increased electronic conductivity is correlated to the reduction of V^{5+} to V^{4+}, thus electron hopping as transport mechanism is more dominant. The electrochemical characterization of the bronzes directly deposited on the current collectors, revealed high lithium insertion rates resulting in high storage capacities and cycling stabilities [27,28]. Therefore, Cu doping is a suitable approach to improve the electrical conductivity of V_2O_5 thin films, which would render them as a promising binder-free and self-supporting cathode material for AIBs.

Here, we report the use of a binder-free and self-supporting cathode, for Al^{3+} intercalation, comprised of V_2O_5 nanofibers in the form of micrometer-thick self-supporting thin films. The cathode is fabricated via a self-assembly approach resulting

in an aligned and layered structure of high mechanical stability [25]. The optimized cell setup and testing parameters included a suitable current collector and a potential window that avoids undesired side reactions with the electrolyte. A Cu doping process was employed to enhance the electrical conductivity of the V_2O_5 cathode. Such cathodes enable the reversible intercalation of Al^{3+} for more than 500 cycles with a high specific discharge capacity of up to ~170 mAh g^{-1}, high Coulomb efficiencies and an energy density of 74 Wh kg^{-1}. Our findings provide novel guidelines and insights to overcome the faced challenges and proceed with the development of future AIBs.

3.2 Materials and Methods

Synthesis of V_2O_5 dispersion: The V_2O_5 nanofibers are synthesized by the mixing of ammonium meta-vanadate (1 g, Fluka, Munich, Germany) and an acidic ion-exchanger (10 g, Dowex 50WX8 50-100, Alfa Aesar, Kandel, Germany) in deionized water (200 mL) [21], which is heated for 10 min in an 80 °C oil bath. After slowly cooling down to room temperature, the dispersion of the nanofibers was aged for 42 days.

Fabrication of V_2O_5 cathodes: Silicon (100) wafers (p-type, Wacker, Sitronic AG, Munich, Germany) were used as substrates, which were cleaned with chloroform, acetone and ethanol each for 10 min in an ultrasonic bath and subsequently dried in a nitrogen flow. These Si wafers were placed in a petri dish and a 1:1 dilution (9 mL) of the V_2O_5 nanofiber dispersion and deionized water was added. After the complete evaporation of the water under ambient conditions, the V_2O_5 film was removed from the Si wafer in a water bath to obtain the self-supporting paper-like film. The self-supporting papers were dried in a two-step procedure in a climatic chamber (VC 7018, Vötsch, Industrietechnik GmbH, Balingen, Germany). The first step involved increasing the humidity from 50% to 80% and temperature from 25 °C to 40 °C in 15 min. The humidity, after one hour, was decreased to 20% within 10 h, while the temperature was kept constant for 15 h. The humidity of 20% was held for 4.5 h. Finally, the temperature was reduced to room temperature. The second step consisted of a temperature increase from 25 °C to 100 °C in 30 min, which was held for two hours followed by a temperature reduction to 25 °C in 30 min.

Microstructural characterization: For microstructural investigations, scanning electron microscopy (SEM, Zeiss Ultra 55, Zeiss GmbH, Oberkochen, Germany) and transmission electron microscopy (TEM, Philips CM200-FEG, Thermo Fisher, Hillsboro, OR, USA) equipped with an EDX (CM200, EDAX, Thermo Fisher, Hillsboro, OR, USA) at 200 kV system also for selected area diffraction (SAD) and atomic force microscopy (AFM, MultiMode 8, Nanoscope V, Bruker, Santa Barbara, CA, USA), were used. The TEM lamellae were prepared by an SEM-FIB system (1540 XB CrossBeam, Zeiss GmbH, Oberkochen, Germany). X-ray diffraction was performed by a PXRD (Rigaku Smartlab, Neu-Isenburg, Germany) in Bragg–Brentano geometry using copper K_α radiation, an acceleration voltage of 40 kV and a current of 30 mA in the range of 5°–40° with 0.02° as step size.

Electrical characterization: The out-of-plane electrical conductivity was determined via a two-point configuration (SourceMeter 2400, Keithley, Cleveland, Ohio, USA).

Electrochemical characterization: For the cell assembly in an argon-filled glovebox (Labmaster SP, MBraun, Garching, Germany) Swagelok™ union connections made of PTFE were used with stainless steel contacts. The contacts were protected from the electrolyte either by a commercial PE foil or by a Ta plate, which was glued with silver paste (Plano GmbH, Wetzlar, Germany) on top of the contact. The remaining steel part was coated with clear lacquer (Swingcolor, BAHAG AG, Mannheim, Germany) (Figure S6, Supporting Information). The V_2O_5 cathode was sputtered from both sides with a gold layer (35 nm, SCD 040, Balzers Union) to reduce the contact resistance toward the current collector. As the doping source, a 25 µm thick Cu foil (purity 99.98%, Sigma-Aldrich Chemie GmbH, Taufkirchen, Germany) was used with a diameter 1/3 smaller than the diameter of the V_2O_5 cathode. An 8 µm thick Al foil (purity 99%, Sigma Aldrich) was used as anode and 6 layers of glass fiber membrane (Grade 934-AH, Whatman, Sigma Aldrich) as separator, and 1-ethyl-3-methylimidazolium chloride mixed with aluminum chloride in the ratio of 1:1.5 (IoLiTec Ionic Liquids Technologies, Heilbronn, Germany) was set as electrolyte. Galvanostatic charge/discharge tests were carried out with 25, 50, 100, 200 and 500 mA g^{-1} as current densities in the voltage range of 0.2–1.1 V. Therefore, the cells were held for at least 2 h in open-circuit conditions. Cyclic voltammetry was performed in the voltage window of 0.02–1.5 V and 0.2–1.1 V, respectively, with a sweep rate of 0.1 mV s^{-1}. Electrochemical impedance spectroscopy was carried out with a frequency range of 0.1–10^6 Hz and an amplitude of 10 mV. The determined EIS data were fitted using an equivalent circuit model (R_1 + R_2/C_2 + W_d) including R_1 as contact resistance, R_2 as bulk resistance, C_2 the bulk capacitance and W_d as Warburg element. The stability tests of Ta and Cu were carried out by CV in potential windows 0.02–2.5 V and 0.2–1.1 V with scan rates of 1 mV s^{-1} and 0.1 mV s^{-1}. All measurements were performed on electrochemical test stations (VSP300, Biologic and 660C, CH Instruments, Seyssinet Pariset, France).

3.3 Results and Discussion

A binder-free and self-supporting cathode for AIBs was fabricated from nanocrystalline V_2O_5 nanofibers. The nanofibers are obtained via the sol–gel method and grow via an anisotropic polycondensation reaction resulting in a rectangular cross-section of the nanofiber with a height of ~1.5 nm and 10–20 nm in width [21]. They are composed of a bilayered chain-like arrangement of VO_5 polyhedrons, separated by a water molecule layer that ensures an interlayer distance of up to 1.77 nm [21,29]. Such distance is large enough to accommodate ions or even small molecules [2,21]. The length of the nanofibers is in the range of several micrometers and can be adjusted by the storage temperature and the age of the nanofibers solution [25,30]. In this study, the used V_2O_5 nanofibers have a length of approximately 2 µm.

The presence of functional surface groups, e.g., hydroxyl- and oxo-groups attached to the nanofibers promote their self-assembly via hydrogen bond formation into self-supporting micrometer-thick paper-like thin film (Figure 1a). The self-assembly results in a good in-plane alignment of the nanofibers (Figure 1b), within an ordered layered structure as the cross-section reveals, shown in Figure 1c. This highly ordered structure, made of bendable nanofibers caused by their high aspect ratio, leads to mechanical flexibility of the films that allows shaping them into any desired form (Figure 1d). Furthermore, the mechanical properties of the films can be tailored by thermal treatment, which supports the formation of oxygen bridges between the nanofibers and thus reinforcing the entire structure [31]. Therefore, the paper-like thin films were thermally treated at 100 °C. The annealing temperature of 100 °C was chosen in order to achieve a compromise between water content and preserving the structural integrity of the nanofibers. Specifically, the presence of water is important, since water molecules keep a necessary distance between the layers. This distance is of great importance for ion insertion. Furthermore, the water molecules could shield the high charges of intercalated Al^{3+} leading to a faster shuttling of the ions into the host lattice, as proven for the co-intercalation of water and magnesium ions [32]. The hydration state of $V_2O_5 \cdot n\ H_2O$ defines the interlayer distance of the V_2O_5 bilayer [21], which was investigated by X-ray diffraction (XRD). The XRD pattern (Figure 1e) of the annealed self-supporting paper-like thin film reveals one clear reflection at 8.98°, which correlates to an interlayer distance of 0.984 nm and the hydration state n = ~1.15. For this work, we used such thermally treated films as self-supporting and binder-free cathodes for AIBs. A defined micro- and nanostructure of such electrodes should

provide accessible intercalation sites and short diffusion paths for the Al^{3+}, thus positively contribute to the kinetic properties of the electrode.

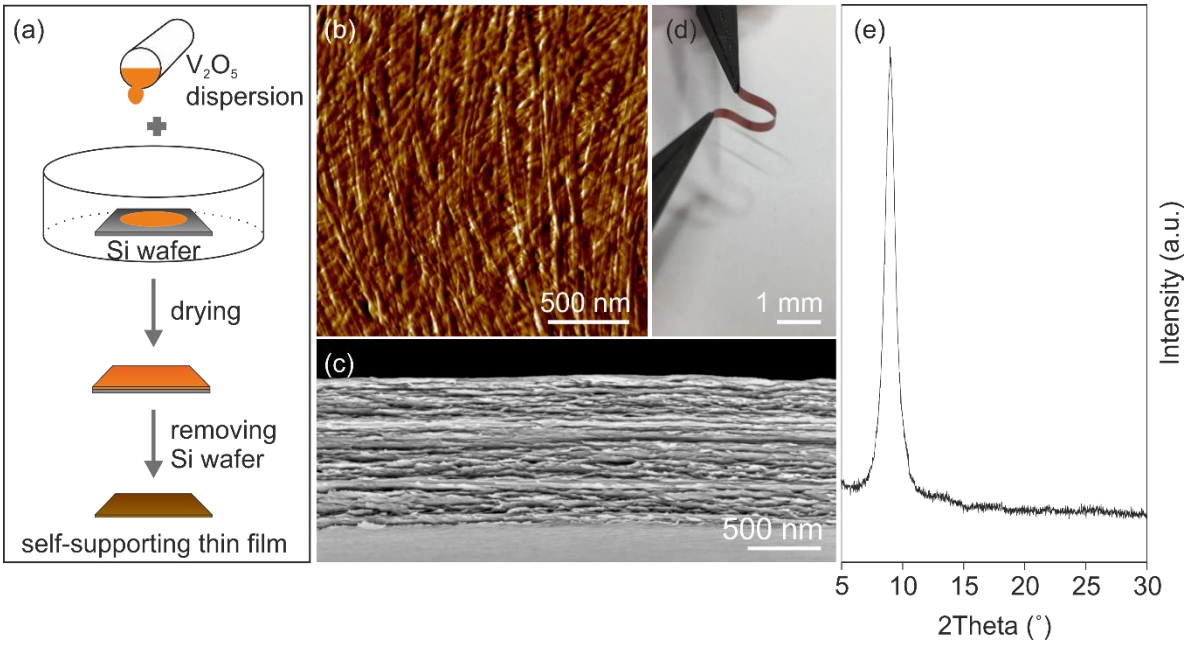

Figure 1. (**a**) Schematic illustration of vanadium pentoxide (V_2O_5) thin film preparation. A Si wafer is placed in a beaker that is filled up with the V_2O_5 dispersion. Drying at ambient conditions and removing the Si wafer from the V_2O_5 thin film results in the self-supporting V_2O_5 paper-like thin film. (**b**) AFM image of the paper-like surface showing the nanofiber alignment. (**c**) SEM image of the V_2O_5 paper revealing a layered structure. (**d**) Shaped V_2O_5 paper showing the flexibility. (**e**) XRD pattern of the V_2O_5 paper.

It was shown that the electrical conductivity of V_2O_5 xerogels comprised of nanofibers doped with silver or copper is enhanced by more than two orders of magnitude [26]. Accordingly, we improve the conductivity of our V_2O_5 cathode material by a one-step doping approach. This approach takes advantage of the synergy of the dissolution of Cu by the imidazolium-based ionic liquid electrolyte [10,12,14], and the Cu migration into the V_2O_5 cathode. Based on the fact that Cu corrosion in this electrolyte takes place around 1.5 V vs. Al/Al^{3+} [18], we performed electrochemical testing with 1.5 V as cut-off potential, insuring the Cu dissolution and thereby the doping approach. In conclusion, the one-step approach is comprised of the simultaneous doping of the cathode by Cu and electrochemical intercalation of the Al^{3+}. Our binder-free and self-supporting V_2O_5 cathode was placed on a copper foil, which acts as a dopant source. Aluminum foil

was employed as the counter electrode and glass fiber membranes as separator. A mixture of 1-ethyl-3-methylimidazolium chloride ([EMIM]Cl]) and aluminum chloride ($AlCl_3$) was used as electrolyte at a ratio of 1:1.5, which guarantees the presence of $AlCl_4^-$ and $Al_2Cl_7^-$ complexes [10]. For our studies, we used a Swagelok-type cell with stainless steel contacts, protected by commercial polyethylene (PE) foil to avoid reactions with the electrolyte.

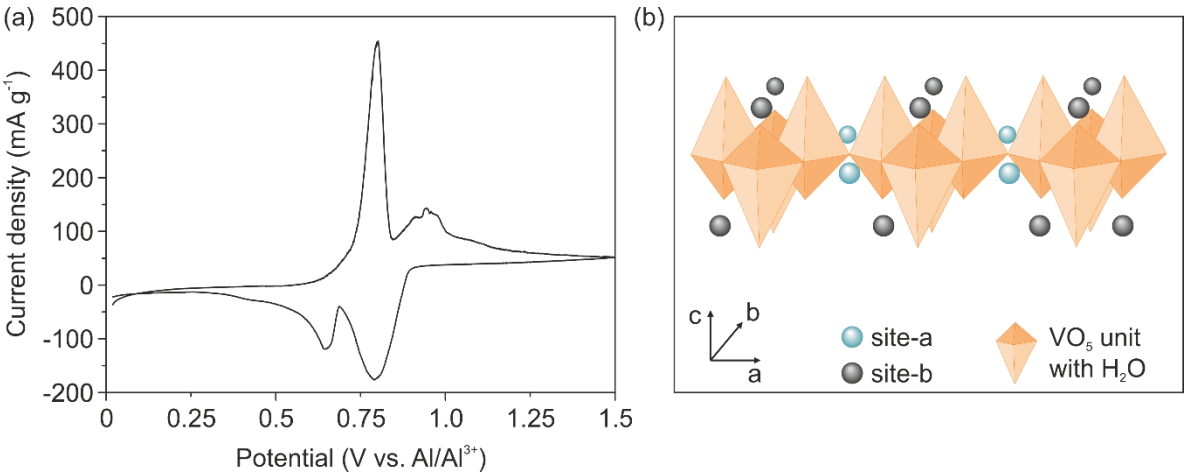

Figure 2. (**a**) Cyclic voltammetry curve of the second cycle at a scan rate of 0.1 mV s^{-1} revealing two de-/intercalation potentials. (**b**) Schematic illustration of the two different intercalation sites near the planar oxygen atom (site-a) and close to the apical oxygen atom (site-b) of the VO_5 units.

Cyclic voltammetry (CV) measurements reveal reversible ion intercalation, as shown in Figure 2a. This result indicates that the electrical conductivity of the cathode is enhanced by the Cu doping and is high enough to support Al^{3+} intercalation. Specifically, two distinct intercalation potentials at 0.79 V and 0.64 V and de-intercalation potentials of 0.80 V and 0.94 V are visible. The intercalation potentials are higher than those reported for binder-free Ni-V_2O_5 electrodes (0.6 V), revealing the impact of reduced electrochemical polarization due to the absence of the binders [12]. Moreover, the two observed de-/intercalation peaks might be correlated to the two different intercalation sites found for V_2O_5 structures, reported for the intercalation of Li^+ and Mg^{2+} [33]. In particular, the higher intercalation potential is correlated to the insertion of the ions at inner layer sites of the VO_5 unit (site-a in Figure 2b), which is in the vicinity of the square planar oxygen atoms. Likewise, the lower intercalation potential is correlated to the insertion of the ions at places close to the apical oxygen atom of the VO_5 unit (site-b in Figure 2b). The CV curve further reveals a stronger peak

at higher intercalation potential, indicating that the inserted Al^{3+} prefers intercalation on the inner layer sites (site-a). An explanation for this phenomenon could be that this site offers four-fold coordination by the oxygen atoms thus a better charge accommodation of the intercalated ion [34].

A simplified reaction mechanism of the de-/intercalation processes in V_2O_5 is presented in Figure 3. In general, Al^{3+} is stripped from the Al anode during the discharge process (Figure 3a) and forms with $AlCl_4^-$ and the larger complex $Al_2Cl_7^-$, which splits into $AlCl_4^-$ and Al^{3+} at the interface between the electrolyte and the cathode. Thereby, Al^{3+} is available and subsequently intercalated into the V_2O_5 host lattice. The following simplified reactions occur during the intercalation process:

$$\text{Anode: } Al - 3\ e^- \rightarrow Al^{3+}, \quad (1)$$

$$\text{Cathode: } V_2O_5 + x\ Al^{3+} + 3\ e^- \rightarrow Al_xV_2O_5, \quad (2)$$

During the charging process, the de-intercalation of Al^{3+} occurs (Figure 3b) leading to the formation of an $Al_2Cl_7^-$ complex at the interface between the electrolyte and the cathode. The formed $Al_2Cl_7^-$ complex dissociates on the anode side to $AlCl_4^-$ and metallic Al. The latter is subsequently deposited on the Al anode. Therefore, the de-intercalation reactions occur according to:

$$\text{Anode: } 4\ Al_2Cl_7^- + 3\ e^- \rightarrow Al + 7\ AlCl_4^-, \quad (3)$$

$$\text{Cathode: } Al_xV_2O_5 - 3\ e^- \rightarrow V_2O_5 + x\ Al^{3+}, \quad (4)$$

The reversibility of the stripping (Equation (1)) and deposition (Equation (3)) reaction is directly connected to the ratio of [EMIM]Cl to $AlCl_3$ and the resulting acidity of the electrolyte. In order to achieve the required acidity, the ratio has to be in the range between 1:1 and 1:2 that the aluminum stripping and deposition is guaranteed [23].

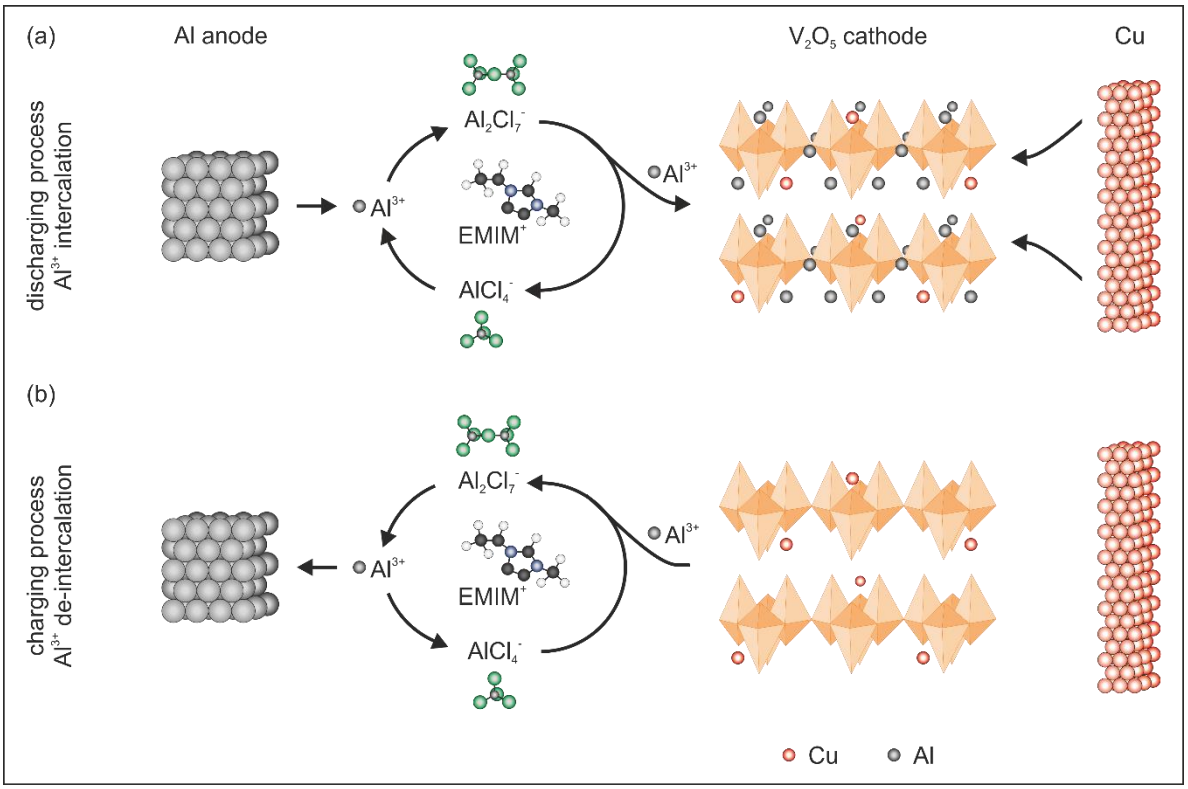

Figure 3. Simplified schematic representation of the occurring reactions during the discharge and charge process in the Cu doped V_2O_5 cathode. (**a**) In the discharge process, Al^{3+} are electrochemically stripped from the Al anode and are intercalated into the V_2O_5 cathode via an intermediate $Al_2Cl_7^-$ complex. (**b**) During the charge process, Al^{3+} is de-intercalated from the V_2O_5 cathode forming the intermediate $Al_2Cl_7^-$ complex and metallic Al is deposited on the anode.

Based on the fact that Cu is dissolved by the electrolyte, as indicated in Figure 3b, we conclude that Cu doping occurs during the electrochemical processes in the V_2O_5 cathode. To this end, the migrated Cu can react irreversibly with V_2O_5 to a $Cu_xV_2O_5$ bronze, similar to the chemically doped $Cu_xV_2O_5$ bronze [26]. To characterize the impact of Cu doping on the structure and morphology of our cathode, we performed ex-situ XRD analysis of the cathodes after the second and eighth CV cycles. The obtained XRD patterns (Figure S1, Supporting Information) reveal that the main reflection around 9.00°, observed for the pristine cathode (Figure 1d**),** is also present for the Cu doped V_2O_5 cathode after both CV measurements. This indicates that the structural integrity, e.g., V_2O_5 sheet stacking, of our cathode is preserved. However, a small shift toward higher 2θ values (from 8.98° to 9.44°) reveals that the distance between the V_2O_5 sheets is reduced. The reason might be the attraction between the positive Cu ions and the negatively charged V_2O_5 sheets [26]. In addition, the chemical stability of

the V_2O_5 paper-like electrode in the used ionic liquid-based electrolyte is shown by the unchanged XRD patterns of the electrode after cycling. If any reaction would take place, then the cycling of the electrodes would not be possible. To visualize the electrode stability, digital images of the V_2O_5 immersed in the ionic liquid-based electrolyte after 0 min, 30 min, 60 min and 20 h were taken (Figure S2, Supporting Information).

To further investigate the influence of the migrated Cu on the morphology of the V_2O_5 cathode, we conducted ex-situ transmission electron microscopy (TEM) on the cathode after discharge cycles. The ex-situ TEM investigation of a cathode after two cycles of CV showed the typical layered V_2O_5 sheet stacking (Figure S3, Supporting Information). Contrary to that, the TEM micrographs of a cathode cycled for eight CV cycles (Figure 4a) revealed the regular stacking of V_2O_5 sheets and homogenously distributed precipitations (dark regions in Figure 4) over the complete cross-section. The precipitates are spherically shaped (Figure 4b) with an average diameter of 9.18 ± 3.30 nm (Figure 4c) and have crystalline lattice planes with a lattice distance in the range of 0.2–0.3 nm (Figure 4d). Such precipitates are assumed to nucleate at voids or places of imperfect alignment of the nanofibers, or at the connection points between nanofibers, which serve as heterogeneous nucleation spots for the forming precipitates. Their local chemical composition is determined by energy-dispersive X-ray spectroscopy (EDX). A high amount of vanadium and copper detected by elemental mapping relates to the Cu migrations into the V_2O_5 cathode. A quantitative analysis (Table S1, Supporting Information) revealed that the V_2O_5 matrix (bright region in Figure 4) exhibits a nearly 1:1 ratio of vanadium to copper. In contrast, the precipitates show a significantly higher amount of copper than vanadium with a vanadium-to-copper ratio of 3:4. Thus, we conclude that the migrating Cu results in doping of our V_2O_5 cathode and forms Cu-enriched precipitates (see Figures S4 and S5, Supporting Information), which are evenly distributed over the entire cathode.

Our conclusion was corroborated by the determination of the electrical conductivity, which is significantly enhanced by the Cu doping [26]. The electrical conductivity of our V_2O_5 cathodes is comprised of an electronic and ionic contribution, specifically electron hopping along the vanadium centers (V^{5+} and V^{4+}) and proton diffusion alongside the nanofiber's surface, respectively [21,25]. The in-plane electrical conductivity in the range of 2 S cm^{-1} [25,31], which is parallel to the V_2O_5 sheets, is approximately five orders higher than the out-of-plane electrical conductivity [31]. In the present work, we

investigated the out-of-plane conductivity of our V_2O_5 cathodes, as it is the limiting factor for electrochemical testing. We determined a value of $0.16 \cdot 10^{-6}$ S cm^{-1} for the cathode before CV cycling, whereas after CV cycles two and eight, the electrical conductivity was $0.07 \cdot 10^{-2}$ S cm^{-1} and $0.16 \cdot 10^{-2}$ S cm^{-1}, respectively. This significant increase by four orders of magnitude verifies several facts. First, the Cu doping is accompanied by an enhancement of the electrical conductivity. Second, that already after two CV cycles a certain amount of Cu is migrated, although not visible by TEM. Finally, the two-fold increase in conductivity of the cathode after eight cycles compared to the values after two cycles underline the significant impact of the Cu doping on the electrical conductivity.

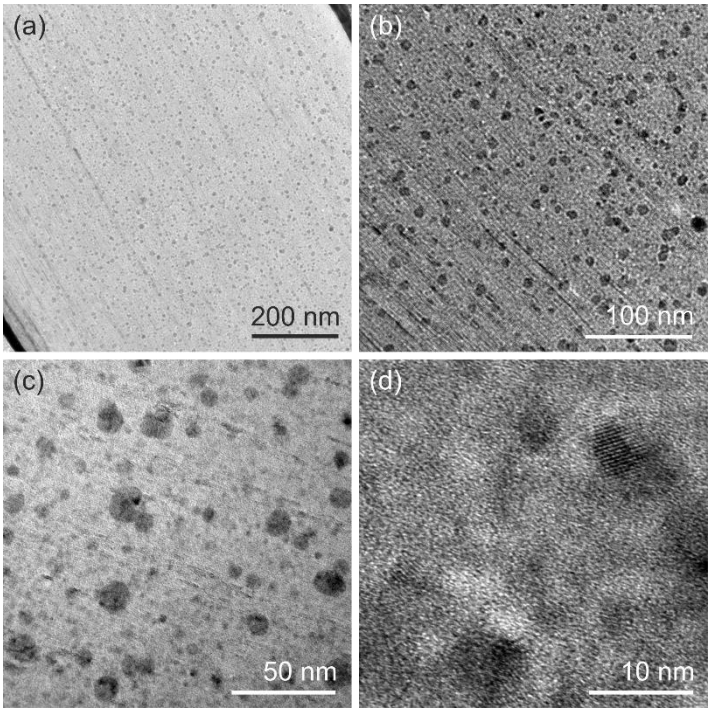

Figure 4. Images obtained during ex-situ TEM investigation of the cross-section of a cathode cycled eight times during CV investigations. An overview of the investigated cross-section is shown in image (**a**). The black regions correspond to the Cu-rich precipitations, which are homogeneously distributed over the complete sample. The images (**b**)–(**d**) are the higher magnification spots from the image (**a**).

Based on all these findings, we further optimized our cell setup to avoid all undesirable side reactions. In this respect, Ta plates were fixed on the stainless steel contacts, which were subsequently coated with a clear lacquer to prevent any reaction between the stainless steel and the electrolyte (see Figure S6, Supporting Information).

Furthermore, we determined the optimal voltage window, where no side reactions attributed to the cell setup occur. For that purpose, CV was performed in a Ta vs. Ta plate configuration in the voltage range of 0.02–2.5 V with a scan rate of 1 mV s^{-1} (Figure S7, Supporting Information). The CV curve revealed that side reactions start at ~1.5 V, attributing to either the Ta plate or the clear lacquer corrosion. In addition, some minor side reactions were observed below 0.2 V. In addition, it was important to determine at which potential Cu dissolution starts in order to use Cu as a doping source. Therefore, we performed electrochemical measurements for the bare Cu foil as the cathode (Figure S8, Supporting Information). We observed weak peaks on the CV curves for the potentials above 1.0 V, which we correlated to the side reactions or Cu corrosion. Accordingly, the potential window from 0.2 V to 1.1 V was set for the electrochemical investigations. It supports the required dissolution of Cu, circumvents severe Cu corrosion and assures the stability of the current collectors. From the electrochemical impedance spectroscopy (EIS) measured on the Ta vs. Ta plate configuration, the aluminum-ion conductivity was estimated to be 5.54 × 10^{-3} S cm^{-1}, which is comparable to other reported electrolytes [35,36].

This optimized cell setup was used for electrochemical characterization of the pure V_2O_5 cathode (p-V_2O_5) as a reference and the Cu doped V_2O_5 cathode (V_2O_5/Cu). The source for Cu was a micrometer-thick Cu foil placed between the cathode and Ta plate. The respective CV curves obtained after two cycles for both cathodes are presented in Figure 5a. The CV curve of p-V_2O_5 reveals no electrochemical performance at all, due to the absence of any intercalation and de-intercalation peaks. On the contrary, the CV curve of V_2O_5/Cu reveals two clear intercalation peaks at potentials of 0.82 V and 0.65 V and two de-intercalation peaks at 0.79 V and 0.96 V. This underlines the importance of the Cu presence on the electrochemical performance of the cathode, which is only due to the enhanced electrical conductivity of the cathode. To prove that the Cu is not electrochemically active within the used voltage window, additional tests were done. Corresponding CV and galvanostatic charge/discharge measurements with bare Cu as the cathode are presented in Figures S8–10 (Supporting Information). Likewise, the potentials peaks also indicate that the two intercalation positions are occupied by the ions, as explained before site-a and site-b. Here, it should be noted that we observed two de-/intercalation potentials, while in all other reported works only one potential is stated. In this respect, the intercalation potential at 0.65 V is similar to the reported insertion potentials for various crystalline V_2O_5-based AIBs [11–13,23], while

the second intercalation potential at 0.82 V is comparable to the observed insertion potential of 0.8 V, reported by Chiku et al. [15], for the cathode made of an amorphous V_2O_5/C composite mixed with carbon black and polytetrafluoroethylene (PTFE). The presence of the two available intercalation sites, and hence two observed peaks for our V_2O_5 paper-like thin film, conforms with the morphology comprised of crystalline nanofibers and their amorphous arrangement. Therefore, we could conclude, that the intercalation site-a (0.82 V) is attributed to the amorphous fraction and site-b (0.65 V) to the nanofibers. It would be of great interest to investigate the relationship between structure and intercalation sites in more detail to pronounce the advantage of such self-assembled binder-free electrodes even more.

Furthermore, we observed a change of the position of the inter- and de-intercalation potentials after the fourth and eighth cycles for V_2O_5/Cu, as shown in Figure 4b. The peak positions are slightly shifted to lower potentials indicating that less energy for ion diffusion through the material is required. This can be explained by the fact that the interfaces between the cathode material and the electrolyte are generated and subsequently stabilized by the ongoing inter- and de-intercalation processes. The CV curves in Figure 5b reveal a decrease of the current density for the intercalation potential of ~0.65 V and the de-intercalation potential of ~0.79 V. These potentials are referred to as intercalation site-b close to the apical oxygen atom. The same place was reported to be favorable as an accommodation site for the Cu used to dope V_2O_5 xerogels [34]. Thus, CV curves reveal the irreversible incorporation of Cu into our cathode during electrochemical cycling. In respect to that, our results show that Cu migrates into site-b, thus fewer intercalation sites for Al^{3+} are available. In contrast to that, the peak intensity for the intercalation potential of 0.82 V and de-intercalation potential of 0.96 V (corresponding to the site-a) is unchanged. This indicates the reversible Al^{3+} insertion and that the intercalation at site-a, close to the planar oxygen atom of the VO_5 units, is favorable.

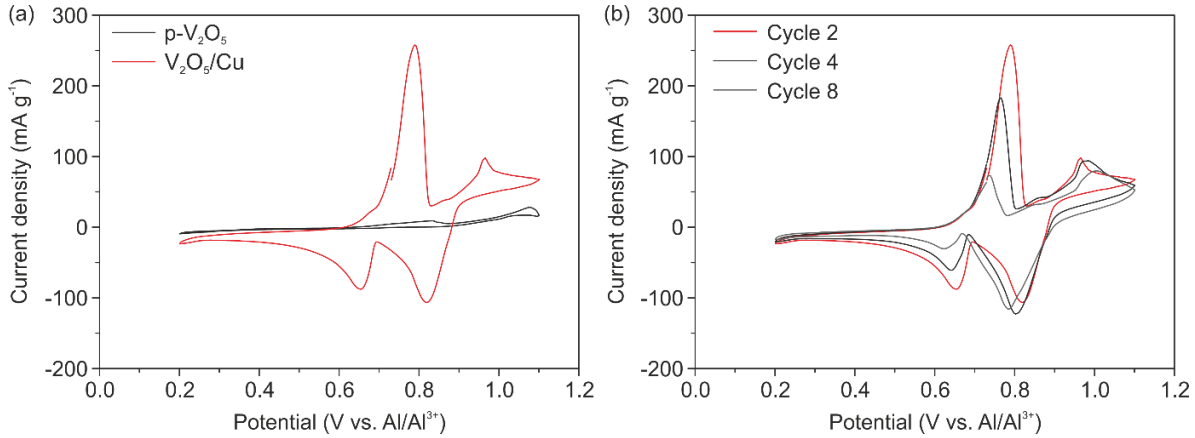

Figure 5. Cyclic voltammetry curves at a scan rate of 0.1 mV s^{-1} of (**a**) second cycles for p-V_2O_5 and V_2O_5/Cu revealing the importance of the migrated Cu, as well as for (**b**) cycles 2, 4 and 8 of V_2O_5/Cu.

The CV measurements were complemented by galvanostatic charge/discharge tests to determine the specific storage capacity of our binder-free and self-supporting V_2O_5 cathodes. Figure 6a represents the specific discharge capacity as a function of cycle numbers for p-V_2O_5 revealing a very low discharge capacity of up to ~2.3 mAh g^{-1} at the lowest applied current density of 25 mA g^{-1}. Low discharge capacities are found for all current rates and no clear intercalation and de-intercalation plateaus can be seen (Figure 6b). These results verify that p-V_2O_5 shows no electrochemical performance at all, as already indicated by the CV measurements (Figure 5a). The low discharge capacity compared to other reported V_2O_5-based cathodes, with carbon black as a conductive agent, is attributed to the very low electrical conductivity of p-V_2O_5, made only of active material.

This becomes even more obvious by the comparison of the specific storage capacities of p-V_2O_5 and V_2O_5/Cu cathodes (Figure 6c). Prior to all charge/discharge experiments, the cells undergo a pre-cycling of 50 cycles at a current rate of 1000 mA g^{-1}. This pre-cycling for V_2O_5/Cu was used to induce the Cu migration into the V_2O_5 cathode (Figure S11, Supporting Information). In order to further investigate the impact of the migrated Cu on the electrical conductivity, the pre-cycling was coupled with EIS measurements. Therefore, for the first 20 cycles and cycles 30, 40 and 50 EIS was performed in the fully charged and discharged state. The gained EIS data were fitted with a respective equivalent circuit model and the bulk resistance was determined (Figure S12, Supporting Information). The resistance in the fully discharged state is not influenced by the pre-cycling and stays constant. However, in the fully charged

state, where Al^{3+} is absent, the resistance shows a continuous decrease. This decrease of resistance or increase in conductivity is attributed to the migrated Cu.

For all investigated current densities (Figure 6c) much higher discharge capacities for V_2O_5/Cu were determined. The corresponding capacity profiles for the first cycles as a function of the current density are shown in Figure 6d. In particular, we determined specific discharge capacities of 6 mAh g^{-1}, 16 mAh g^{-1}, 27 mAh g^{-1}, 53 mAh g^{-1} and 155 mAh g^{-1} with the corresponding Coulomb efficiencies of 99%, 88%, 81%, 72% and 65% at current densities of 500 mA g^{-1}, 200 mA g^{-1}, 100 mA g^{-1}, 50 mA g^{-1} and 25 mA g^{-1}. Figure 6e shows the specific charge, discharge capacities and Coulomb efficiency over cycles for the applied current densities. The initial Coulomb efficiency (ICE) is about 95% at a current density of 500 mA g^{-1}. The low Coulomb efficiencies and the visible potential drops in Figure 6d indicate minor side reactions. The side reactions at this potential are caused neither by the electrolyte nor by the V_2O_5 electrode electrochemical stability (Figure S2, Supporting Information). However, they are mainly attributed to Cu dissolution. These side reactions are more pronounced during the charging process at low current densities thus resulting in a decrease of the Coulomb efficiency to 70%.

The diagram in Figure 6e further reveals that the storage capacities and Coulomb efficiencies are stabilized over time by comparing the first and second blocks of the five current densities. Moreover, it can be seen that our cathode delivers a constant discharge capacity of ~25 mAh g^{-1} at a current density of 100 mA g^{-1}. Furthermore, the Coulomb efficiency close to 100% underlines the high reversibility toward Al^{3+} intercalation and cycling stability over 300 cycles. The latter is attributed to the ability of the cathode's microstructure to effectively accommodate the stresses upon cycling.

The impact of the migrated Cu on the electrical conductivity of the cathodes is evident through the discharge capacities of p-V_2O_5 and V_2O_5/Cu. Specifically, for the highest current density, the discharge capacity of V_2O_5/Cu is about 150% higher than for p-V_2O_5. We assume that the Cu migration in V_2O_5/Cu is a self-limiting process. By cycling, a plateau is observed, referring to saturation of migrated Cu within the cathode. The saturation is due to the irreversible migration of Cu, thus the number of available intercalation sites is reduced. Furthermore, the Cu saturation is accompanied by the enhancement of the electrical conductivity of the cathode. This enables an enhanced de-/intercalation of Al^{3+} of up to 0.38 mole aluminum per V_2O_5 unit. Moreover, optimization of the dopant source would be beneficial to achieve a compromise

between the amount of migrated Cu, the resulting enhanced electrical conductivity and availability of Al^{3+} intercalation sites.

To validate our fabrication concept of a binder-free and self-supporting V_2O_5 cathode to other cathode materials for AIB, the energy density was calculated and summarized in Table S2 (Supporting Information). We determined an energy density for V_2O_5/Cu of 74 Wh kg^{-1} (173 mAh g^{-1} at 25 mA g^{-1}), which is comparable to carbon-based electrode materials [10,14,17,19]. Furthermore, the energy density of our V_2O_5/Cu is superior to the values of other reported V_2O_5-based cathodes [11-13,15,22,23]. This improvement is partly attributed to the omission of binders during the fabrication of the electrodes. In addition, these electrodes, exclusively made of active material, are assembled in a uniform aligned microstructure. The advantage of this microstructure is its improved accessibility for ions throughout the entire electrode. Therefore, the Cu migration and the Al^{3+} de-/intercalation are facilitated, which strongly enhances the electrical conductivity and the storage capacity, respectively. These findings provide a big leap into the development of novel advanced electrodes for AIB.

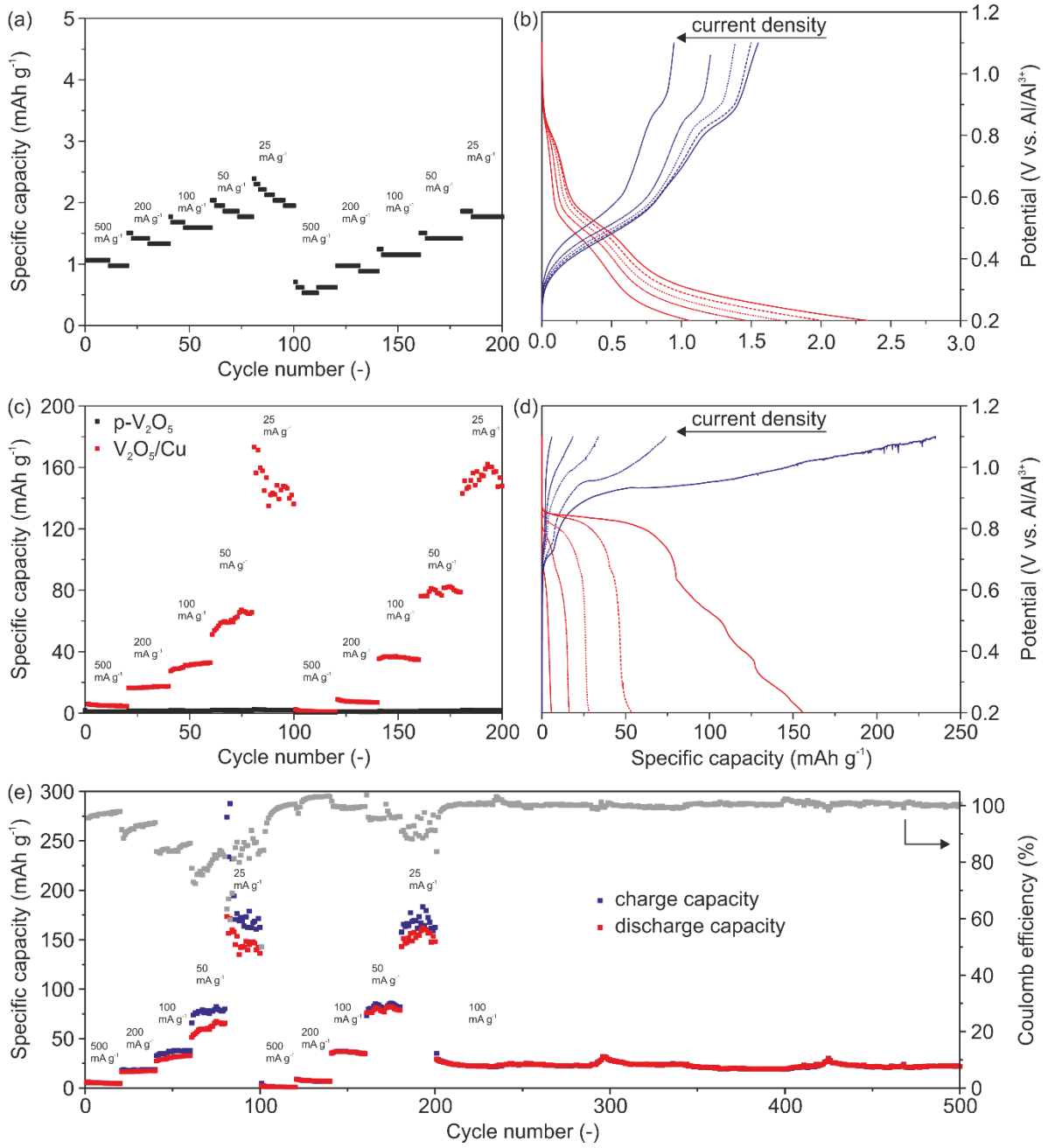

Figure 6. Galvanostatic charge and discharge measurements with various current densities, as displayed in the diagrams. Specific storage capacity as a function of the cycle number. (**a**) Specific discharge capacity of p-V_2O_5. (**b**) Potential vs. specific capacity plot for p-V_2O_5. (**c**) Specific discharge capacity of p-V_2O_5 and V_2O_5/Cu. (**d**) Potential vs. specific capacity plot for the V_2O_5/Cu. (**e**) Charging/discharging capacity and Coulomb efficiency of the V_2O_5/Cu cathode.

3.4 Conclusions

We successfully obtained a self-supporting and binder-free paper-like thin film comprised of V_2O_5 nanofibers doped with Cu to enable its application as cathode material for AIBs. The Cu doping relies on the dissolution of Cu by the ionic liquid-based electrolyte and the subsequent Cu migration into the V_2O_5 films. While the Cu migration notably increases the electrical conductivity of the films, their high mechanical stability and flexibility that originates from their regular, hierarchical layer structure is effectively preserved after Cu doping. The self-limiting doping process guarantees a high density of accommodation sites available for Al^{3+} and simultaneously facilitates their intercalation. Hereby, a specific discharge capacity of ~170 mAh g^{-1} at a current density of 25 mA g^{-1} is reached, leading to an energy density of 74 Wh kg^{-1}. Furthermore, a Coulomb efficiency of almost 100% is achieved over 300 cycles at an even higher current density. Overall, our findings provide valuable insights on how to overcome current challenges in the development of AIBs. The demonstrated approach may be transferable to the fabrication of other batteries that operate with multivalent cations.

3.5 Supporting Information

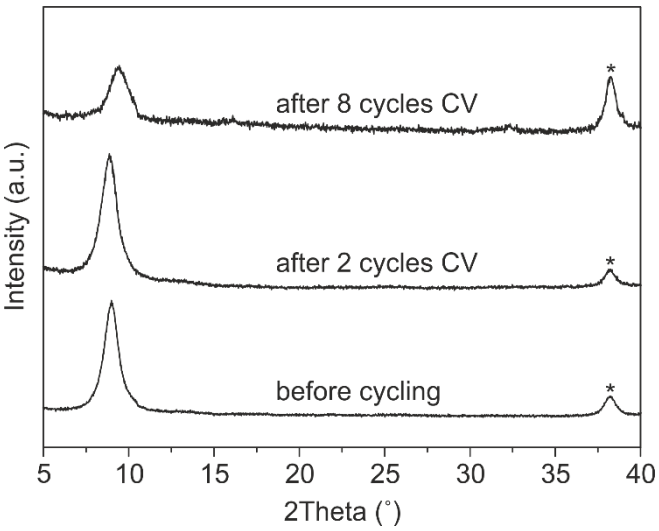

Figure S1: XRD patterns before and after electrochemical cycling (two and eight cycles CV). The intensity is normalized to one Au reflection (*).

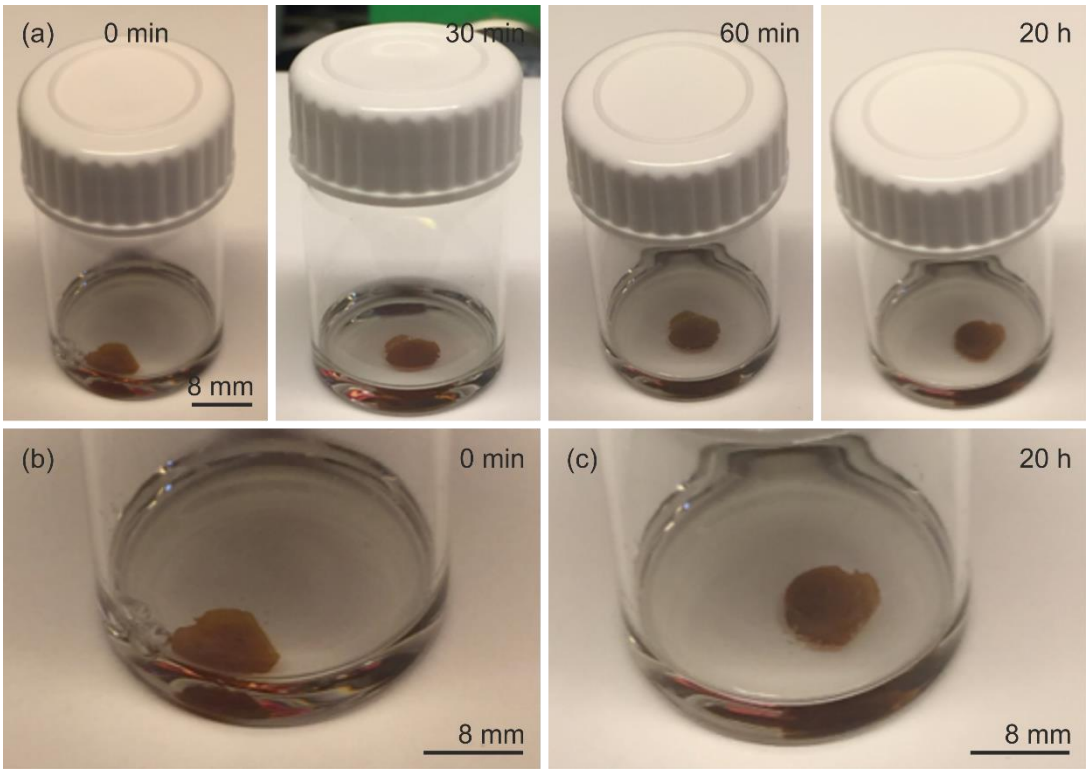

Figure S2. Digital images of the V_2O_5 paper like electrode immersed in the ionic liquid-based electrolyte after indicated time, demonstrating the electrode's chemical stability.

Diem et al., Nanomaterials, 2020, 10, 247.

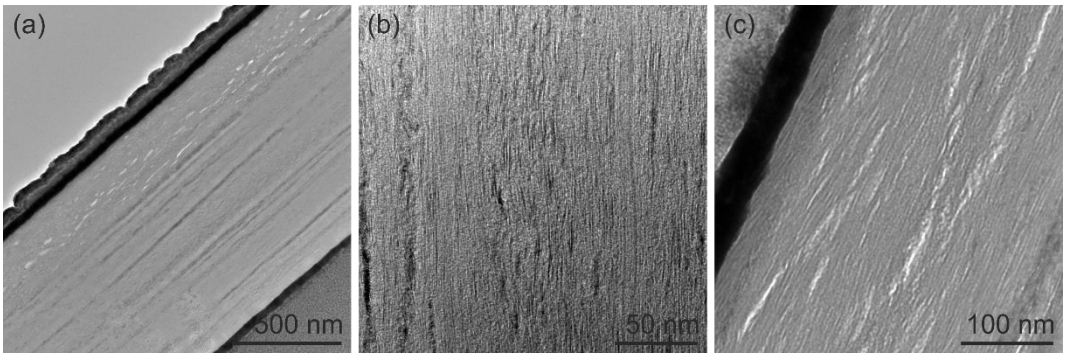

Figure S3: Ex-situ TEM images of the cross-section of a cathode, which was cycled for two cycles CV.

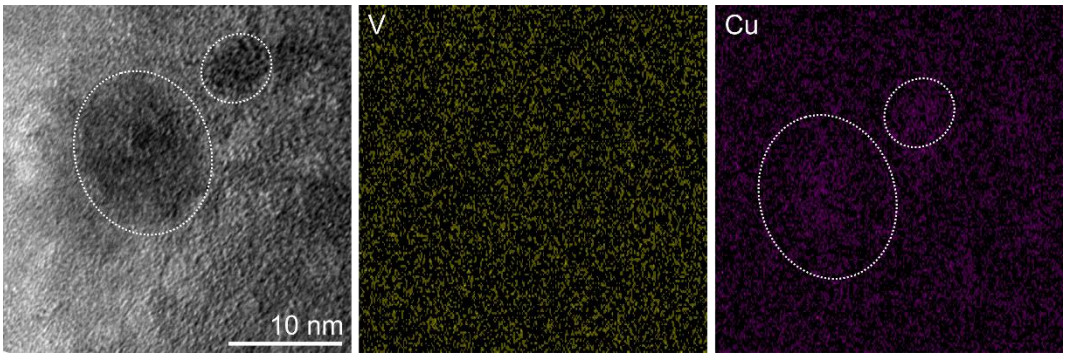

Figure S4: Ex-situ TEM investigation coupled with elemental mapping of the cross-section of a cathode, which was cycled for eight cycles CV.

Table S1: Ex-situ EDX analysis of a V_2O_5 cathode after 8 cycles of CV

	O (at%)	**Al (at%)**	**Cu (at%)**	**V (at%)**
Matrix	41.3	0.4	28.4	29.9
Precipitate	30.2	0.3	40.8	28.7

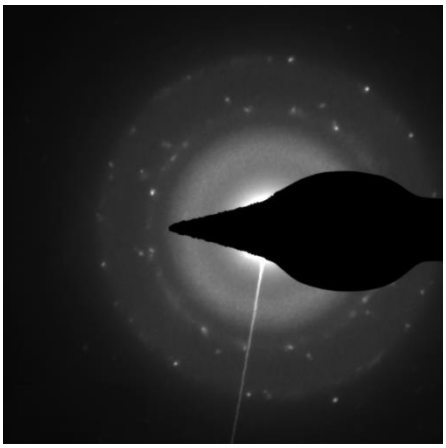

Figure S5: Electron diffraction reveals a ring-like diffraction pattern indicating a polycrystalline structure of our V_2O_5/Cu cathode. In particular, the (001) orientation of V_2O_5 can be observed. The residual diffraction rings might be referred to the Cu doped V_2O_5 and the nanocrystalline Cu-enriched precipitates.

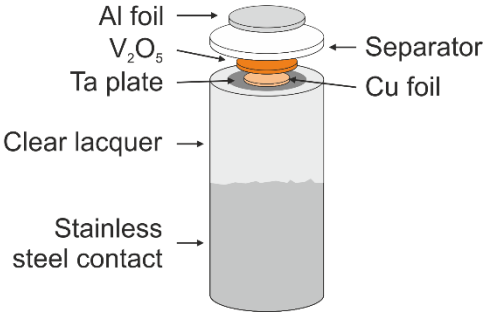

Figure S6: Scheme of the cell setup used for the electrochemical characterization of V_2O_5/Cu. The setup includes fixing a Ta plate on the stainless steel contact. The remaining stainless steel parts are coated with clear lacquer to avoid contact with the electrolyte.

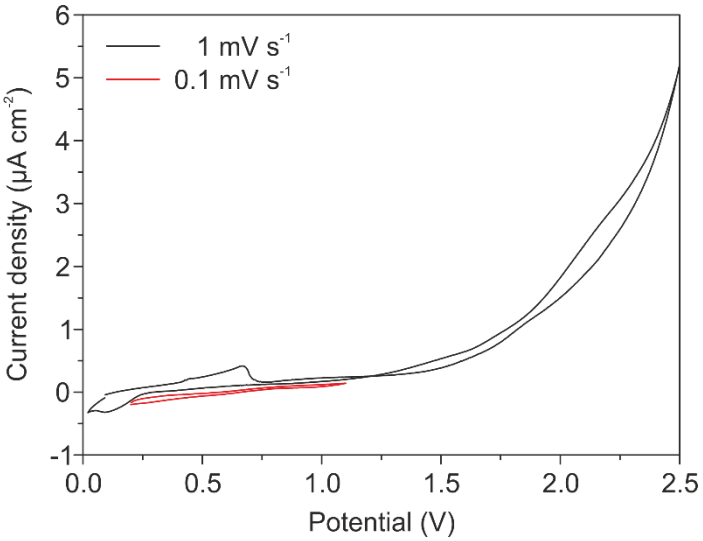

Figure S7: Stability test with Ta *vs.* Ta plate configuration, separated by one layer of glass fiber membrane. CV measurement in the potential window of 0.02-2.5 V and a scan rate of 1 mV s^{-1} (black line) revealing side reaction from ~1.5 V on. CV in the potential range of 0.2-1.1 V and a scan rate of 0.1 mV s^{-1} (red line) exhibiting no side reactions.

CV and galvanostatic charge/discharge measurements with bare Cu as cathode were performed to prove that the Cu is not electrochemically active. The visible peaks of the first CV cycle (Figure S8) reveal the dissolution of the native Cu oxide layer. From the cycle three on, only the anodic peak can be seen, which strongly decreases by further cycling. This indicates that the pure copper is dissolved by electrolyte and might be complexed by the chloroaluminate anions in the electrolyte. For the cycle five, almost no peaks are visible, revealing that the dissolution process is slow down and the saturation of Cu in the electrolyte is reached. Furthermore, the comparison of the CV curves of V_2O_5/Cu and bare Cu as cathode (Figure S9) reveals that the CV curve of V_2O_5/Cu shows distinct anodic and cathodic peaks, while the Cu dissolution is only an underlying reaction. This clearly excludes that the Cu shows electrochemical activity. Therefore, we prove that the electrochemical activity is attributed only to the intercalation of Al^{3+} and the redox reactions of V_2O_5. This was further verified by glavanostatic charge/discharge tests, showing that Cu only contributes in a negligible amount to the storage capacity (Figure S10). Moreover, the electrochemical activity of V_2O_5 towards the reversible intercalation of Al^{3+} was confirmed by Gu and coworkers.[1]

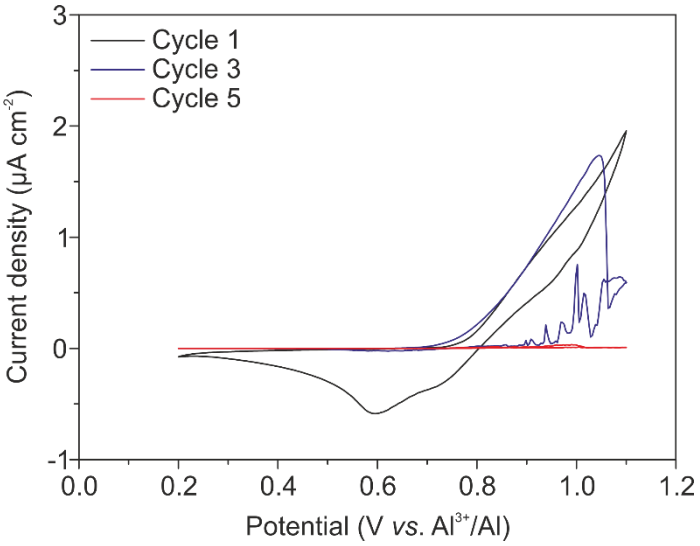

Figure S8: CV curves for a bare Cu cathode at a scan rate of 0.1 mV s^{-1}.

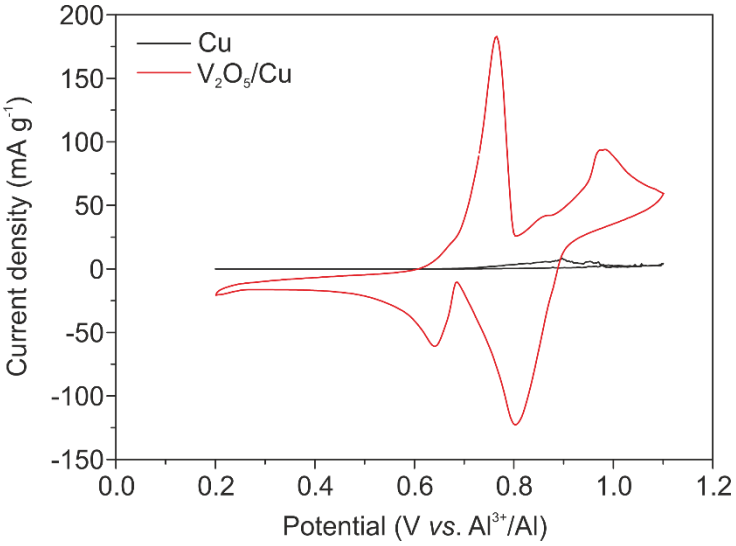

Figure S9: Comparison of CV curves of the 4th cycle for V_2O_5/Cu and bare Cu as cathode showing that the Cu dissolution is an underlying process.

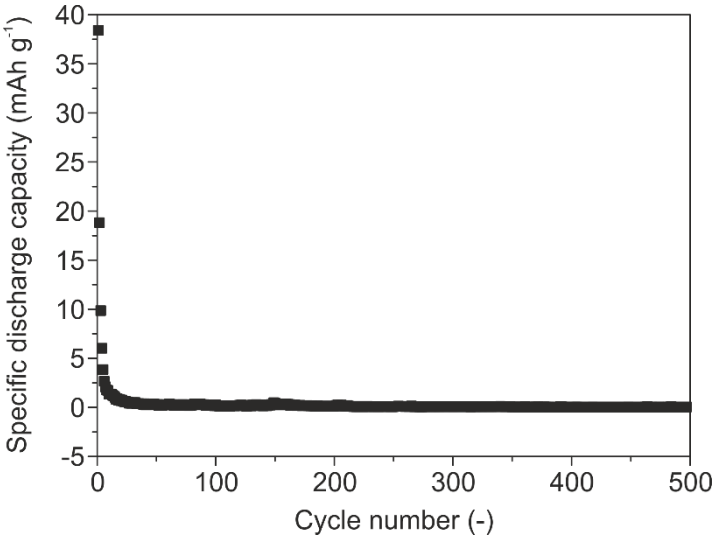

Figure S10: Specific discharge capacity obtained from galvanostatic charge/discharge tests with a current density of 100 mA g^{-1} of a bare Cu cathode vs. Al/Al^{3+}.

Diem et al., Nanomaterials, 2020, 10, 247.

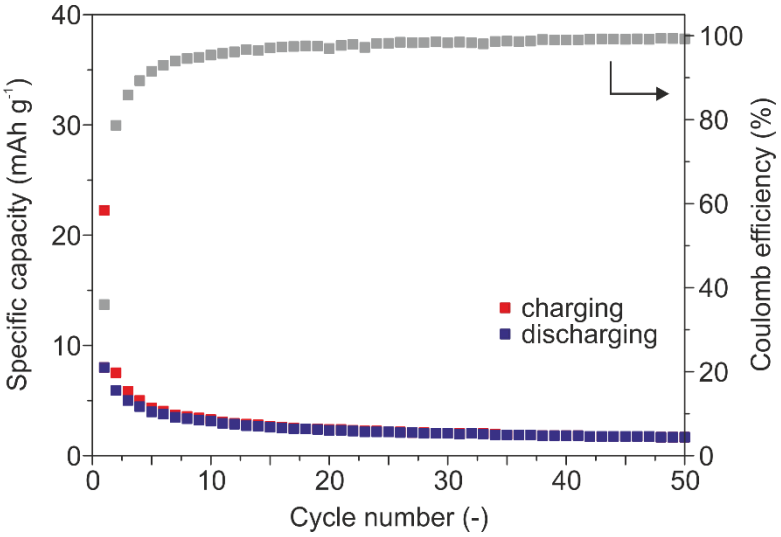

Figure S11: Storage capacity and Coulomb efficiency of the pre-cycling for 50 cycles at a current density of 1000 mA g^{-1}.

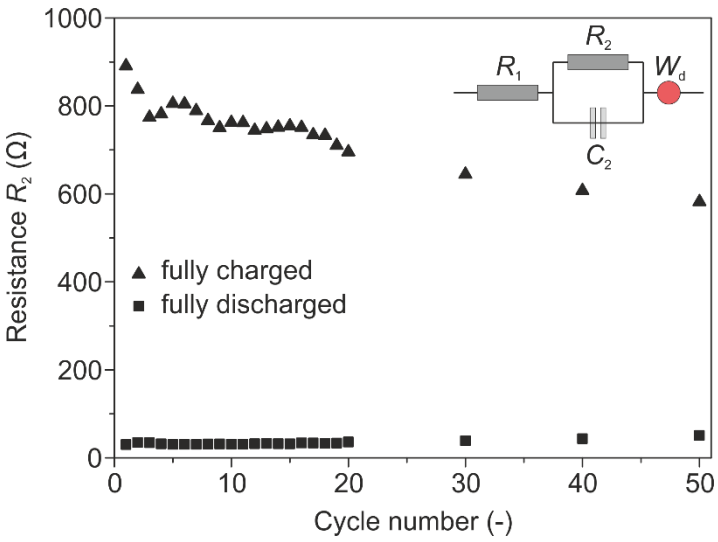

Figure S12: Investigation of the pre-cycling for 50 cycles at a current density of 1000 mA g^{-1}. At fully charged and discharged states EIS measurements were performed, which are fitted with the presented equivalent circuit model. R_1 represents the contact resistance, R_2 the bulk resistance, C_2 the bulk capacitance and W_d the Warburg element.

Table S2: Comparison of active material ratio, specific storage capacity, intercalation plateaus, current density and energy density for different electrode materials.

Electrode material	**Amount of active material (%)**	**Specific discharge capacity (mAh g^{-1})**	**Intercalation plateaus (V)**	**Current density (mA g^{-1})**	**Energy density (Wh kg^{-1})**
Carbon-based					
Smajic et al., Small, 2018.[2]	80	171		100	170
Lin et al., Nature, 2015.[3]	100	65	2.25-2.0 & 1.9-1.5	n.a.	40
Wang et al., Nature Communications, 2016.[4]	90	110	2.25-2.0 & 1.9-1.5	99	69
Zhang et al., Energy Storage Materials, 2018.[5]	100	106	2.2-2.0 & 1.7-1.5*	4000	43***
V_2O_5-based					
Wang et al., ACS Applied Materials & Interfaces, 2014.[6]	100	239	0.7-0.5*	44	48***
Chiku et al., ACS Applied Materials & Interfaces, 2015.[7]	90	150*	1.0-0.7*	5	45***
Gu et al., Energy Storage Materials, 2017[1]	90	107	0.75-0.5*	n.a.	27***
Wang et al., Advanced Energy Materials, 2017[8]	n.a.	32*	0.5-0.3*	100	6***

Wang et al., Journal of Materials Chemistry A, 2015.[9]	80	100*	0.5-0.4**	10	10***
Jayaprakash et al., Chemical Communications, 2011.[10]	85	273	0.6-0.5*	125	12***
This work					
p-V_2O_5	100	2.3	0.87-0.75 & 0.58-0.48	25	0.37
V_2O_5/Cu	100	173	0.86-0.77 & 0.68-0.59	25	74

Remarks:

*estimated for the 1st cycle

**estimated for the 2nd cycle

***calculation is based on provided storage capacity and insertion potentials

References

[1] S. Gu, H. Wang, C. Wu, Y. Bai, H. Li, F. Wu, *Energy Storage Mater.* **2017**, *6*, 9.

[2] J. Smajic, A. Alazmi, N. Batra, T. Palanisamy, D. H. Anjum, P. M. F. J. Costa, *Small* **2018**, *14*, 1803584.

[3] M.-C. Lin, M. Gong, B. Lu, Y. Wu, D.-Y. Wang, M. Guan, M. Angell, C. Chen, J. Yang, B.-J. Hwang, H. Dai, *Nature* **2015**, *520*, 324.

[4] D.-Y. Wang, C.-Y. Wei, M.-C. Lin, C.-J. Pan, H.-L. Chou, H.-A. Chen, M. Gong, Y. Wu, C. Yuan, M. Angell, Y.-J. Hsieh, Y.-H. Chen, C.-Y. Wen, C.-W. Chen, B.-J. Hwang, C.-C. Chen, H. Dai, *Nat. Commun.* **2017**, *8*, 14283.

[5] Q. Zhang, L. Wang, J. Wang, C. Xing, J. Ge, L. Fan, Z. Liu, X. Lu, M. Wu, X. Yu, H. Zhang, B. Lu, *Energy Storage Mater.* **2018**, *15*, 361.

[6] H. Wang, Y. Bai, S. Chen, X. Luo, C. Wu, F. Wu, J. Lu, K. Amine, *ACS Appl. Mater. Interfaces* **2015**, *7*, 80.

[7] M. Chiku, H. Takeda, S. Matsumura, E. Higuchi, H. Inoue, *ACS Appl. Mater. Interfaces* **2015**, *7*, 24385.

[8] H. Wang, X. Bi, Y. Bai, C. Wu, S. Gu, S. Chen, F. Wu, K. Amine, J. Lu, *Adv. Energy Mater.* **2017**, *7*, 1602720.

[9] H. Wang, S. Gu, Y. Bai, S. Chen, N. Zhu, C. Wu, F. Wu, *J. Mater. Chem. A* **2015**, *3*, 22677.

[10] N. Jayaprakash, S. K. Das, L. A. Archer, *Chem. Commun.* **2011**, *47*, 12610.

3.6 Acknowledgments

The authors thank the group of J. Spatz and the Nanostructuring Lab of J. Weiss from the Max-Planck-Institutes in Stuttgart for equipment use and technical support, and the group of G. Schmitz from the Institute for Materials Science of the University of Stuttgart for using the TEM. The authors are thankful to T. Jahnke and R. Lawitzki for TEM assistance, T. Wörner for engineering support, M. Widenmeyer and L. Raafat for fruitful discussions and A. Schilling for experimental assistance. The financial support provided by the Vector Stiftung (project no.: 0090018) is highly appreciated.

3.7 References

[1] M. Armand, J.-M. Tarascon, *Nature* **2008**, *451*, 652.

[2] A. Moretti, S. Passerini, *Adv. Energy Mater.* **2016**, *6*, 1600868.

[3] J. Yao, Y. Li, R. C. Massé, E. Uchaker, G. Cao, *Energy Storage Mater.* **2018**, *11*, 205.

[4] M. S. Whittingham, *Chem. Rev.* **2004**, *104*, 4271.

[5] V. Etacheri, R. Marom, R. Elazari, G. Salitra, D. Aurbach, *Energy Environ. Sci.* **2011**, *4*, 3243.

[6] D. McNulty, D. N. Buckley, C. O'Dwyer, *J. Power Sources* **2014**, *267*, 831.

[7] P. Canepa, G. Sai Gautam, D. C. Hannah, R. Malik, M. Liu, K. G. Gallagher, K. A. Persson, G. Ceder, *Chem. Rev.* **2017**, *117*, 4287.

[8] G. A. Elia, K. Marquardt, K. Hoeppner, S. Fantini, R. Lin, E. Knipping, W. Peters, J.-F. Drillet, S. Passerini, R. Hahn, *Adv. Mater.* **2016**, *28*, 7564.

[9] S. K. Das, S. Mahapatra, H. Lahan, *J. Mater. Chem. A* **2017**, *5*, 6347.

[10] M.-C. Lin, M. Gong, B. Lu, Y. Wu, D.-Y. Wang, M. Guan, M. Angell, C. Chen, J. Yang, B.-J. Hwang, H. Dai, *Nature* **2015**, *520*, 324.

[11] S. Gu, H. Wang, C. Wu, Y. Bai, H. Li, F. Wu, *Energy Storage Mater.* **2017**, *6*, 9.

[12] H. Wang, Y. Bai, S. Chen, X. Luo, C. Wu, F. Wu, J. Lu, K. Amine, *ACS Appl. Mater. Interfaces* **2015**, *7*, 80.

[13] N. Jayaprakash, S. K. Das, L. A. Archer, *Chem. Commun.* **2011**, *47*, 12610.

[14] D.-Y. Wang, C.-Y. Wei, M.-C. Lin, C.-J. Pan, H.-L. Chou, H.-A. Chen, M. Gong, Y. Wu, C. Yuan, M. Angell, Y.-J. Hsieh, Y.-H. Chen, C.-Y. Wen, C.-W. Chen, B.-J. Hwang, C.-C. Chen, H. Dai, *Nat. Commun.* **2017**, *8*, 14283.

[15] M. Chiku, H. Takeda, S. Matsumura, E. Higuchi, H. Inoue, *ACS Appl. Mater. Interfaces* **2015**, *7*, 24385.

[16] L. D. Reed, E. Menke, *J. Electrochem. Soc.* **2013**, *160*, A915.

[17] J. Smajic, A. Alazmi, N. Batra, T. Palanisamy, D. H. Anjum, P. M. F. J. Costa, *Small* **2018**, *14*, 1803584.

[18] S. Wang, Z. Yu, J. Tu, J. Wang, D. Tian, Y. Liu, S. Jiao, *Adv. Energy Mater.* **2016**, *6*, 1600137.

[19] Q. Zhang, L. Wang, J. Wang, C. Xing, J. Ge, L. Fan, Z. Liu, X. Lu, M. Wu, X. Yu, H. Zhang, B. Lu, *Energy Storage Mater.* **2018**, *15*, 361.

[20] P. Bhauriyal, A. Mahata, B. Pathak, *Phys. Chem. Chem. Phys.* **2017**, *19*, 7980.

[21] J. Livage, *Chem. Mater.* **1991**, *3*, 578.

[22] H. Wang, X. Bi, Y. Bai, C. Wu, S. Gu, S. Chen, F. Wu, K. Amine, J. Lu, *Adv. Energy Mater.* **2017**, *7*, 1602720.

[23] H. Wang, S. Gu, Y. Bai, S. Chen, N. Zhu, C. Wu, F. Wu, *J. Mater. Chem. A* **2015**, *3*, 22677.

[24] J. R. González, F. Nacimiento, M. Cabello, R. Alcántara, P. Lavela, J. L. Tirado, *RSC Adv.* **2016**, *6*, 62157.

[25] A. M. Diem, A. Knöller, Z. Burghard, J. Bill, *Nanoscale* **2018**, *10*, 15736.

[26] F. Coustier, J. Hill, B. B. Owens, S. Passerini, W. H. Smyrl, *J. Electrochem. Soc.* **1999**, *146*, 1355.

[27] F. Coustier, G. Jarero, S. Passerini, W. H. Smyrl, *J. Power Sources* **1999**, *83*, 9.

[28] M. Giorgetti, S. Mukerjee, S. Passerini, J. McBreen, W. H. Smyrl, *J. Electrochem. Soc.* **2001**, *148*, A768.

[29] V. Petkov, P. N. Trikalitis, E. S. Bozin, S. J. L. Billinge, T. Vogt, M. G. Kanatzidis, *J. Am. Chem. Soc.* **2002**, *124*, 10157.

[30] S. J. Park, J. S. Ha, Y. J. Chang, G. T. Kim, *Chem. Phys. Lett.* **2004**, *390*, 199.

[31] Z. Burghard, A. Leineweber, P. A. van Aken, T. Dufaux, M. Burghard, J. Bill, *Adv. Mater.* **2013**, *25*, 2468.

[32] G. Sai Gautam, P. Canepa, W. D. Richards, R. Malik, G. Ceder, *Nano Lett.* **2016**, *16*, 2426.

[33] D. Imamura, M. Miyayama, *Solid State Ion.* **2003**, *161*, 173.

[34] M. Giorgetti, M. Berrettoni, W. H. Smyrl, *Chem. Mater.* **2007**, *19*, 5991.

[35] H. Lee, M. Yanilmaz, O. Toprakci, K. Fu, X. Zhang, *Energy Environ. Sci.* **2014**, *7*, 3857.

[36] C. Ferrara, V. Dall'Asta, V. Berbenni, E. Quartarone, P. Mustarelli, *J. Phys. Chem. C* **2017**, *121*, 26607.

Diem et al., Nanomaterials, 2020, 10, 247.

4 Creasing Highly Porous V_2O_5 Scaffolds for High Energy Density Aluminum-ion Batteries

(reprinted with permission of ACS 2020)

Achim M. Diem, Joachim Bill and Zaklina Burghard

Abstract

The growing demand for rechargeable metal-ion batteries with high energy densities requires innovative electrode design strategies. We address this challenge by exploring light and highly porous, binder-free scaffolds comprised of vanadium pentoxide (V_2O_5) nanofibers as the cathode material for aluminum-ion batteries (AIBs). The V_2O_5 scaffolds are fabricated by unidirectional ice-templating that gives the structure its anisotropic property of ordered channels for facilitated ion diffusion. The unique structure of the scaffolds provides high mechanical stability, despite their porosity of 99.9%. Creasing of such scaffolds results in a corrugated lamella arrangement and formation of contact points, yielding a significant enhancement of the electrical conductivity. The synergy of the electrical conductivity and the high specific surface area renders the creased scaffolds as a promising cathode material for AIBs, demonstrated by the reversible intercalation of Al^{3+}. Particularly, at high current densities of 500 mA g^{-1}, specific storage capacities up to 105 mAh g^{-1} are achieved, providing an energy density of 52 Wh kg^{-1}, which outperforms other V_2O_5- and carbon-based cathodes. Our results offer guidelines for the structuring of advanced electrode materials for high energy density metal-ion batteries, which boosts areal and gravimetric capacities.

Diem et al., ACS Applied Energy Materials, 2020, 3, 4033-4042. Reprinted with permission from American Chemical Society.

4.1 Introduction

Because of increasing market demand, the focal point of energy storage research is to develop advanced electrodes for metal-ion batteries, which deliver high energy density at high current densities.[1-3] To this end, a variety of electrochemically active materials have been investigated so far, demonstrating that adjusting their morphology and assembly into an electrode significantly impacts the specific storage capacity delivered at certain current densities.[4,5] One of the most promising and straightforward approaches is downscaling the electrochemically active material to the nanoscale. This approach helps to reduce the ion diffusion pathways and enhances the active surface area, resulting in enriched ion intercalation kinetics and electrode areal loading.[6,7] Accordingly, research has been steered in the aforementioned direction toward novel synthesis methods for nanosized electrode materials with powder morphology.[7] However, the benefits of nanosized electrode materials can only be reaped if the assembled electrodes are additive-free. This is a rather difficult task due to the poor intrinsic electrical conductivity of the so far synthesized electrode materials, and as a loose powder, they need mechanical support. Another promising route to achieve high energy density electrodes is to produce a porous electrochemically active material. The high surface area of those porous materials corresponds to a large electrode/electrolyte interface and an increased number of available intercalation sites. Accordingly, the delivered areal and gravimetric storage capacities are significantly enhanced.[8,9] Conversely, the disadvantage of the high porous electrode is its low tap density, resulting in low volumetric storage capacity. Consequently, the current challenge is to fabricate electrodes with nanosized building blocks of the electrochemically active material, specifically their assembly into structurally designed porous scaffolds for realizing high tap density electrodes that are self-supported, i.e., additive-free. To this end, high energy density and volumetric capacity electrodes can be achieved.

Among electrochemically active materials, extensive research has been devoted to vanadium pentoxide (V_2O_5) due to its various redox states and high theoretical storage capacity.[10] In addition, its applicability in multivalent metal-ion batteries, such as aluminum-ion batteries (AIBs), raises more interest. Several groups reported on the reversible insertion of Al^{3+} into V_2O_5 structures, reaching a broad range of storage capacities.[11-15] The latter is attributed to the usage of binders as a mechanical support for the loose V_2O_5 powder and carbon black as a conductive agent as well as engaged

current collectors. Specifically, it was reported that some current collectors and binders cause side reactions with the used ionic liquid-based electrolyte for AIBs.[8,16-18] To avoid such reactions, a selection of current collectors and the utilization of binder-free electrodes are required. In this respect, Wang and co-workers fabricated a binder-free electrode by deposition of V_2O_5 particles on a Ni foam that serves as a mechanical support and current collector. The electrode delivers a storage capacity of up to 240 mAh g^{-1} at a current density of 44.2 mA g^{-1}.[16] The notable enhancement of the electrochemical performance of such an electrode compared to the binder containing one is attributed to the good electrical contact, short diffusion pathways for Al^{3+}, and reduced electrochemical polarization. Although the reported gravimetric capacity of V_2O_5-based cathode materials is relatively high, the porous structure of the Ni foam certainly lowers the tap density, affecting their volumetric performance.

Moreover, special attention is paid to V_2O_5 gels made of nanofibers that are synthesized via a low-temperature sol–gel synthesis method.[10,19] The nanofibers are comprised of spacious bilayers, each composed of a chain-like structure of VO_5 units separated by water molecules.[19,20] The distance of the bilayer is large enough to accommodate not only small Li^+,[10,21,22] but also larger and multivalent ions, such as Na^+,[23,24] Mg^{2+},[25,26] Zn^{2+},[27,28] and Al^{3+}.[11,29] Furthermore, it was reported that electrochemical performance of aerogels is superior to xerogels due to the different interlayer spacing, fiber thickness, and porosity.[30]

To the best of our knowledge, there has been no research done by other groups on the fabrication of binder-free and self-supporting electrodes made of sol–gel derived V_2O_5. Recently, we published work on the fabrication of self-supporting two-dimensional (2D) paper-like electrodes made of highly aligned V_2O_5 sol–gel derived nanofibers. Such electrodes are compact, robust, and flexible. We prove that they are good for Li^+ and Al^{3+} ion intercalation.[31,32] We found that nanofiber length, hierarchical structuring, and electrode thickness are crucial for mechanical stability and electrochemical performance of such self-supporting electrodes. Moreover, to abstain from using carbon black, we developed an in situ Cu-doping method of the 2D self-supporting V_2O_5-based paper-like electrodes. The method takes advantage of the Cu dissolution by the ionic liquid-based electrolyte. Specifically, the Cu migrates into the V_2O_5 electrode, enhancing the electrical conductivity, enabling the reversible intercalation of Al^{3+}, and therefore delivering a high energy density.[32] However, the

areal capacity of such electrodes is relatively low. In this regard, assembling nanofibers into a porous three-dimensional (3D) structure would increase the areal capacity.

A promising method to precisely control and design the microstructure of porous V_2O_5 is ice-templating.[33] This method is based on the fast formation of the ice crystals that serve as a template to structure the nanofiber assembly. The formed ice crystals are subsequently removed by freeze-drying, resulting in a porous structure with the impression of the ice crystals.[34] Recently, we reported on highly porous V_2O_5 scaffolds, fabricated by this method.[35] Their unique structure, comprised of regularly stacked cavities arranged within lamellas with a centrosymmetric orientation, renders their excellent mechanical stability. The importance of such an ordered microstructure is highlighted by superior mechanical properties to scaffolds with randomly oriented pores.[35] By adjusting the temperature gradient, the freezing direction, and the concentration of the V_2O_5 dispersion, the scaffold's microstructure can be further tailored, thus improving the mechanical properties. Such a precisely tailored scaffold's microstructure renders it as a 3D self-supporting and binder-free electrode material.

However, besides the advantages of the porous scaffolds to accommodate the volume change during ion intercalation and their large electrode/electrolyte interface, the volume/weight ratio of the electrode plays a crucial role to meet their volumetric capacity. In this respect, the pore size and specific surface area should be considered. Smajic and co-workers highlighted the significance of the pore size distribution (micro/meso) on the electrochemical performance of porous reduced graphene oxide.[8] The superior electrochemical performance of the mesoporous to the microporous structure is attributed to the smaller pore volume and the increased number of intercalation sites due to the higher specific surface area. Furthermore, theoretical calculations indicate that nanoribbons and nanopores could incorporate more nanovoids within the electrode structure. In this manner, they attract and adapt more ions resulting in enhanced storage capacity.[36] Another way to increase the specific surface area of a thin-films-based electrode is their folding, as it creates layers separated by voids.[37] For example, folding of graphene-based freestanding films allowed the realization of a compact electrode with high areal capacity, while preserving the electrode's weight and volume. Furthermore, compression of an aerogel made of carbon nanotubes is another way to fabricate compact freestanding electrodes with high areal capacity.[38] Although some research has been done on the synthesis of porous electrodes and the tailoring of their pore morphology, still that of

porous self-supporting nanostructured electrodes remains a challenge. The main challenge is to achieve the synergy of the low pore volume and optimal micro-/mesoporosity with high specific surface area.

Here we report a method for the fabrication and structural design of 3D self-supporting binder-free electrodes with a porous structure that effectively combines high specific surface area with micro-/mesoporosity. Such porous nanostructured scaffolds exclusively made of V_2O_5 nanofibers are assembled by unidirectional ice-templating. Creasing the scaffolds under mechanical compression introduces a corrugated and folded lamella structure, which significantly enhances the electrical conductivity, rendering them as promising cathodes for AIBs. The improvement of the electrical conductivity involves the creation of contact points to ensure continuous and more effective charge transportation paths. The electrical conductivity is further enhanced by the in situ Cu-doping approach. Electrochemical testing revealed the reversible de/intercalation of Al^{3+} into the V_2O_5 host lattice. The synergy of the high surface area, the creased microstructure, and the enhanced electrical conductivity of the scaffolds resulted in high energy density at high current densities.

4.2 Results and Discussion

4.2.1 Fabrication of the Self-Supporting Porous V_2O_5 Scaffolds

The three-dimensional highly porous scaffolds with a well-defined microstructure were fabricated from V_2O_5 nanofibers as building blocks. Such nanofibers are obtained by a sol–gel process via an anisotropic polycondensation reaction.[19] They are composed of a bilayer separated by water molecules (with distance *d* of ∼1 nm) and are decorated with functional surface groups (Figure 1a), i.e., hydroxyl and oxo groups. The size and structure of the V_2O_5 nanofibers, i.e., the distance between the bilayers and the number of surface functional groups, can be adjusted via processing parameters.[19] In this work, nanofibers with a length of up to 6 μm, a width of 10–20 nm, and 1.5 nm in height were used. Owing to their high aspect ratio and architecture, the V_2O_5 nanofibers exhibit mechanical flexibility.[39] Combined with the available surface functional groups, their assembly from an aqueous dispersion by an ice-templating method is feasible.[35] The method involves instant freezing of the nanofiber dispersion in liquid nitrogen, leading to fast ice crystals growth and assembly of the V_2O_5 nanofibers. The latter is based on the interaction of the surface functional groups with the growing ice crystals and the nanofiber's flexibility. In this manner, the nanofibers are guided and subsequently trapped by the ice crystals that are removed by freeze-drying. The macroscopic form and size of the yielded V_2O_5 scaffolds depend on the mold's geometry. Moreover, the ice crystal profile and size define the pore morphology of the scaffolds, which can be precisely controlled by the direction and extent of the temperature gradient.

On the basis of this method, we fabricated highly porous V_2O_5 scaffolds with an adjusted structure of aligned open channels in the direction parallel to the charge transport. Thereby, the unidirectional temperature gradient of 18.75 K mm^{-1} in the *z*-direction was employed to ensure the defined ice crystal growth orientation within the aqueous dispersion, resulting in aligned elongated pores and continuous channels. Figure 1b shows a schematic depiction of the setup and the process of nanofiber trapping and arrangement into an ordered architecture by the formed ice crystals. The latter is characterized by two microstructural features, lamellas and pillars,[35] as displayed in Figure 1c. The organization of the nanofibers into a hierarchical architecture is based on hydrogen bonds, mediated by the water molecules and the functional surface groups.[35] To this end, self-supporting scaffolds were fabricated with a cylindrical form (Figure S1, Supporting Information) appropriate for mechanical and

electrochemical investigations (Figure 1d). The visible color stripes along the *z*-direction of the scaffold indicate the presence of lamella alignment.

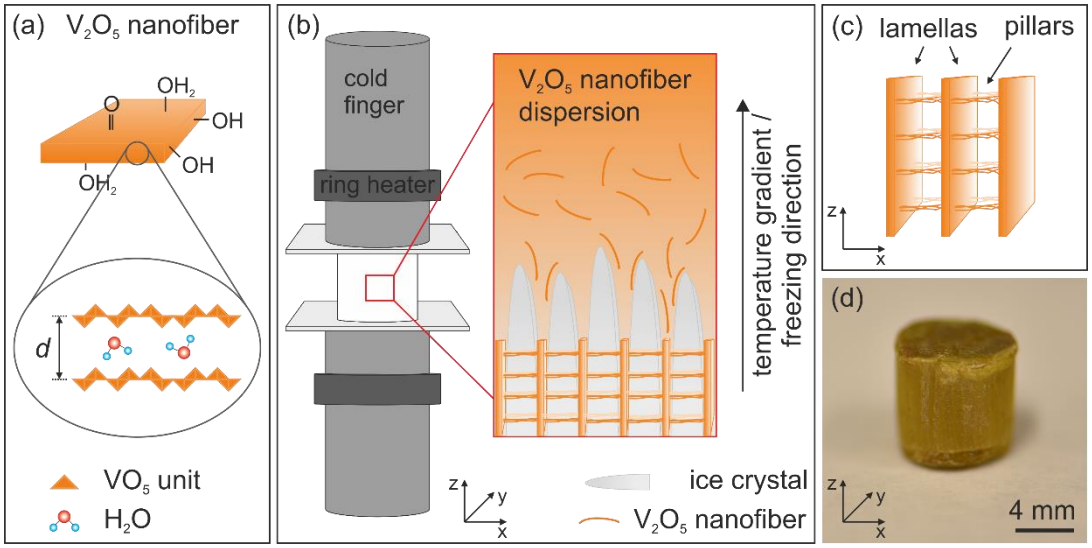

Figure 1. Vanadium pentoxide (V_2O_5) nanofibers and their assembly into highly porous scaffolds. (a) Scheme of a V_2O_5 nanofiber with functional groups on its surface. It is composed of a chain-like VO_5 unit structure separated by water molecules with the interlayer distance *d*. (b) Setup used for the fabrication of the V_2O_5 scaffolds showing the two Cu cold fingers equipped with ring heaters that control the temperature. In addition, the arrangement and trapping of the nanofibers between the ice crystals propagating along the temperature gradient are illustrated. (c) Schematic depiction of the scaffold's structure, including lamellas and interconnecting pillars, along the longitudinal direction. (d) Digital image of the V_2O_5 scaffold after freeze-drying.

The hierarchical arrangement of the nanofibers into porous scaffolds was confirmed by the scanning electron microscope (SEM) review, shown in Figure 2. The cross-section positions of the presented microstructures, representative for the whole scaffold, are indicated in the schematic illustration. Highly ordered lamella alignment is visible across the longitudinal direction (Figure 2a), while the transverse section provides insights into the pore morphology made of lamella interconnections via pillars (Figure 2c). Furthermore, a domain-like structure over several hundreds of micrometers is visible (Figure 2b). The different *x*–*y* orientations of such domains are attributed to the various nucleation sites of the formed ice crystals, which further propagate along the temperature gradient. Moreover, due to the spatial constraint the formed ice crystals of different in-plane orientation fuse together, yielding connected

domains in the microstructure (Figure 2d). A closer look of such domains reveals a filigree structure comprised of interwoven nanofibers arranged in stacked lamellas with a regular distance of ~20 µm that correlates to the pore size of the scaffolds (Figure 2e).

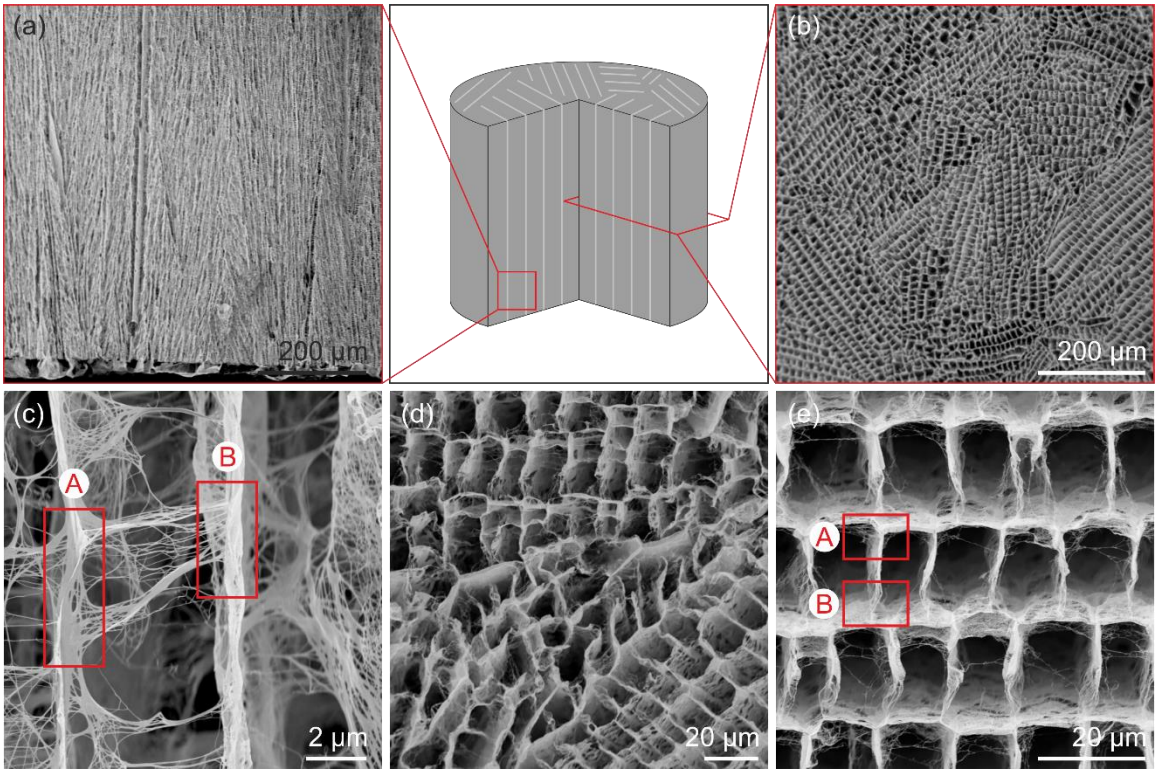

Figure 2. SEM investigation of the V_2O_5 scaffolds' microstructure at different cross-sections (positions are indicated in the schematic illustration). (a, c) Longitudinal and (b, d, e) transverse cross-section images revealing lamella orientation along the z-direction, as well as regularly stacked lamellas interconnected by pillars comprised of nanofiber bundles, respectively. The regions of strongly connected pillars to the lamellas are indicated by A, whereas those weakly connected, by B.

In general, the microstructure comprises thin mesoporous lamellas, which thickness is adjusted by the dispersion concentration. Moreover, regularly distributed pillars comprised of nanofiber bundles interconnect the lamellas. The SEM images presented in Figure 2c,e show that pillars have a thickness gradient, which affects their mesoporosity and their interconnection to the lamellas. The latter is different on the top and bottom for one lamella (positions A and B, respectively, Figure 2c,e). This is due to the mechanism of the lamella and pillars formation.[35] Apparently, the thinner part of the pillars is weakly connected to the lamella by several individual nanofibers, while

the thicker part is strongly connected by densely arranged nanofibers (see details in Figure S2, Supporting Information). The micrometer pores in the form of cavities as well as the mesoporosity (~5 nm) of the lamellas and pillars are attributed to the exceptionally high porosity of 99.9% (Figure S3, Supporting Information). Furthermore, analysis of the scaffolds by the Brunauer–Emmett–Teller (BET) method revealed a high specific surface area of 211 m^2 g^{-1}. This value is comparable with that of porous carbon-nanotube-based electrodes that provide a large number of intercalation sites per area and short diffusion paths for the charge carriers.[38]

Furthermore, the electrochemical reactions during the ion intercalation process into V_2O_5 nanofibers are affected by the water molecules present between the bilayers of the nanofibers and their entire network.[40] In this respect, the molecules keep a bilayer distance large enough for ion intercalation and shield the charge of the ions. The latter enables a faster ion shuttling into the host lattice as it was reported for the co-intercalation of water molecules and Mg^{2+} into V_2O_5.[40] Therefore, it was important to determine the water content of the scaffolds as we assume a similar shuttling process for Al^{3+}. Thermal gravimetric analysis (TGA) revealed 13.81 wt % H_2O in the scaffolds, which correlates to a hydration state *n* of 1.5 in $V_2O_5 \cdot n\ H_2O$ (Figure S4, Supporting Information). Furthermore, the X-ray diffraction (XRD) pattern of the scaffold revealed the typical reflection peak for bilayered V_2O_5 structures at $2\theta = 8.2°$ (Figure S5, Supporting Information). It corresponds to the distance between the bilayers, thus referring to the number of water molecules between them.[19] To this end, we determined that the interlayer distance of the V_2O_5 bilayer is 1.07 nm, which corresponds to 1.4 molecules of the hydrogen-bonded water[19,41] and correlates well with the TGA results. This spacing assures the ability of the nanofibers to host ions, in our case Al^{3+}, while the water content can effectively shield the electrostatic interactions of Al^{3+} cations, thus resulting in good electrochemical kinetics and stability.

4.2.2 Mechanical Properties of V_2O_5 Scaffolds

Besides the microstructural investigations, static compression tests up to a maximum compression of 90% were conducted to monitor the mechanical properties of the scaffolds parallel to the lamella orientation. Figure 3a shows a typical compressive stress–strain curve for the V_2O_5 scaffolds. The curve reveals a linear regime up to 6% followed by a slight increase in stress up to 45% compression and reaches its maximum before entering the densification regime above 50%. Further compression

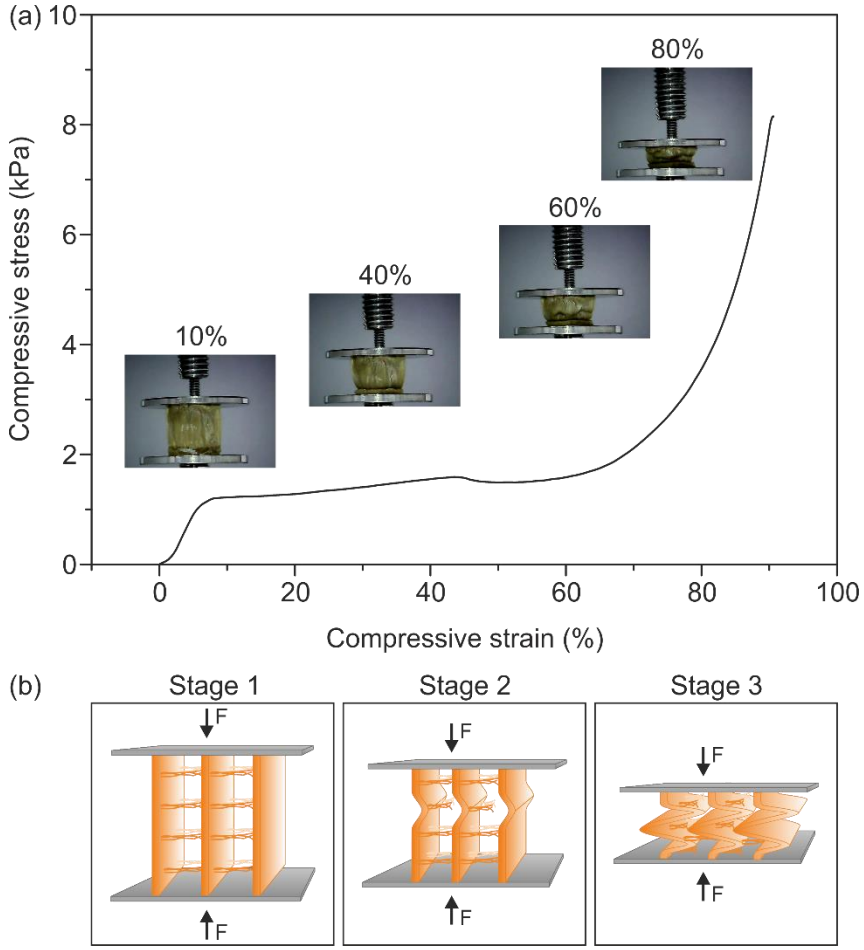

Figure 3. Mechanical performance of the V_2O_5 scaffolds under compression. (a) Compressive stress–strain curve with corresponding in situ images of the different compression states. (b) Schematic illustration of the scaffold's deformation mechanisms. Stage 1 comprises the linear elastic behavior, followed by stage 2 characterized by the pillar pull-out and lamella buckling. Further pillar pull-out and stronger lamella buckling take place in stage 3, causing the scaffold densification.

results in an increase in stress, attributed to the densification of the entire scaffold.[42] To monitor the macroscopic scaffold's deformation mechanisms under compression stress, we recorded different stages of the test (Video S1, Supporting Information). The digital images corresponding to the compression states are included in Figure 3a. We observed that the scaffolds homogeneously deform with preserving the lateral dimension, underlining the importance of the aligned lamellas for the entire scaffold stability. On the basis of the compressive stress–strain curves, the Young's modulus and strength were determined to be 24.97 ± 3.00 kPa and 1.30 ± 0.18 kPa, respectively.

The Young's modulus is significantly higher (133%) than that of the V_2O_5 scaffolds with completely different lamella alignment (centrosymmetric orientation).[35] The difference in the mechanical properties can be attributed to the various lamella orientations toward the scaffold's center as both types of scaffolds exhibit similar porosity. In the case of the centrosymmetric scaffolds the properties are averaged over all orientations. This supports the conclusion that the lamellas are the main load bearer of the scaffolds, and hence, their orientation to the applied load is of great importance. Furthermore, the mechanical performance depends on the lamella thickness, the micro-/mesoporosity, and finally their interconnections via the pillars. All of these aspects contribute to the effective stress distribution, supported by the entire hydrogen-bonded network of the V_2O_5 nanofibers within the lamellas. Accordingly, we assume three possible deformation mechanisms governing the densification of the scaffolds structure in three compression dependent stages, as schematically depicted in Figure 3b. Up to 6% compression, the effective stress distribution via pillars and the energy dissipation via reversible lamella bending are the main deformation appearances of the scaffold's linear elastic behavior. Further increase of the stress (up to 45% compression) causes the stronger bending of the lamellas. Consequently, the lamella buckling takes place due to the pronounced pull-out of the pillars and hence their disjunction. Most likely, the pull-out takes place at the weakly bonded part of the pillars with lamellas (Figure 2 and Figure S2, Supporting Information). Compression above 45% leads to the plastic deformation characterized by the stronger lamella buckling and the densification of the scaffolds. The lamella buckling is possible due to their intrinsic mechanical flexibility based on the high aspect ratio of the nanofibers and their hydrogen-bonded network. In our previous work, we monitored this phenomenon in situ by an SEM equipped with two micromanipulators; it revealed bending of the lamellas under high angle without breaking.[43]

4.2.3 Creasing and Electrical Properties of V_2O_5 Scaffolds

Creasing of the scaffolds requires defined microstructural features, which allow flexibility of the lamellas without their damage. The latter is important to support a facilitated disjunction from each other and their folding within the scaffolds. In this respect, the flexibility of the lamellas is adjusted by their thickness, while the lamella distance and pore morphology are controlled by the temperature gradient. In this work, scaffolds with a lamella thickness of ~50 nm and their distance of ~20 μm were

obtained by the adjusted temperature gradient and concentration of the V_2O_5 aqueous dispersion (see Experimental Section). Therefore, the obtained lamella structure is optimized through the mesoporosity (~5 nm pore size) and the interconnections with the pillars, which enable the effective creasing of the scaffolds.

The compression of cylindrical scaffolds up to 90% yielded a disc-shaped form without visible damage while only changing their lateral dimensions (Figure 4a), leading to a tap density of ~28 mg cm^{-3}. Further SEM investigations (Figure 4) of the compressed scaffold's surface and cross-section revealed the expected creased lamellas arrangement and that the surface porosity is preserved. The latter is a combination of micro- and mesoporosity. Specifically, the microporosity dominates over the complete surface, visible as interlamella cavities of reduced pore size within different domains (Figure 4b). In addition, the cavities are partially covered by a mesoporous net of interwoven nanofibers (Figure 4c). The longitudinal cross-section reveals densely packed buckled lamellas, which are creased in the vertical direction along their alignment. Likewise, the reduced lamella distance and number of pillar connections are visible (Figure 4d). A closer inspection of the microstructure revealed the integrity of the mesoporous lamellas with the corrugated surface structures composed of nanofibers. In addition, the pulled pillars and separated nanofibers are visible. It is important to note that the lamellas are not broken despite their high degree of bending, forming a looplike structure (Figure 4e,f). The loops are involved in the creation of contact points among the lamellas where they support each other and provide the creased scaffolds with the mechanical stability. In addition, the domain-like structure constrains the movement of the lamellas, preventing their shearing and delamination.

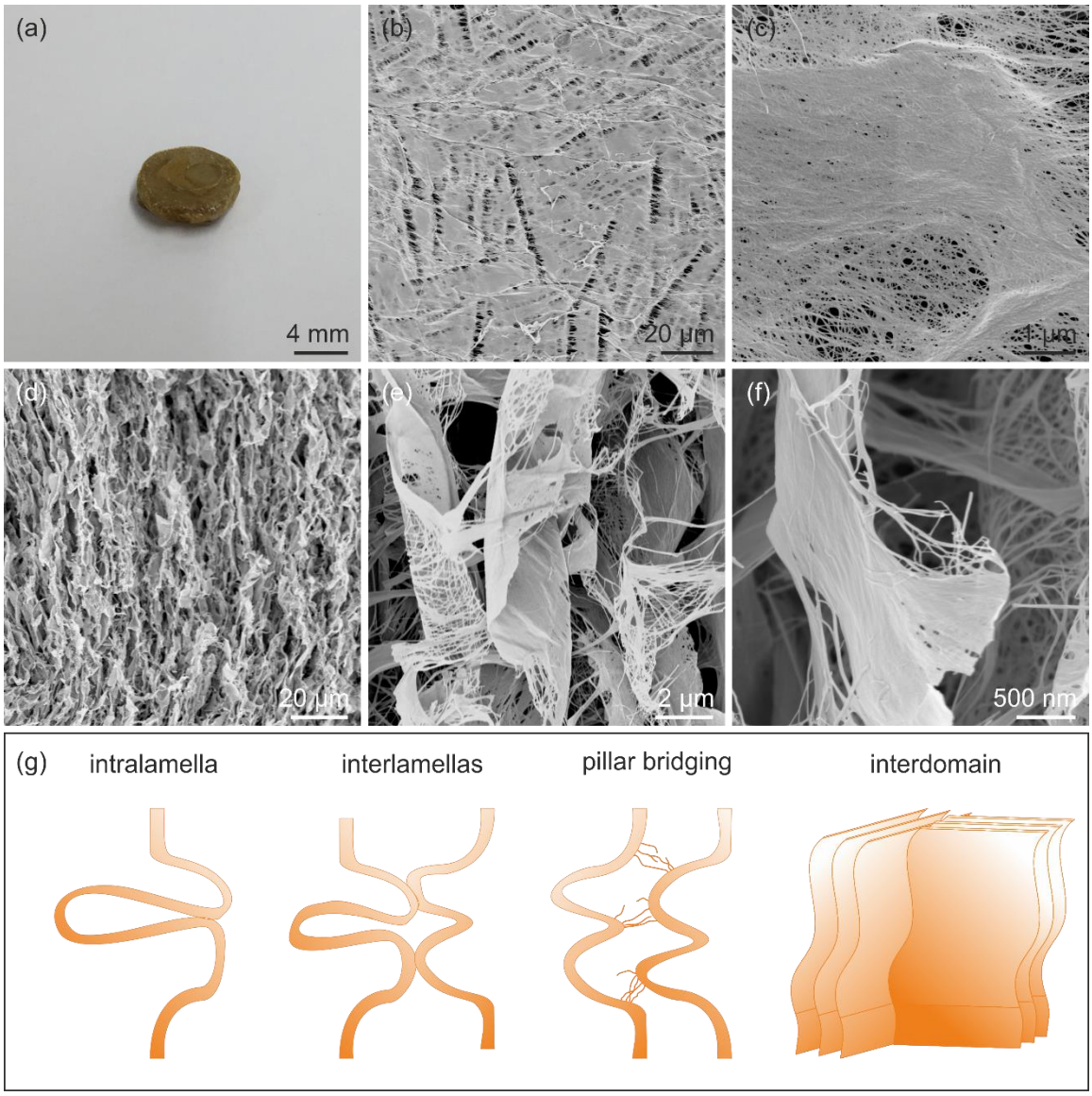

Figure 4. (a) Digital image of creased scaffold, revealing its disc-like shape. (b, c) SEM images of the creased scaffold's surface with the micro- and mesoporosity. (d–f) Longitudinal cross-section SEM images of the corrugated lamella structure and the lamella contact points. (g) Schematic illustration of the created contact points, including intra- and interlamella connection, pillar bridging between lamellas, and interdomain connections.

In general, the electrical conductivity of the sol–gel derived V_2O_5 nanofibers-based materials depends on several factors, including the water content and the ratio of V^{4+} to V^{5+}.[19] The latter strongly influences the electronic contribution to the overall electrical conductivity through the electron hopping along the V^{4+} and V^{5+} centers within the nanofibers. As for the water content and thus the hydration state of the nanofibers, it influences the proton diffusion along the hydrogen-bond network of the nanofibers.[31]

This ionic conductivity contributes only when the hydration state *n* is larger than 0.5.[19] Since the hydration state of our scaffolds is 1.5, the electrical conductivity of the scaffolds is a combination of the ionic and electronic conductivities. Both benefit from the well-interconnected structure. In this respect, we investigated the electrical properties of the scaffolds by electrochemical impedance spectroscopy (EIS). A two-point configuration, parallel to the lamella orientation, was employed at different compression states of the scaffolds ranging from 0% to 75% (Figure S6, Supporting Information). From the fitted EIS data the internal resistance and, hence, the electrical conductivity of the scaffolds were determined. A decrease of the scaffolds' internal resistance with increasing compression state is concluded from the Nyquist plot (Figure 5a). In order to determine the electrical conductivity as a function of compression state, the simultaneous decrease of the distance between the Cu electrodes and the porosity of the scaffolds were taken into consideration (see details in the Supporting Information). The determined electrical conductivity of the scaffolds increases with the compression state (Figure 5b) and follows the scaffold's compressive deformation and densification (Figure 3a). In particular, up to 40% compression the electrical conductivity slightly increases, which reflects the linear elastic and the plateau regime of the compressive stress–strain curve where the scaffold's lamellar structure is preserved. The more pronounced increase in electrical conductivity starts at compression state beyond 40%. This phenomenon is attributed to the previously discussed structural change caused by the creasing mechanism and the densification of the scaffold. It includes the creation of new contact points of the lamella loops, pillar bridging, and contacts between the domains as schematically illustrated in Figure 4g. Therefore, a faster and more effective charge transport is facilitated by the shortened paths. To this end, the scaffolds have a good intrinsic electrical conductivity of 0.42 mS cm^{-1} at 75% compression. The determined electrical conductivity of the V_2O_5 scaffolds is comparable to 10^{-2}–10^{-4} S cm^{-1} for V_2O_5 single crystals and $\sim 10^{-3}$–10^{-6} S cm^{-1} for vapor- and sputter-deposited,[44,45] and spray-coated V_2O_5 thin films.[46] The relatively low value of the electrical conductivity compared to the 2D V_2O_5 thin films[31] can be explained by the high porosity of the scaffolds.

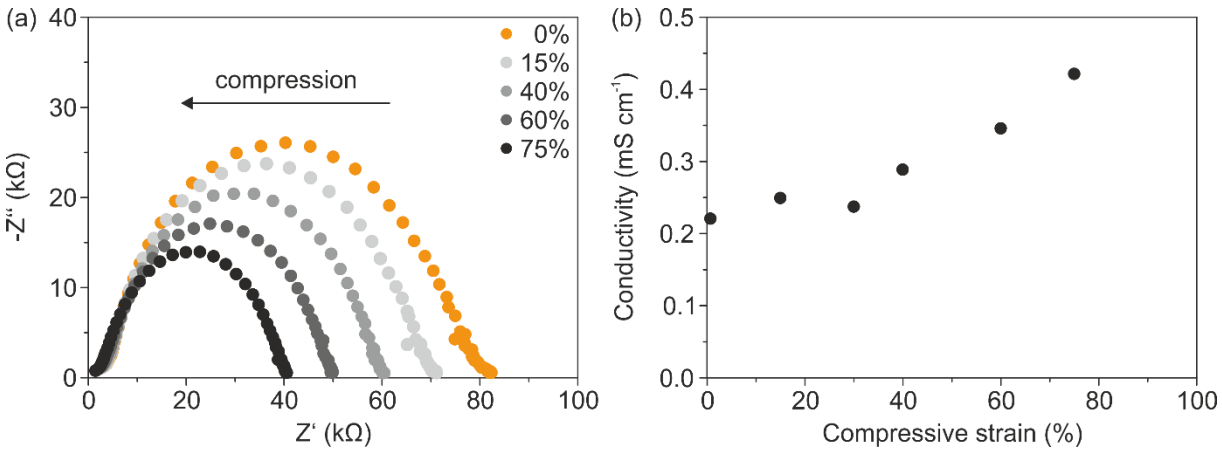

Figure 5. (a) Nyquist plot obtained in a two-point configuration as a function of the compression state of the V_2O_5 scaffolds. (b) Determined electrical conductivity at different compression states.

4.2.4 Electrochemical Characterization of Creased Scaffolds

We further characterized our creased V_2O_5 scaffolds (90% compression) as cathodes for AIB concerning their electrochemical properties. The high porosity of the creased scaffolds limits their tap density (~28 mg cm^{-3}) but facilitates a large electrode/electrolyte interface, rendering them for practical application in half-cell configurations. For this purpose, the testing cell included the creased V_2O_5 scaffolds in the shape of a disc (Figure 4a), aluminum foil as the counter electrode, and glass fiber membranes as separators soaked with the ionic liquid-based electrolyte. Molybdenum was used as a current collector for the cathode and anode sides due to its high stability in the applied potential window (Figure S7, Supporting Information). The used electrolyte is 1-ethyl-3-methylimidazolium chloride ([EMIM]Cl) mixed with aluminum chloride ($AlCl_3$) in the ratio of 1:1.5. This ratio assures the necessary acidity and guarantees the presence of chloroaluminate complexes, especially $Al_2Cl_7^-$ and $AlCl_4^-$, essential for the de/intercalation of Al^{3+}.[47]

Furthermore, it was shown, that Cu or Ag doping of V_2O_5 xerogels significantly enhances their electrical conductivity, facilitates the metal-ion intercalation, and enables the fast lithium insertion rates.[46,48] Recently, we reported about a one-step Cu-doping approach for 2D V_2O_5 paper-like thin films.[32] This in situ method is based on the Cu dissolution and migration into the cathode, i.e., its doping during electrochemical testing. The doping process is enabled because bilayered V_2O_5 offers two different insertion sites.[49] In particular, one site is near the planar oxygen atom and the other close to the apical oxygen atom of the VO_5 units. The latter is typically

occupied by dopants;[50] thus, the other insertion site is available for ion intercalation. In this work, we used a Cu foil as a doping source to obtain a Cu-doped V_2O_5 cathode. The foil was placed beneath the scaffolds, providing a continuous flow of Cu that can migrate into the cathode. In this way, the intrinsic electrical conductivity of our creased V_2O_5 scaffolds was further enhanced.

In order to ensure the availability of Cu for the migration and doping process, the anodic cutoff potential had to be set around the potential for Cu dissolution. For our setup, using Cu as a bare cathode, this potential is around 1.1 V (Figure S8, Supporting Information). Furthermore, the capacity contribution of Cu dissolution is negligible, as shown in our previous work, assuring that the capacity obtained is only attributed to the Al^{3+} de/intercalation.[32] Therefore, we set the upper cutoff potential for the electrochemical tests to 1.1 V. Galvanostatic charge/discharge tests were performed to determine the specific storage capacity and cycling stability of the scaffolds. The results revealed that the scaffolds' discharge capacities of up to 58, 85, and 105 mAh g^{-1} with Coulomb efficiencies of 99, 92, and 81% at the current densities 2000, 1000, and 500 mA g^{-1} are achieved. In Figure 6a the specific discharge capacity at these current densities is presented. In general, the discharge capacities first show an increase, up to the capacity maximum, which is then followed by capacity fading. The increase of the discharge capacity can be explained by the ongoing Cu migration process, which enhances the electrical conductivity and, thus, the electrochemical performance of the scaffolds. Therefore, when the Cu migration process reaches its saturation, the maximum increase of the electrical conductivity is reached and, consequently, the maximum capacity as well. The rate of the capacity increase is higher for lower current densities, as the system has more time during each cycle for the Cu migration.

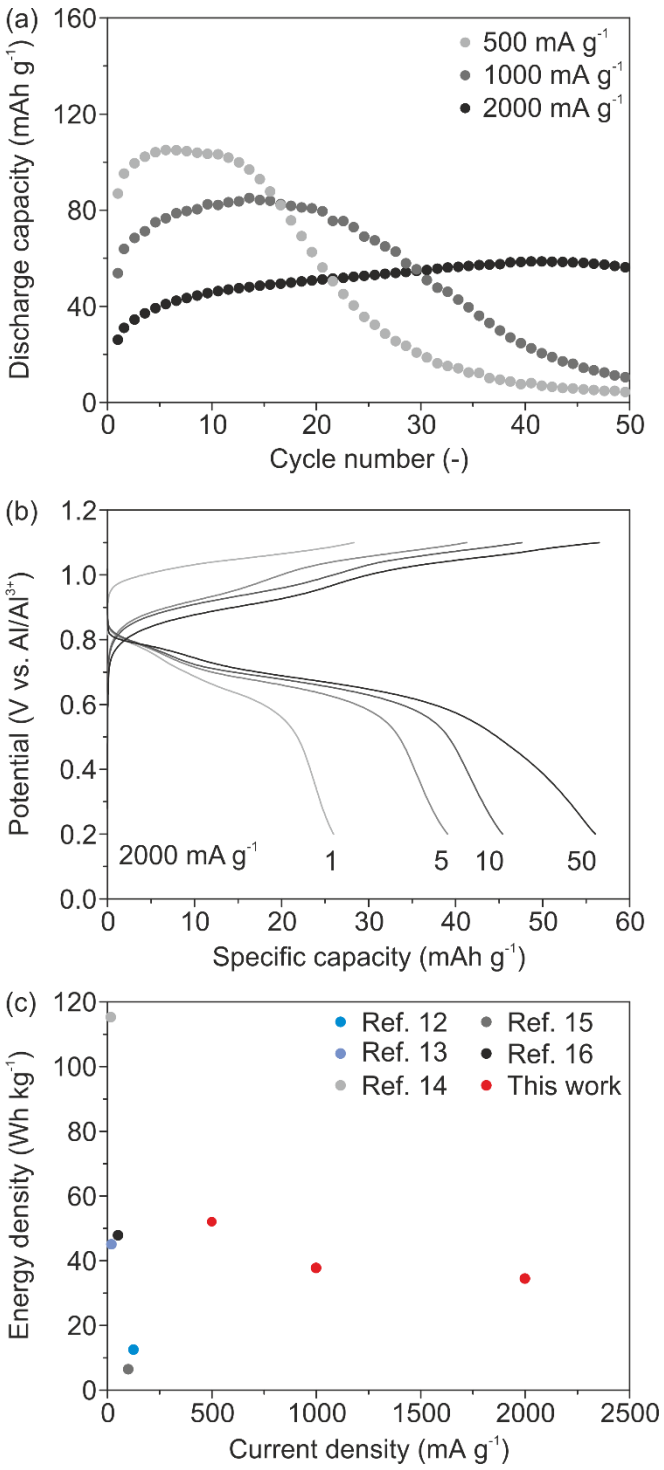

Figure 6. Electrochemical performance of the creased scaffolds. (a) Specific discharge capacity retention for current densities of 500, 1000, and 2000 mA g^{-1}. (b) Potential capacity profiles for cycles 1, 5, 10, and 50 at a current density of 2000 mA g^{-1}. (c) Energy density vs current density for the V_2O_5 scaffolds compared to reported V_2O_5-based electrodes (data from refs [12-16] and this work).

The capacity profiles for the current density of 2000 mA g^{-1} (Figure 6b) confirm the increase of the specific discharge capacities with cycling. The profile further reveals the reversible de/intercalation of Al^{3+} with a Coulomb efficiency of almost 100% (see also Figure S9, Supporting Information). In addition, two distinct intercalation potentials are visible at 0.67 and 0.79 V, which coincide with already reported values for crystalline V_2O_5-based[11,14,16] and for amorphous V_2O_5 electrodes for AIBs.[13] The presence of the two intercalation potentials, as well as the two available intercalation sites for V_2O_5,[49] is expected as our scaffolds are comprised of crystalline V_2O_5 nanofibers arranged in an amorphous microstructure.

To validate the benefits of the structure of our V_2O_5 creased scaffolds for the electrochemical performance, we compared their energy densities to those reported for V_2O_5-based cathodes. The reported works include a binder-free V_2O_5 cathode on a Ni support,[16] an amorphous V_2O_5/C composite mixed with poly(tetrafluoroethylene) (PTFE),[13] crystalline V_2O_5 nanowires with poly(vinylidene difluoride) (PVDF), and carbon black,[12] crystalline V_2O_5 nanowires with PVDF and carbon black,[14] as well as V_2O_5 nanoflakes grown on stainless steel.[15] The energy densities of 35, 38, and 52 Wh kg^{-1} at current densities of 2000, 1000, and 500 mA g^{-1} were determined for the V_2O_5 scaffolds. The comparison reveals that our cathodes deliver comparable or even superior energy densities, but at much higher current densities, as shown in Figure 6c. This is attributed to the scaffold's highly porous and creased structure, including its high specific surface area and increased amount of short diffusion pathways for the electrolyte. Furthermore, by the use of our binder-free V_2O_5 scaffold, undesirable side reactions between the ionic liquid-based electrolyte and the binder are avoided. Additionally, the choice of Mo as current collector and a suitable potential window omitting side reactions contribute to superior electrochemical performance.

The advantages of the highly porous and creased V_2O_5 scaffolds are emphasized when their electrochemical performance is compared to that of the 2D paper-like V_2O_5 thin films (Table S1, Supporting Information).[32] For the same current density of 500 mA g^{-1} superior areal capacity and energy density were achieved for the 3D V_2O_5 creased scaffolds, reaching 0.24 mAh cm^{-2} and 52 Wh kg^{-1}, respectively, in comparison to 1.4×10^{-3} mAh cm^{-2} and 2 Wh kg^{-1} for the 2D thin films. Thereby, an increase of 2 orders of magnitude in the areal capacity and more impressively 25-fold enhancement of the energy density are achieved by targeted tailoring of the electrode material. Therefore, the gained high specific surface area of the 3D structure enables

a larger electrode/electrolyte interface, more efficient ion diffusion pathways, available intercalation sites, and thus support of the intercalation kinetics.

Notably, comparison of our V_2O_5 scaffolds vs carbon-based materials, on the basis of the common test at high current densities, reveals a similar energy density.[8,47,51-53] In particular, an energy densitiy of 170 Wh kg^{-1} was reached for mesoporous reduced graphene oxide,[8] 40 Wh kg^{-1} for graphite-based battery,[47] ~43 Wh kg^{-1} for an edge-rich graphene paper,[51] and 30 Wh kg^{-1} for carbon nanoscrolls.[52] However, the carbon-based materials have a limited storage capacity due to the one-electron transfer of the intercalated $AlCl_4^-$.[54,55] Thus, our structurally designed V_2O_5 scaffolds, which are able to host Al^{3+}, deliver high specific storage capacities, resulting in high energy densities, and, therefore, outperform not just V_2O_5-based but also carbon-based cathodes.

4.3 Conclusions

We demonstrated the fabrication of anisotropic highly porous scaffolds (99.9% porosity) comprised of V_2O_5 nanofibers by unidirectional ice-templating. This structural design of ordered lamellas and pillars enables the creasing of the scaffolds to create a folded lamella structure without visible damage while preserving a high porosity. Notably, the creased structure enhances the electrical conductivity by the simultaneous processes of lamellas' buckling and their contacts formation leading to a facilitated charge transport. The electrochemical investigation of the creased scaffolds, as the cathode for AIB, revealed that high capacities up to 105 mAh g^{-1} at a current density of 500 mA g^{-1} with a corresponding energy density of 52 Wh kg^{-1} can be achieved. Thereby, the 3D creased scaffolds deliver a superior areal capacity (2 orders of magnitude) and energy density (25-fold) compared to the 2D paper-like thin films. Thus, our scaffolds are comparable or even superior to other V_2O_5- and carbon-based electrodes for aluminum-ion batteries. However, it would be interesting to assess the effects of the scaffolds' height and the precise control of their creasing degree on their electrochemical performance.

4.4 Experimental Section

4.4.1 Synthesis of V_2O_5 Dispersion

The V_2O_5 nanofibers are fabricated by heating a mixture of ammonium meta-vanadate (1 g, Fluka) and an acidic ion-exchanger (10 g, Dowex 50WX8 50–100, Alfa Aesar) in deionized water (200 mL) for 10 min in an 80 °C oil bath under vigorous stirring. Subsequently, the dispersion was cooled to room temperature and aged for 42 days. After aging the V_2O_5 dispersion had a concentration of 3.55 mg/mL.

4.4.2 Fabrication of V_2O_5 Scaffolds

For the fabrication of V_2O_5 scaffolds by unidirectional ice-templating, a system custom-made by our group was used. The setup includes two parts, one of which is movable in the z-direction (Figure S1, Supporting Information). Both parts are comprised of a copper rod connected to a vessel filled with liquid nitrogen. Further, the copper cooling fingers were equipped with ring heaters to adjust the temperature. The lower part was set to −153 °C, whereas the upper part was set to −3 °C. A cylindrical poly(tetrafluoroethylene) (PTFE) mold with the same height and diameter of 8 mm was used. The precooled (4 °C) V2O5 dispersion (370 μL) was poured in the mold. To protect the copper rod from the V2O5 dispersion, a thin glass slide was used. After 3 min of freezing, the sample was stored in a climatic chamber (−25 °C, VC7018, Vötsch) for 3 min, followed by its demolding. For the microstructural characterization, the samples were cut in the frozen state. The frozen samples were freeze-dried in a freeze-dryer (L10E, Dieter Piatkowski). The freeze-drying program involves cooling of the chamber to −50 °C, followed by evacuating the chamber for 2 h. Subsequently, the temperature is stepwise increased to room temperature within 17 h.

4.4.3 Microstructural Characterization

The samples were sputtered (1 nm Ir, EM ACE600, Leica) and investigated by scanning electron microscope (Zeiss Ultra 55). Nitrogen adsorption–desorption isotherms were analyzed by a physisorption analyzer (Quantachrome Instruments Autosorb iQ3) after activation at 80 °C for 12 h. X-ray diffraction was performed by a PXRD (Rigaku Smartlab) in Bragg–Brentano geometry in the range of 5–30° with 0.01° as step size by using Cu Kα radiation, operated at an acceleration voltage of 40 kV and a current of 30 mA. TGA/DSC (STA 449C, Netzsch) measurements were done in synthetic air and with use of a constant heating rate of 2 K/min to 400 °C, at which the temperature was kept for 2 h.

4.4.4 Mechanical Characterization

Static compression test (UTM 150, Keysight) was used to determine the mechanical properties of the V_2O_5 scaffolds by compressing the scaffolds to 50% with a strain rate of 8.0 × 10–3 mm/s.

4.4.5 Electrical Characterization

The scaffolds were placed between two copper plates connected to an electrochemical test station (VSP300, Biologic). Electrochemical Impedance Spectroscopy (EIS) was performed in a frequency range of 0.1 Hz to 1 MHz with an amplitude of 10 mV. The obtained data were fitted and the internal resistance was used for the calculation of the electrical conductivity.

4.4.6 Electrochemical Characterization

Swagelok union connections made of PTFE and molybdenum contacts were used for the cells and were assembled in an argon filled glovebox (Labmaster SP, MBraun). The V_2O_5 scaffolds were sputtered from both sides with a thin gold layer (35 nm, SCD 040, Balzers Union) to reduce the contact resistance toward the molybdenum current collector. The source of Cu as a dopant for the V_2O_5 scaffolds was a 25 μm thick Cu foil (purity, 99.98%; Sigma-Aldrich) with a diameter one-third smaller than the diameter of the scaffolds. An 8 μm thick Al foil (purity, 99%; Sigma-Aldrich) was used as the anode and six layers of glass fiber membrane (Grade 934-AH, Whatman) as the separator. The electrolyte was composed of 1-ethyl-3-methylimidazolium chloride mixed with aluminum chloride in the ratio of 1:1.5 (IoLiTec Ionic Liquids Technologies). The cells were held for at least 2 h in open-circuit conditions. Galvanostatic charge/discharge tests were performed with the current densities of 500, 1000, and 2000 mA g^{-1} in the voltage range of 0.2–1.1 V. Cyclic voltammetry was carried out in the voltage window of 0.2–1.1 V with a sweep rate of 0.1 mV s^{-1}. The stability test for Mo current collectors in a Mo vs Mo configuration, separated by one glass fiber membrane, was performed in the voltage windows of 0.2–1.1 V and 0.02–2.5 V with sweep rates of 0.1 mV s^{-1} and 1 mV s^{-1}, respectively. The electrochemical performance of bare Cu as a cathode was carried out in a potential window of 0.02–2.5 V vs Al/Al^{3+} with 0.1 mV s^{-1} as the sweep rate. All electrochemical measurements were performed on an electrochemical test station (VSP300, Biologic).

4.5 Supporting Information

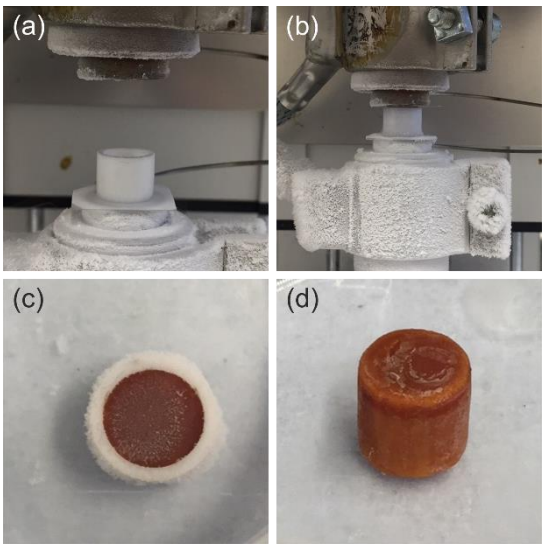

Figure S1: Illustration of the scaffold's fabrication process. (a) The cylindrical polytetrafluoroethylene (PTFE) 8 x 8 mm mold on the cold finger (120 K) (b) Mold filled with the V_2O_5 dispersion fixed by the upper cooling finger (270 K). (c) Top view of the frozen scaffold in the mold. (d) De-molded frozen scaffold.

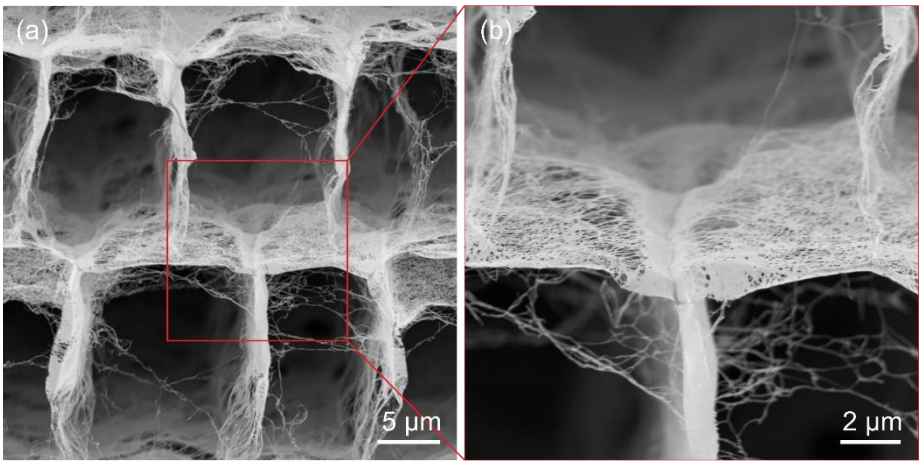

Figure S2: SEM images of the transversal cross-section of a V_2O_5 scaffold, revealing the mesoporosity of the lamellas.

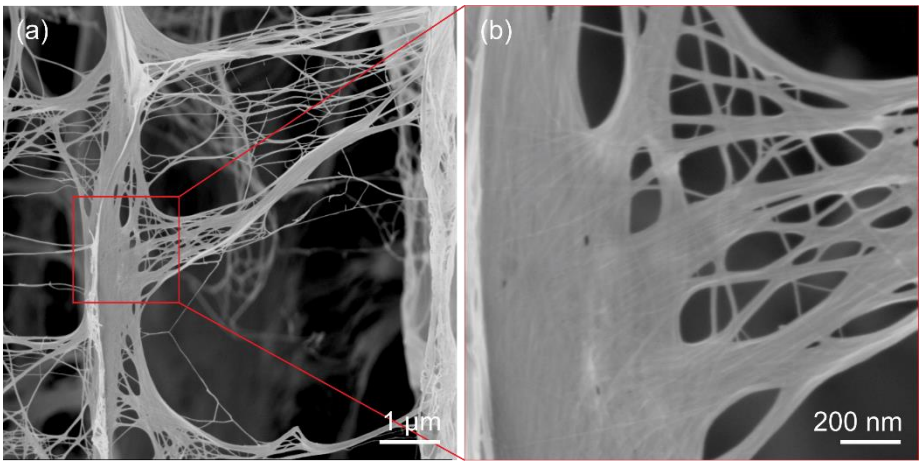

Figure S3: SEM images of the longitudinal cross-section of a V_2O_5 scaffold, revealing the mesoporosity of the lamellas, showing the filigree structure of the interconnecting pillars made of nanofibers.

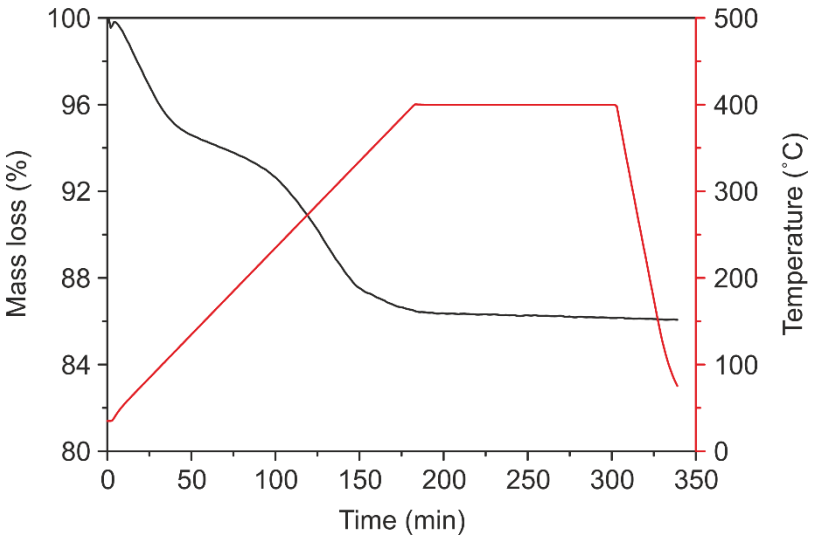

Figure S4: TGA plot for the scaffolds revealing 13.81 wt% mass loss corresponding to the residual H_2O.

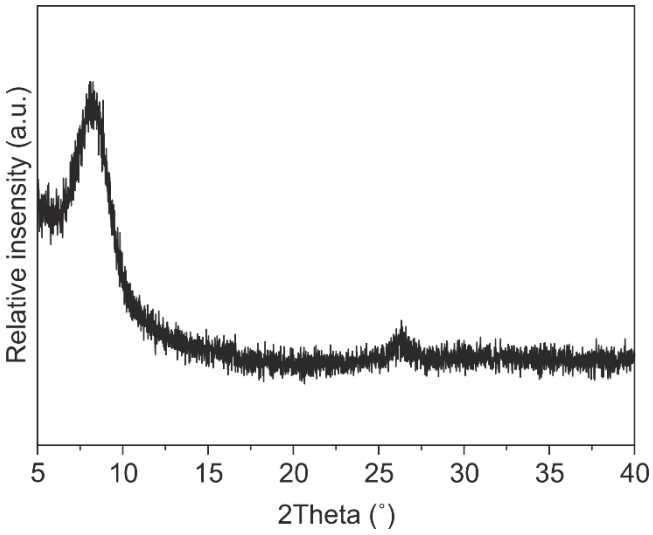

Figure S5: XRD pattern of a V_2O_5 scaffold.

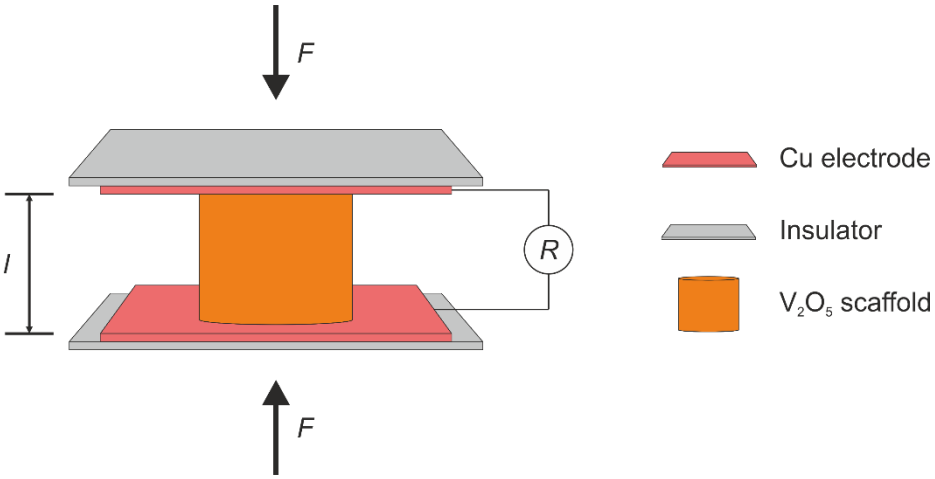

Figure S6: Schematic of the setup used for electrical conductivity measurements as a function of the compression state (applied load *F*, distance *l* and *R* internal resistance).

The electrical conductivity of the scaffolds:

The determination of the electrical conductivity is based on the obtained internal resistance of the EIS measurement, the scaffold's dimension and the compression state. In general, the electrical conductivity σ_0 can be calculated by

$$\sigma_0 = \frac{l}{R_{\text{internal}} \cdot A_{\text{scaffold}}} \quad (1)$$

with l as the distance between the electrodes, R_{internal} obtained resistance and $A_{\text{scaffolds}}$ the scaffold's area. Further, the porosity ε of the scaffolds is

$$\varepsilon = \frac{\rho}{\rho_{V_2O_5}} \quad (2)$$

with ρ as scaffold density and ρ_{V2O5} the density of V_2O_5. As the compression state influences d and ε, the following relationship for the relative conductivity of cylindrically shaped pores, aligned parallel to the electrical field is valid.[1,2]

$$\frac{\sigma}{\sigma_0} = 1 - \varepsilon \quad (3)$$

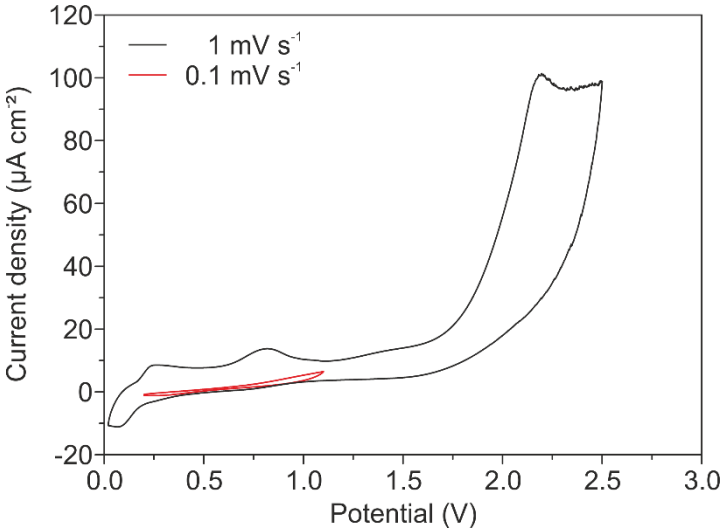

Figure S7: CV curves obtained from testing Mo vs. Mo configuration separated by a glass fiber membrane to determine a stable potential window. Black curve (1 mV/s) shows corrosion below 0.2 V and above 2 V. Therefore, the potential window 0.2 - 1.1 V with a sweep rate of 0.1 mV/s (red curve) was chosen for the electrochemical measurements.

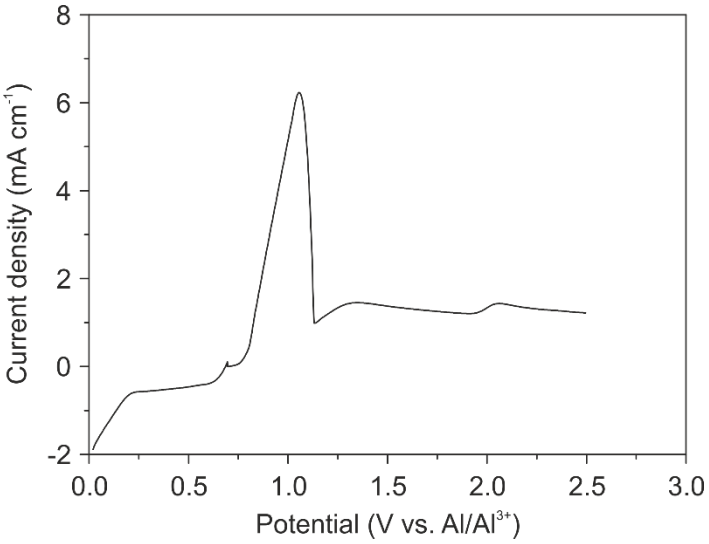

Figure S8: The linear sweep voltammetry curve for Cu as bare cathode revealing an anodic peak at ~1.1 V.

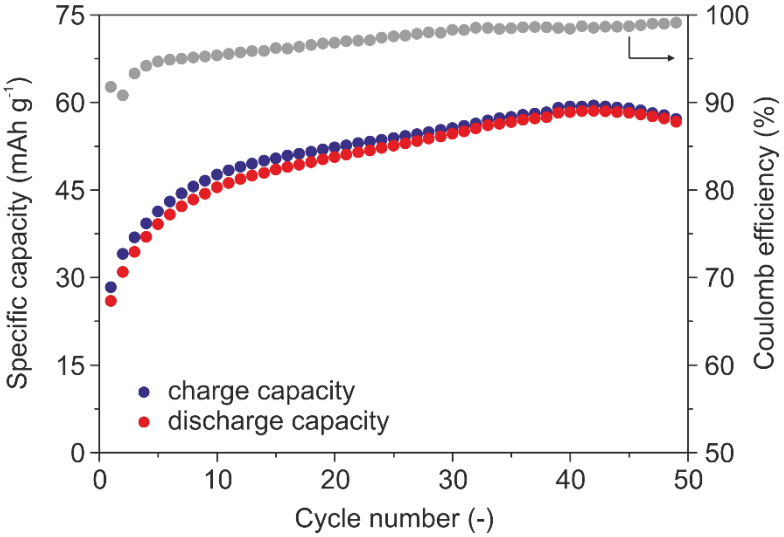

Figure S9: Galvanostatic charge/discharge curves for a creased scaffold with an applied current density of 2000 mA g^{-1}.

Table S1: Comparison of the electrochemical performance of the creased V_2O_5 scaffolds with the 2D V_2O_5 paper-like thin films

Electrode material	**Current density (mA g^{-1})**	**Specific capacity (mAh g^{-1})**	**Areal capacity (mAh cm^{-2})**	**Energy density (Wh kg^{-1})**
2D V_2O_5 paper-like thin film[3]	25	173	0.05	74
	500	5	0.0014	2
This work: 3D V_2O_5 creased scaffold	500	105	0.24	52
	1000	85	0.20	38
	2000	58	0.13	35

References

[1] H. J. Juretschke, R. Landauer, J. A. Swanson, *J. Appl. Phys.* **1956**, *27*, 838.

[2] J. Mizusaki, K. Waragai, S. Tsuchiya, H. Tagawa, Y. Arai, Y. Kuwayama, J. *Am. Ceram. Soc.* **1996**, *79*, 109.

[3] A. M. Diem, B. Fenk, J. Bill, Z. Burghard, *Nanomaterials* **2020**, *10*, 247.

4.6 Acknowledgments

We thank the group of J. Spatz from the Max Planck Institute in Stuttgart for equipment use and technical support, T. Wörner for engineering support, and A. Schilling for experimental assistance. We are thankful to S. Emmerling for performing the BET measurements. We also greatly appreciate L. Raafat for valuable discussions and proofreading the manuscript. The financial support provided by the Vector Stiftung (Project No. 0090018) is highly appreciated.

4.7 References

[1] V. Etacheri, R. Marom, R. Elazari, G. Salitra, D. Aurbach, *Energy Environ. Sci.* **2011**, *4*, 3243.

[2] J. B. Goodenough, Y. Kim, *Chem. Mater.* **2010**, *22*, 587.

[3] J. W. Choi, D. Aurbach, *Nat. Rev. Mater.* **2016**, *1*, 1.

[4] P. Canepa, G. Sai Gautam, D. C. Hannah, R. Malik, M. Liu, K. G. Gallagher, K. A. Persson, G. Ceder, *Chem. Rev.* **2017**, *117*, 4287.

[5] M. S. Whittingham, *Chem. Rev.* **2004**, *104*, 4271.

[6] A. S. Aricò, P. Bruce, B. Scrosati, J.-M. Tarascon, W. van Schalkwijk, *Nat. Mater.* **2005**, *4*, 366.

[7] M. Armand, J.-M. Tarascon, *Nature* **2008**, *451*, 652.

[8] J. Smajic, A. Alazmi, N. Batra, T. Palanisamy, D. H. Anjum, P. M. F. J. Costa, *Small* **2018**, *0*, 1803584.

[9] Q. Li, D. Chen, H. Tan, X. Zhang, X. Rui, Y. Yu, *J. Energy Chem.* **2020**, *40*, 15.

[10] A. Moretti, S. Passerini, *Adv. Energy Mater.* **2016**, *6*, 1600868.

[11] S. Gu, H. Wang, C. Wu, Y. Bai, H. Li, F. Wu, *Energy Storage Mater.* **2017**, *6*, 9.

[12] N. Jayaprakash, S. K. Das, L. A. Archer, *Chem. Commun.* **2011**, *47*, 12610.

[13] M. Chiku, H. Takeda, S. Matsumura, E. Higuchi, H. Inoue, *ACS Appl. Mater. Interfaces* **2015**, *7*, 24385.

[14] H. Wang, S. Gu, Y. Bai, S. Chen, N. Zhu, C. Wu, F. Wu, *J. Mater. Chem. A* **2015**, *3*, 22677.

[15] H. Wang, X. Bi, Y. Bai, C. Wu, S. Gu, S. Chen, F. Wu, K. Amine, J. Lu, *Adv. Energy Mater.* **2017**, *7*, 1602720.

[16] H. Wang, Y. Bai, S. Chen, X. Luo, C. Wu, F. Wu, J. Lu, K. Amine, *ACS Appl. Mater. Interfaces* **2015**, *7*, 80.

[17] L. D. Reed, E. Menke, *J. Electrochem. Soc.* **2013**, *160*, A915.

[18] H. Yang, H. Li, J. Li, Z. Sun, K. He, H.-M. Cheng, F. Li, *Angew. Chem. Int. Ed.* **2019**, *58*, 11978.

[19] J. Livage, *Chem. Mater.* **1991**, *3*, 578.

[20] V. Petkov, P. N. Trikalitis, E. S. Bozin, S. J. L. Billinge, T. Vogt, M. G. Kanatzidis, *J. Am. Chem. Soc.* **2002**, *124*, 10157.

[21] J. Yao, Y. Li, R. C. Massé, E. Uchaker, G. Cao, *Energy Storage Mater.* **2018**, *11*, 205.

[22] Y. Yue, H. Liang, *Adv. Energy Mater.* **2017**, *7*, 1602545.

[23] S. Tepavcevic, H. Xiong, V. R. Stamenkovic, X. Zuo, M. Balasubramanian, V. B. Prakapenka, C. S. Johnson, T. Rajh, *ACS Nano* **2012**, *6*, 530.

[24] W. Luo, J.-J. Gaumet, L. Mai, *MRS Commun.* **2017**, *7*, 152.

[25] M. Mao, T. Gao, S. Hou, C. Wang, *Chem. Soc. Rev.* **2018**, *47*, 8804.

[26] D. B. Le, S. Passerini, F. Coustier, J. Guo, T. Soderstrom, B. B. Owens, W. H. Smyrl, *Chem. Mater.* **1998**, *10*, 682.

[27] Y. Yang, Y. Tang, G. Fang, L. Shan, J. Guo, W. Zhang, C. Wang, L. Wang, J. Zhou, S. Liang, *Energy Environ. Sci.* **2018**, *11*, 3157.

[28] F. Liu, Z. Chen, G. Fang, Z. Wang, Y. Cai, B. Tang, J. Zhou, S. Liang, *Nano-Micro Lett.* **2019**, *11*, 25.

[29] G. A. Elia, K. Marquardt, K. Hoeppner, S. Fantini, R. Lin, E. Knipping, W. Peters, J.-F. Drillet, S. Passerini, R. Hahn, *Adv. Mater.* **2016**, *28*, 7564.

[30] A. Moretti, F. Maroni, I. Osada, F. Nobili, S. Passerini, *ChemElectroChem* **2015**, *2*, 529.

[31] A. M. Diem, A. Knöller, Z. Burghard, J. Bill, *Nanoscale* **2018**, *10*, 15736.

[32] A. M. Diem, B. Fenk, J. Bill, Z. Burghard, *Nanomaterials* **2020**, *10*, 247.

[33] S. Deville, *Adv. Eng. Mater.* **2008**, *10*, 155.

[34] S. Deville, *J. Mater. Res.* **2013**, *28*, 2202.

[35] A. Knöller, T. Runčevski, R. E. Dinnebier, J. Bill, Z. Burghard, *Sci. Rep.* **2017**, *7*, 42951.

[36] X. Yu, B. Wang, D. Gong, Z. Xu, B. Lu, *Adv. Mater.* **2017**, *29*, 1604118.

[37] B. Wang, J. Ryu, S. Choi, G. Song, D. Hong, C. Hwang, X. Chen, B. Wang, W. Li, H.-K. Song, S. Park, R. S. Ruoff, *ACS Nano* **2018**, *12*, 1739.

[38] J. Ryu, B. Park, J. Kang, D. Hong, S.-D. Kim, J.-K. Yoo, J. W. Yi, S. Park, Y. Oh, *ACS Nano* **2019**, *13*, 14357.

[39] A. Knöller, C. P. Lampa, F. von Cube, T. H. Zeng, D. C. Bell, M. S. Dresselhaus, Z. Burghard, J. Bill, *Sci. Rep.* **2017**, *7*, 40999.

[40] G. Sai Gautam, P. Canepa, W. D. Richards, R. Malik, G. Ceder, *Nano Lett.* **2016**, *16*, 2426.

[41] J. Livage, *Coord. Chem. Rev.* **1998**, *178–180*, 999.

[42] M. F. Ashby, R. F. M. Medalist, *Metall. Trans. A* **1983**, *14*, 1755.

[43] A. Knöller, S. Kilper, A. M. Diem, M. Widenmeyer, T. Runčevski, R. E. Dinnebier, J. Bill, Z. Burghard, *Nano Lett.* **2018**, *18*, 2519.

[44] J. Bullot, O. Gallais, M. Gauthier, J. Livage, *Appl. Phys. Lett.* **1980**, *36*, 986.

[45] T. Szörényi, K. Bali, I. Török, I. Hevesi, *Thin Solid Films* **1984**, *121*, 29.

[46] F. Coustier, J. Hill, B. B. Owens, S. Passerini, W. H. Smyrl, *J. Electrochem. Soc.* **1999**, *146*, 1355.

[47] M.-C. Lin, M. Gong, B. Lu, Y. Wu, D.-Y. Wang, M. Guan, M. Angell, C. Chen, J. Yang, B.-J. Hwang, H. Dai, *Nature* **2015**, *520*, 324.

[48] F. Coustier, G. Jarero, S. Passerini, W. H. Smyrl, *J. Power Sources* **1999**, *83*, 9.

[49] D. Imamura, M. Miyayama, *Solid State Ion.* **2003**, *161*, 173.

[50] M. Giorgetti, M. Berrettoni, W. H. Smyrl, *Chem. Mater.* **2007**, *19*, 5991.

[51] Q. Zhang, L. Wang, J. Wang, C. Xing, J. Ge, L. Fan, Z. Liu, X. Lu, M. Wu, X. Yu, H. Zhang, B. Lu, *Energy Storage Mater.* **2018**, *15*, 361.

[52] Z. Liu, J. Wang, H. Ding, S. Chen, X. Yu, B. Lu, *ACS Nano* **2018**, *12*, 8456.

[53] Z. Liu, J. Wang, X. Jia, W. Li, Q. Zhang, L. Fan, H. Ding, H. Yang, X. Yu, X. Li, B. Lu, *ACS Nano* **2019**, *13*, 10631.

[54] Z. A. Zafar, S. Imtiaz, R. Razaq, S. Ji, T. Huang, Z. Zhang, Y. Huang, J. A. Anderson, *J. Mater. Chem. A* **2017**, *5*, 5646.

[55] Y. Zhang, S. Liu, Y. Ji, J. Ma, H. Yu, *Adv. Mater.* **2018**, *30*, 1706310.

5 Summary

The hierarchical design, inspired by natural role models of advanced electrodes using V_2O_5 Nanofibers as building blocks for mono- and multivalent metal-ion battery application was demonstrated. The role models were the dense and layered microstructure of nacre comprised of aragonite platelets embedded in an organic matrix and highly porous cuttlebone with its regular arranged lamellas and pillars made of aragonite fibers and a small organic fraction. Mimicking those two microstructures required a suitable material. In conclusion, flexible V_2O_5 nanofibers decorated with functional surface groups can be synthesized by a sol-gel route, which allows to control the nanofiber length by the growth time. Such nanofibers were successfully assembled into two mechanical stable, self-supporting and electrically conductive microstructures, *i.e.* paper-like thin films and highly porous scaffolds.

The paper-like thin films were obtained by a facile self-assembly process leading to micrometer thick thin films, comprised of a hierarchical arrangement of slabs and lamellas with incorporated water molecules. This hydrogen bond-based network exhibits remarkable mechanical properties, which are improved with the nanofiber length, as stress distribution is more effective. A humidity controlled post-treatment tuned the hydrogen bond network resulting in an enhancement of the mechanical properties. Additionally, an electrical conductivity of up to 2 S cm^{-1} was determined and could be related to an electronic and ionic contribution to the overall transport mechanism. It was observed that by aging the paper-like thin films a partial reduction V^{5+} to V^{4+} occurs, enhancing the electronic contribution to the electrical conductivity. Furthermore, reversible Li^+ intercalation into the paper-like thin films could be demonstrated, achieving a storage capacity of 150 mAh g^{-1} at a current density of 100 mA g^{-1}.

In addition, such binder-free and self-supporting paper-like thin films were employed as cathode material in aluminum-ion batteries. In this respect, a self-limiting Cu doping approach was established, which takes advantage of the Cu dissolution by the ionic liquid-based electrolyte and the presence of two different intercalation sites of the bilayered V_2O_5 nanofibers. This doping method resulted in the formation of a Cu-doped V_2O_5 bronze with Cu-enriched precipitates and thus significantly increased the electrical conductivity of the cathode. By this, the electrochemical performance of the cathode could be enhanced leading to the reversible intercalation of Al^{3+}. A specific

discharge capacity of 170 mAh g^{-1} at a current density of 25 mA g^{-1} was achieved, correlating to an energy density of 74 Wh kg^{-1}. Moreover, the paper-like thin films' mechanical stability supported a cycling stability over 500 cycles.

The highly porous scaffolds are fabricated by unidirectional ice-templating and subsequent freeze drying from the aqueous V_2O_5 nanofiber dispersion. Such scaffolds exhibit a porosity of 99.9% and the longitudinal cross-section reveals an anisotropic structure along the employed temperature gradient. Contrary, the transverse cross-section shows regular stacked lamellas with interconnecting pillars. This sophisticated microstructure enables a good mechanical stability and thus creasing creates a corrugated lamella structure without any macroscopic visible damage. The creasing further generates additional contact points between the lamellas which facilitates the mass transport path. This results in an increasement of the electrical conductivity upon creasing. The creased scaffolds were investigated as cathode material for AIBs, delivering a specific storage capacity of up to 105 mAh g^{-1} at a current density of 500 mA g^{-1} with a corresponding energy density of 52 Wh kg^{-1}. Moreover, the creased scaffolds show a superior areal capacity and energy density compared to the paper-like thin films for the same current density.

All in all, two different structural designs employing V_2O_5 nanofibers were successfully established exhibiting good mechanical and electrical properties. It was successfully demonstrated that the microstructures can host and reversible intercalate mono- and multivalent ions, such as Li^+ and Al^{3+}, achieving a high electrochemical performance. In particular, the application in aluminum-ion batteries provided promising insights and results for novel design guidelines of nanostructured advanced electrodes for metal-ion batteries, as the shown V_2O_5 cathodes outperform reported V_2O_5- and carbon-based electrodes.

6 Zusammenfassung

Ziel dieser Arbeit war ein synergetischer Ansatz, der bioinspirierte Strukturdesigns mit elektrochemischen Fachkenntnissen zur Herstellung von nanostrukturierten, freistehenden und binderfreien Elektroden für mono- und multivalente Metall-Ionen Batterien kombiniert. Hierbei war die hierarchische Architektur der Elektroden dem Aufbau von Biomaterialien nachempfunden. Als Vorbilder dienten die dichte und gestapelte Mikrostruktur von Perlmutt sowie die hochporöse Sepiaschale. Hierfür wurden 1D flexible V_2O_5 Nanofasern als Baustein für die Elektroden verwendet, welche über ein Sol-Gel Verfahren hergestellt wurden. Dabei wurde die Nanofaserlänge über die Wachstumszeit kontrolliert, die die mechanischen Eigenschaften stark beeinflusste. Zudem besaßen die Nanofasern funktionelle Oberflächengruppen, die für die Herstellung der mechanisch stabilen, freistehenden und elektrisch leitfähigen Mikrostrukturen wichtig waren, so dass Perlmutt-inspirierte, 2D papierähnliche dünne Filme und 3D hochporöse Gerüste, die der Sepiaschalenstruktur nachgeahmt sind, synthetisiert werden konnten. Die erhaltenen Mikrostrukturen konnten erfolgreich als neue V_2O_5 Kathoden für Lithium- und Aluminium-Ionen Batterien eingesetzt werden.

Die 2D papierähnlichen dünnen Filme wurden über einen Selbst-assemblierungsprozess hergestellt, welcher zu Mikrometer dicken Filmen aus hierarchisch angeordneten Bündeln und Lamellen mit eingelagertem Wasser führte. Das Wasserstoffbrücken basierte Netzwerk besaß bemerkenswerte mechanische Eigenschaften, die mit länger werdenden Nanofasern verbessert wurden. Mit einer feuchtigkeitskontrollierten Nachbehandlung wurde das Wasserstoffbrücken Netzwerk weiter verstärkt, was zu einem weiteren Anstieg der mechanischen Eigenschaften führte. Zusätzlich wurde eine elektrische Leitfähigkeit von bis zu 2 S cm^{-1} erreicht, die sich aus einem elektronischen und ionischen Beitrag zusammensetzte. Der elektronische Beitrag konnte durch Altern der papierähnlichen dünnen Filme weiter erhöht werden. Dabei wurde V^{5+} zu V^{4+} teilweise reduziert, was sich in einem Anstieg der elektrischen Leitfähigkeit bemerkbar machte. Weiter konnte die reversible Einlagerung von Li^+ demonstriert werden. Hierbei wurde eine Speicherkapazität von 150 mAh g^{-1} bei einer Stromdichte von 100 mA g^{-1} erreicht.

Zudem wurden die papierähnlichen dünnen Filme als binderfreie und freistehende Kathoden für Aluminium-Ionen Batterien getestet. In diesem Zusammenhang wurde ein selbstlimitierender Kupfer Dotierungsprozess etabliert, welcher sich die Azidität der

ionischen Flüssigkeit, die als Elektrolyt verwendet wurde, zu Nutze machte. Folglich wurde eine Kupfer-dotierte V_2O_5 Bronze mit kupferreichen Ausscheidungen gebildet, was zu einem erheblichen Anstieg der elektrischen Leitfähigkeit um vier Größenordnungen führte. Dadurch wurde die elektrochemische Leistung solcher modifizierten Kathoden verbessert, was die reversible Einlagerung von Al^{3+} erleichterte. Somit wurde eine Speicherkapazität von 170 mAh g^{-1} bei einer Stromdichte von 25 mA g^{-1} erreicht, korrelierend zu einer Energiedichte von 74 Wh kg^{-1}. Darüber hinaus erlaubte die mechanische Stabilität der Filme eine verbesserte Zyklenstabilität über 500 Zyklen.

Die 3D hochporösen Gerüste wurden aus einer wässrigen V_2O_5 Nanofaser Dispersion mittels unidirektionalen Eisschablonenverfahren mit darauffolgender Gefriertrocknung hergestellt. Solche Gerüste besaßen eine Porosität von 99,9% und eine anisotrope Struktur entlang dem verwendeten Temperaturgradienten. Im Gegensatz hierzu, zeigte der Querschnitt regelmäßig angeordnete Lamellen mit verbindenden Säulen. Diese ausgeklügelte Mikrostruktur erlaubte eine hohe mechanische Stabilität, die das Falzen ohne makroskopisch sichtbaren Schaden ermöglichte, das zu einer welligen Lamellenstruktur führte. Das Falzen generierte zusätzliche Kontaktpunkte zwischen den Lamellen, welche den Ladungstransport erleichterte und somit die elektrische Leitfähigkeit verbesserte. Die gefalzten Gerüste wurden als neuartiges Kathodenmaterial in Aluminium-Ionen Batterien eingesetzt und erreichten eine Speicherkapazität von bis zu 105 mAh g^{-1} bei einer Stromdichte von 500 mA g^{-1} mit einer entsprechenden Energiedichte von 52 Wh kg^{-1}. Zudem zeigten die gefalzten Gerüste eine höhere Flächenkapazität und Energiedichte als die papierähnlichen dünnen Filme bei gleicher Stromdichte.

Die beiden bioinspirierten Strukturdesigns mit V_2O_5 Nanofasern als Bausteine besaßen gute mechanische und elektrische Eigenschaften. Durch ihre einzigartigen Mikrostrukturen konnten mono- und multivalente Ionen, wie Li^+ und Al^{3+}, reversibel eingelagert werden, und eine erhöhte elektrochemische Leistung wurde erreicht. Außerdem übertrafen die entwickelten V_2O_5 Kathoden bereits bekannte V_2O_5 und Kohlenstoff basierte Elektroden. Daher liefert diese Arbeit aufschlussreiche Einblicke in neuen Designstrategien mit vielversprechenden Ergebnissen für innovative nanostrukturierte hochentwickelte Elektroden für Batterien mit einer hohen Energiedichte.

7 Danksagung

An dieser Stelle möchte ich mich nun bedanken für die zahlriechen Personen auf deren Unterstützung ich bauen konnte.

Zuerst möchte ich mich bei meinem Doktorvater Herrn Prof. Dr. Joachim Bill bedanken, für die Möglichkeit unter seiner Leitung diese Arbeit zu realisieren und dafür, dass er mich in meinem Vorhaben unterstützt hat und für seine stetige Unterstützung. Weiter möchte ich Herrn Prof. Dr. Siegfried Schmauder und Herrn Prof. Dr. Thomas Schleid für die Übernahme des Mitberichts beziehungsweise des Prüfungsvorsitzes danken.

Mein größter Dank gilt Dr. Zaklina Burghard, die mich bereits während meiner Masterarbeit und nun auch während meiner Dissertation betreut hat. Ich danke Ihr für ihre stetige Unterstützung, die zahlreichen Forschungsprojekte, die ich mit ihr bearbeiten konnte, sowie die Möglichkeit internationale Konferenzen zu besuchen. Über die Jahre führten wir unzählige fachliche Diskussionen und fanden oft einen gemeinsamen Nenner und ich konnte viel von ihr lernen.

Ein weiter Dank gilt allen Kollegen des Instituts für Materialwissenschaft, sowie der beiden Max-Planck-Institute, die mich stets tatkräftig unterstützt haben und wissenschaftliche Diskussion anregten. Sie ermöglichten mir Zugang zu Messgeräten, die diese Arbeit erst ermöglicht haben. In diesem Zusammenhang gilt mein Dank Dr. Marc Widenmeyer für die Hilfe bei XRD-Messungen, Juliane Kränzl für alle administrativen Aufgaben und den beiden Abteilungen von Prof. Dr. Joachim Spatz und am Max-Planck-Institut für medizinische Forschung und Prof. Dr. Jürgen Weis am Max-Planck-Institut für Festkörperforschung.

Besonders möchte ich mich jedoch bei Dr. Stefan Kilper, Dr. Andrea Knöller, Timotheus Jahnke, Maximilian Hackner und Leila Raafat für die jahrelange Unterstützung und für hervorragendes Teamwork bedanken. Gemeinsam haben wir jede Herausforderung gemeistert und hatten zu weil schöne Zeiten auf gemeinsamen Konferenzen. Dabei sind sie zu echten Freunden geworden und wir hatten auch außerhalb des Instituts viel Spaß.

Zu guter Letzt möchte ich meiner Familie und Freunden danken, deren seelischen und moralischen Rückhalt ich hatte und mich an dem ein oder andern Abend auf anderen Gedanken brachten und so für den nötigen Ausgleich sorgten.